UNIVERSITY OF SOUTHAMPTON

Equatorial Pacific Dynamics: Lateral Mixing and Tropical Instability Waves

Luciano Ponzi Pezzi

Submitted for the degree of Doctor of Philosophy

School of Ocean and Earth Sciences

August 2003

The Graduate School of the

School of Ocean and Earth Science

Equatorial Pacific Dynamics: Lateral Mixing and Tropical Instability Waves

This PhD dissertation by

Luciano Ponzi Pezzi

has been produced under the supervision of the following persons

Supervisors

Prof. Kelvin Richards

Mr. Peter Challenor

Chair of Advisory Panel

Prof. Jochem Marotzke

Member of Advisory Panel

Dr. Neil Wells

UNIVERSITY OF SOUTHAMPTON

ABSTRACT

FACULTY OF SCIENCE
OCEAN AND EARTH SCIENCES

Doctor of Philosophy

Equatorial Pacific Dynamics:
Lateral Mixing and Tropical Instability Waves

by

Luciano Ponzi Pezzi

This thesis presents a study focused on two main aspects of the equatorial Pacific dynamics: One is the parameterization of lateral mixing and its impact in numerical simulations of the equatorial Pacific ocean. The other is the Tropical Instability Wave (TIW) characteristics in eastern equatorial Pacific region and the associated coupled ocean-atmosphere interactions. The main objectives of this research project are achieved using both model and satellite observations.

An ocean general circulation model (OGCM) is adapted to represent the tropical Pacific ocean. Experiments are performed to assess the impact of the form of lateral mixing of momentum and tracers on the state of an equatorial ocean. It is found that the large-scale structure of both the velocity and temperature fields are very sensitive to the imposed parameterization of lateral mixing in the model. With uniform values for the viscosity and diffusion coefficient across the domain, a decrease in these coefficients increases the activity of TIW, resulting in an increase in the Sea Surface Temperature of the cold tongue, and thus overcoming the cold bias often found in ocean models of the equatorial Pacific. However there is an associated increase in the strength of the Equatorial Under Current (EUC) to unrealistic levels. It is found that the strength of the EUC can be limited, whilst having little affect on the TIW activity, by applying an enhanced level of mixing in the vicinity of the equator. This enhanced mixing is used to model the effect of the observed interleaving of water masses across the equator.

Descriptions of TIW variability characteristics in the tropical Pacific ocean as function of the large scale climate conditions and interannual variability, such as ENSO, are made based on satellite data. As others have found, the TIW ocean-atmosphere coupling is caused by atmospheric boundary layer (ABL) instability and mixing. Our observational results suggest that this mechanism of wind-SST coupled variability may occur not only during La Niña years, when TIWs are more active, but whenever the TIWs are active. There is evidence that the TIW activity increases when under strengthened wind stress conditions either in La Niña years or, *by analogy*, when numerical simulations are carried out with stronger wind stress.

The coupled ocean-atmosphere experiments, using a simplified ABL scheme, under different coupling strengths, suggests that this system is able to accurately simulate the TIW atmospheric imprints using a standard coupling coefficient. The active coupling strengthening produces a negative feedback on the TIWs. The TIW activity tend to be reduced in both surface and sub-surface ocean. The experiments using active wind interaction simulate a cooler Cold Tongue region with anomalous values reaching -0.3°C in some equatorial regions, when compared with the control (CTL) experiment. However, the mechanisms which fully explains the ABL effects in the TIWs characteristics need to be further investigated.

DECLARATION

I hereby declare that the work presented within this thesis is my own and was undertaken wholly whilst registered as a full-time postgraduate at the University of Southampton.

Luciano Ponzi Pezzi
August 2003.

Acknowledgements

Principally, thanks goes to Prof. Kelvin Richards for his scientific advice throughout this project and for the scientific and professional opportunities he has helped me to find during this project.

I am very appreciative to Brazilian government, through the Conselho Nacional de Pesquisas Científicas (CNPq), for sponsoring my project and for its continuing investment in education as an integral part of the country development.

I would like to thank Dr. Jérôme Vialard, Dr. Christophe Menkes, Dr. David Anderson and Prof. Kelvin Richards for encourage me to study Tropical Instability Waves under an ocean-atmosphere coupled perspective; Mr. Peter Challenor for accept the challenge in supervising me throughout my final year and Dr. Paolo Cipollini for his invaluable assistance with use of spectral analysis techniques.

I am grateful to Centro de Previsão do Tempo e Estudos Climáticos (CPTEC/INPE) for giving me the opportunity to participate in a Ph.D. program at SOES/SOC and the encouragement by Dr. Carlos Nobre, Dr. José Paulo Bonatti and Dr. Iracema Cavalcanti. LODYC and IPRC for giving me the opportunity to improve my research and also grow as a professional during the scientific visits. Many people have encouraged and supported me during this project. I would like to thank all my friends and colleagues at SOES/SOC and CPTEC/INPE, unfortunately is impossible mention all of them.

I would like to express my gratitude to my family, Marta, João, João Pedro, Luis Gustavo, Thais, Alberto, Albertinho e Gabriela for all their love, support and positive thoughts which many times shortened the distances between England and Brazil. My parents Terezinha and Cid, *in memory*, who *always* believed in me. Uncles, Deca and Carluccio, who always found a way to reach me. All my friends and relatives in southern Brazil who never let me feel alone. A great part of this work or *eventual success* achieved is due to all your support.

Finally, my love and thanks to my beloved Marisa who has shared the highs and lows during the years we have been together. Words cannot express how deeply appreciative I am for her dedication, support and encouragement throughout my project. Also, for the decision in suspend her own carrier in Brazil and accept the new life and professional challenges in England.

Contents

List of Figures

List of Tables

Chapter 1

Introduction

1.1 Motivation

One of the most studied and reasonably well understood climatic phenomena in the tropical Pacific oceanic region is the so called El Niño Southern Oscillation (ENSO). This is a natural and quasi-periodic coupled ocean-atmosphere phenomenon responsible for patterns of the global circulation which are related to anomalous climatic phenomena in many continental regions around the globe (Philander, 1992). The oceanic part of this phenomenon is caused by changes in the surface winds over the tropical Pacific ocean. Under normal conditions, El Niño starts as a relaxation of these strong climatological equatorial easterly winds that produce a strong upwelling of cold water in the eastern Pacific that moves westward.

As a consequence of this wind relaxation, warm surface waters that have been piled up in the western Pacific move eastward. Conversely, La Niña is established by oceanic and atmospheric conditions generally opposite to those of El Niño, i.e. when ocean waters, cooler than average, spread in the central and eastern Pacific ocean formed by stronger uppwelling, caused by the easterly winds strengthening.

Since the strong 1982-83 El Niño the scientific community gave greater emphasis on the importance of the ENSO to the world climate and a big effort was undertaken to improve the observational system in the tropical Pacific ocean (McPhaden *et al.*, 1998). By the middle of the 1980's the Tropical Ocean-Global Atmosphere (TOGA) program was set up. This resulted in the development of an observing system to support seasonal to interannual

climate studies focussed on understanding the detailed physics of both Warm Pool and Cold Tongue of the equatorial Pacific. In support of TOGA the Tropical Atmosphere Ocean (TAO)[1] array was implemented to collect in situ oceanographic and meteorological data (e.g., wind, SST and current velocities) and telemetering to shore in real-time via the Argos satellite system.

The so called 'El Niño of the century' occurred in 1997-98 and it is illustrated in Figure 1.1. This episode has developed quite rapidly, from May to the end of 1997, as compared to previous intense events including the 1982-83 case. In the eastern Pacific region, near the Ecuadorian and Peruvian coast, waters were warmer than normal reaching 4°C above climatological conditions in December of 1997 (as high as 29°C). As part of the ENSO cycle evolution, the trade winds rapidly returned to normal conditions in the eastern Pacific around May 1998, allowing for upwelling of subsurface cold waters to appear, marking the end of the event in June 1998 and giving rise to La Niña of 1998-99. At this time, the scientific community was able to forecast and produce warnings some time in advance about the intensity and climate impacts produced, as well as monitoring in real time the event with TOGA/TAO data. This was the case in South America, where the Centre for Weather Forecast and Climate Studies (CPTEC/INPE) [2] supplied the Brazilian government and decision makers with information about the ENSO development and associated climate impacts. The CPTEC mission is provide state of art numerical weather and climate forecasts for the Brazilian government and society as a whole.

The tropical Pacific basin plays a significant role in the global climate. For instance see, Ropelewski and Halpert (1987, 1989) for a good indication of the ENSO impacts in the precipitation and temperature over many regions in the world. A relatively small change in the SST can produce weather and climate anomalies over several regions of the globe. Nowadays it is possible to forecast with some accuracy and quite well in advance both ENSO and its impacts in the temperature and precipitation anomalies in some regions, e.g. over North America (Ropelewski and Halpert, 1986, Barnston and Preisendorfer, 1987), Hawaii

[1]The TAO array was renamed to TAO/TRITON array on 1 January 2000 since the Japan Marine Science and Technology Center (JAMSTEC) introduced a new ocean buoy measurement system called TRITON (Triangle Trans-Ocean Buoy Network) to replace ATLAS buoys in the western Pacific. TOGA-TAO data are available at http://www.pmel.noaa.gov/tao/jsdisplay

[2]INPE stands for National Institute for Space Research and CPTEC is part of this institute. Information about CPTEC and forecasts for South America can be downloaded from http://www.cptec.inpe.br

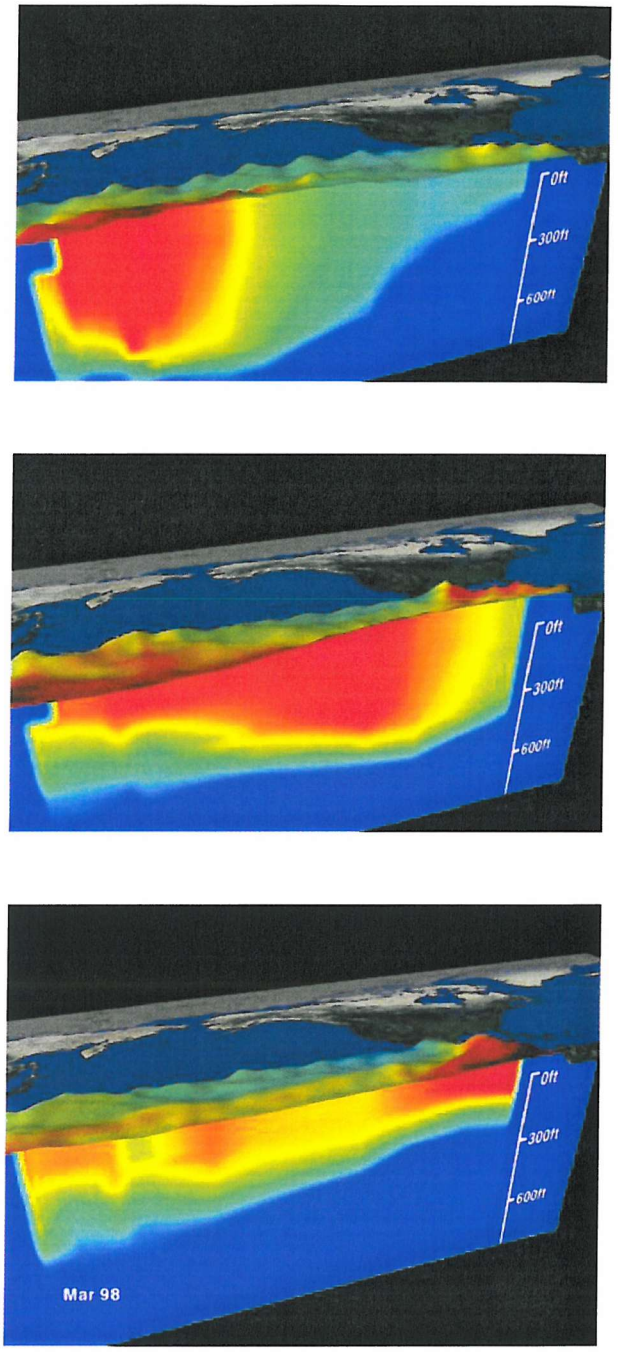

Figure 1.1: SST and water temperature profile in the equatorial Pacific ocean. January 1997 Normal Conditions, (top panel), November 1997, El Niño mature phase (middle panel) and March 1998 El Niño's transition to La Niña (lower panel). The images show sea surface topography from TOPEX satellite, SST from NOAA AVHRR satellite sensor and sea temperature below the surface as measured by TAO moored buoys, illustrating how the thermocline is flattened out by La Niña . Red is 30°C, blue is 8°C. The thermocline is the border between the dark blue at the bottom and the cyan. Source: http://nsipp.gsfc.nasa.gov/enso.

and Alaska (Barnston and He, 1996), South America (Rao and Hada, 1990, Pezzi and Cavalcanti, 2001), Amazon region of South America (Souza *et al.*, 2000) and south of Brazil (Pezzi *et al.*, 2001). Some ENSO impacts in the tropical and southern Africa, Australia and parts of India are reported also in Ropelewski and Halpert (1987) and Ropelewski and Halpert (1989).

Focusing specifically on South America climate impacts, a warm (cold) ENSO phase can produce a drastic reduction (increase) in the amount of precipitation over the northeast of South America (Nordeste) and eastern part of Amazon region during their rainy season Ropelewski and Halpert (1987), Rao and Hada (1990), Souza *et al.* (2000). On the other hand, the southeast of South America can experience an accentuated increase (reduction) in the amount of precipitation.

Extreme climate fluctuations are observed to impact severely on natural resources, human life and the economies of several countries in the world. This is mainly true in the tropics since the range of weather extremes is not as large as in the extra-tropics where the weather systems produce large variations in the pressure and temperature. However, in the tropics a shift in the precipitation can be devastating. Because of these impacts on the world climate caused by the tropical oceans and the possibility of seasonally forecasting the oceanic state in advance, there is a strong motivation and need to continue studying and understanding these subjects that are related to ocean, atmosphere with interactions both at large scales (global impacts) and at regional scales.

The accuracy of numerical simulations depends of the ability of atmospheric and ocean models in capturing the essential physics of the phenomena. Models used for climate studies and seasonal forecast purposes lack in representing all physical processes affecting the ocean-atmosphere interactions. For instance, coupled and forced models tend to exhibit a cold bias in the Cold Tongue region. This is a common problem found in Ocean Global Circulation Model (OGCM) in which the Cold Tongue is too cold and extending to far west. This might be partially caused by the misrepresentation of Tropical Instability Waves (TIWs) activity, which are known to transport significant amount of heat flux to the Equator (Hansen and Paul, 1984). The typical level of lateral mixing used in the models might be large enough to damp these wave activities.

The model deficiency in reproducing the major features in the tropical climatology might be attributed to a sub-grid scale processes misrepresentation as reported in Neelin (1992). Previous studies such as Maes *et al.* (1997) and Large *et al.* (2001) have suggested that small scale processes such as lateral mixing plays an important role in SST and large scale equatorial dynamics simulation. In addition, the mechanisms that control SST and the dynamics in the eastern Pacific cold tongue region remain still unclear and need to be further understood.

This thesis will focus on two main aspects of the equatorial Pacific dynamics: One is the parameterization of lateral mixing and its impact in the numerical simulations of the equatorial Pacific ocean. The other is the Tropical Instability Wave (TIW) characteristics in the eastern equatorial Pacific region and the associated coupled ocean-atmosphere interactions.

In the reminder of this chapter we introduce the study area, briefly review lateral mixing, the main characteristics of TIWs and the associated coupled ocean-atmosphere interactions. This chapter finishes outlining the aims of this project. More comprehensive reviews are provided in the introductory sections of each chapter.

1.2 Study area

The eastern tropical Pacific region is characterized, normally, by a tongue of cold water as shown in Figure 1.2, where temperature can vary over 10°C during its annual cycle. This pattern is maintained by the Walker Cell circulation, that consists of a large scale zonal and vertical atmospheric circulation with an ascending branch over the western Pacific and a descending branch over the eastern Pacific, coinciding with the cool tongue region. The appearance of cool water (as shown in 1.2) extends from the west coast of South America westward along the equator. During March the water is warm in the eastern Pacific and the SST is nearly symmetric about the equator, with cooler water at the equator as a result of equatorial upwelling. After April this upwelling becomes stronger and subsequently this cool water spreads over the southern hemisphere as a result of mixing processes. Using a coupled GCM, Xie (1996) has suggest that the equatorial Pacific ocean has an annual mean climate asymmetry over eastern region caused by the American continental asymmetries.

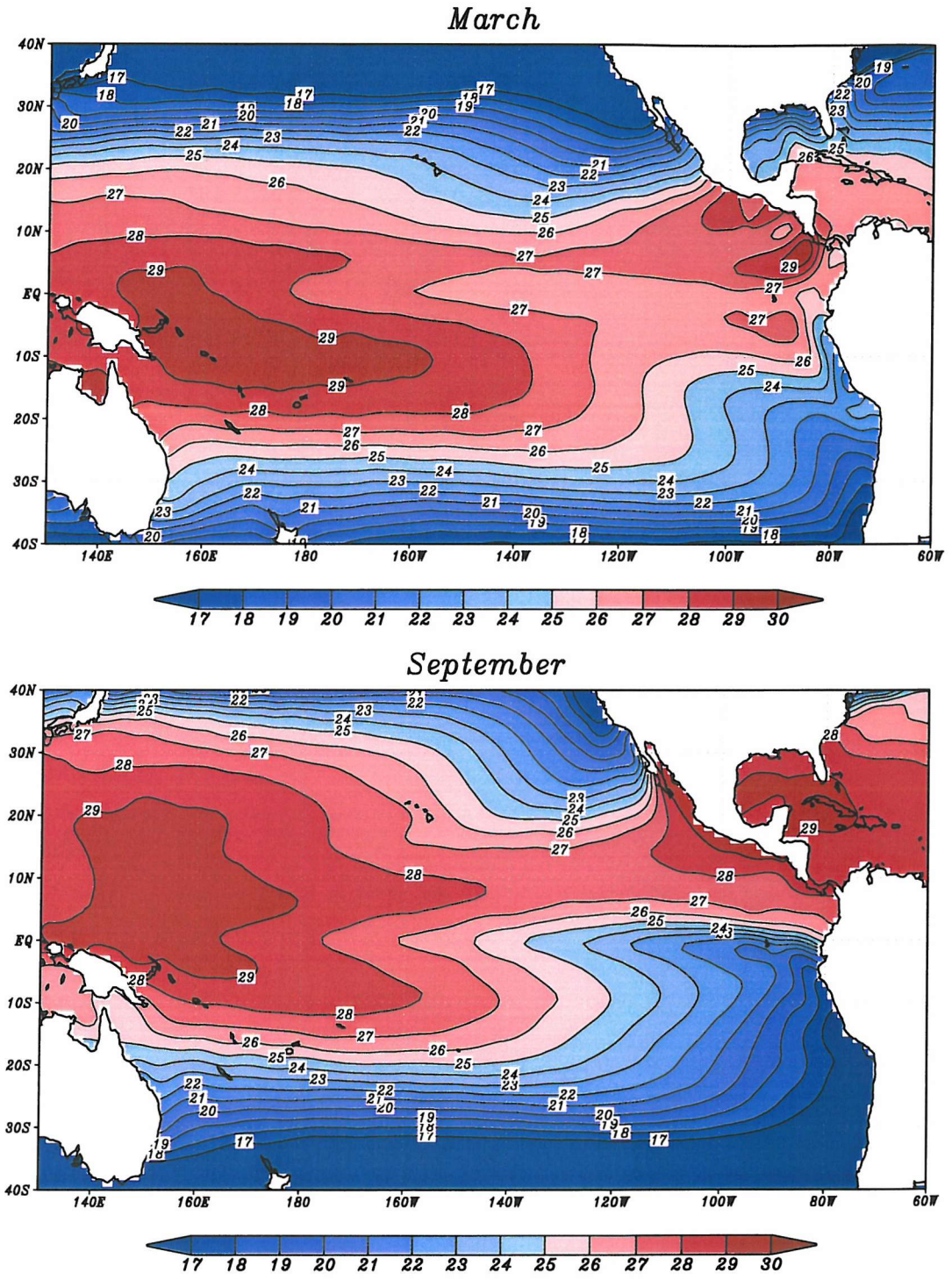

Figure 1.2: Climatological SST for the tropical Pacific, March (upper panel) and September (lower panel). SST data source: Reynolds and Smith (1994).

The SST annual cycle in this region is not very well represented in coupled model simulations because of the poor representation of the Cold Tongue/ITCZ complex system. The mechanisms governing the temperature and salinity field evolution in the oceanic cold tongue still need better understanding. These include mixing processes as well as oceanic interactions with the atmospheric boundary layer structure. This oceanic region clearly has an influence over the climate in the continents surrounding it as well as remote impacts on the tropical Atlantic, South America (Moura and Shukla, 1981, Nobre and Shukla, 1996, Pezzi and Cavalcanti, 2001) and northwest Africa (Folland *et al.*, 1986).

Many efforts have been done by the scientific community to better understand the climate in this region and its teleconnections with the global climate. For instance, the importance of the east Pacific has increasingly being recognized. A specific project for this area, the Eastern Pacific Investigation of Climate Processes (EPIC)[3], was scheduled for the years 1998-2004 to investigate the climate and the coupled ocean-atmosphere system by modelling and observational studies. It is believed that the extensive marine stratus deck off the west coast of South America act to reflect a large fraction of the incident solar radiation, which would otherwise be absorbed by the ocean consequently cooling the ocean. This reinforces the cross-equatorial contrast in SST and intensifies the cross-equatorial Hadley cell circulation (Philander *et al.*, 1996, Ma *et al.*, 1996). A better understanding of the eastern Pacific ocean-atmosphere coupling and the Cold Tongue temperature regulating mechanisms such as TIWs would benefit the numerical parameterizations improvement, basing their developments on the physics evolved in these processes.

1.3 Background

1.3.1 Lateral mixing

Small scale physical processes and eddy activities have to be parameterized in numerical models since they are not explicitly resolved due to the limitations in grid resolution. Ac-

[3]EPIC is a process study sponsored by NSF and NOAA under the US CLIVAR, more information can be obtained from http://www.atmos.washington.edu/gcg/EPIC/

cording to Garrett (2003) and Richards and Edwards (2003), the sub-grid scale processes such as lateral mixing needs to be observed and understood so their effects can be represented based on physical reasoning.

Nevertheless, due to our lack of understanding, the eddy effects are included in most of the numerical models in a diffusive manner by setting values for diffusion coefficients, such as

$$\overline{u_i'\kappa'} = -A_h \frac{\partial \overline{\kappa}}{\partial y_i},$$

where κ is the property being mixed, A_h is the diffusion coefficient, u is the velocity field and y_i is the direction. The magnitude of the lateral mixing coefficient (A_h) is, somewhat, related to the horizontal grid resolution used in the simulation since it is used for numerical stability reasons. The diffusion value is much larger than molecular viscosity and Richards (1998) has suggested that an effective diffusion value is on the order of 1.0×10^3 m^2s^{-1}, large enough to affect the dynamics of the system.

Some attempts have been made to base lateral mixing parameterizations on physics reasoning. For instance, Banks (1997), Richards and Banks (2002) and Richards and Edwards (2003) have suggested that the interleaving of water masses in producing meridional fluxes of tracers and momentum also plays a role in the lateral mixing and in some way this phenomenon might be considered in the parameterizations. Interleaving is a process which produces alternate layers in the vertical of two water masses, with the layering brought about by differential lateral advection. Up to now, the mechanism responsible for the interleaving formation is still not clear. Richards and Edwards (2003) suggests that inertial instability is the prime mechanism for the formation of the interleaving, i.e. caused by the shear instability. The secondary candidate is that the interleaving of water masses is formed by double-diffusive fluxes. However, observations alone can not be used to distinguish between the two mechanisms so that theoretical studies should be done in parallel to observations in order to understand both processes.

Some previous studies have demonstrated that lateral mixing parameterizations can play a crucial role in the numerical results. Banks (1997) studied the effects of lateral mixing and intrusive features with a simplified 2-D model. Maes *et al.* (1997) demonstrated the

importance of the lateral mixing using the OPA OGCM (Madec *et al.*, 1998) in the Tropical Pacific basin. In that study, the sensitivity of the model simulation to the magnitude of the momentum and diffusivity coefficients is assessed by varying the coefficients by three orders of magnitude. The lateral mixing coefficients used are 1×10^4 m^2s^{-1}, 1×10^3 m^2s^{-1} and 1×10^2 m^2s^{-1}. Both Banks (1997) and Maes *et al.* (1997) have suggested that the strength of the Equatorial Under Current (EUC) increased when the eddy dissipation was decreased with an associated change in the vertical mixing. Maes *et al.* (1997) has shown that in some regions where they used small horizontal coefficients the vertical mixing was increased as well as the vertical shear. As a consequence changes in the vertical structure of the equatorial current systems were produced. They postulated that lateral mixing plays an important role in the model solution since a change in the lateral mixing (one parameter) characteristics will affect the model's behavior (multi-parameter) changing the role of others parameters, e.g. in the EUC regime and in the vertical mixing.

Even with the improvements made in the knowledge of lateral mixing effects in equatorial simulations, a number of problems still remain. Increasing the horizontal resolution (from 1/2° to 1/4°) and decreasing the lateral mixing is not the solution to a better representation of equatorial dynamics since the model tends to simulate an excessive strong undercurrent as it is shown in Chapter 2 and Pezzi and Richards (2003).

Some recent studies have investigated the orientation of the mixing tensor such as horizontal mixing versus isopycnal mixing. Lengaigne *et al.* (2003) have tested both orientations in a OGCM, Guilyardi *et al.* (2001) in a coupled GCM (CGCM) and Megann and New (2001) in an primitive equation isopycnal coordinate model. All studies have suggested that isopycnal mixing of the tracers (temperature and salinity) tend to improve the tropical thermocline representation while mixing momentum along isopycnic surfaces improves the equatorial current structures (Lengaigne *et al.*, 2003). This topic is further explored in Chapter 2.

1.3.2 Tropical Instability Waves

Oceanic characteristics

Legeckis waves, nowadays called Tropical Instability Waves are oceanic long waves.

They were first observed in the Atlantic by Duing *et al.* (1975) and using environmental geostationary infrared satellites over the Equatorial Pacific by Legeckis (1977). They are generated over the eastern equatorial Pacific Ocean (Figure 3.1) and propagate westward up to the mid Pacific basin with a zonal wavelength ranging from 700 to 2000 Km, period from 20 to 40 days and phase speed from 20 to 80 cm s^{-1} westward approximately (Qiao and Weisberg, 1995).

In recent years a number of research programs have highlighted the importance of studying TIWs by numerical models and observations. A project named Tropical Instability Waves Experiment (TIWE) was initiated in the boreal spring 1990 aiming to understand the effects of these waves in the near-surface mass, momentum, heat and energy instabilities. During this project observed data have been collected from arrays of moored instrumentation, shipboard hydrographic mapping and lagrangian drifter tracking as described in Qiao and Weisberg (1995) and Qiao and Weisberg (1998). Also, TIWs have been studied in the EPIC and the TOGA project (McPhaden *et al.*, 1998).

The generation and propagation of the observed TIWs are associated with the SST front produced by the low temperatures of the South Equatorial Current (SEC) and upwelled waters within eastern equatorial region. These cooler waters contrast with those relatively warm waters from the Pacific west advected by the North Equatorial Countercurrent (NECC). This region has a marked latitudinal SST gradient and during La Niña years the temperature and hence density difference between the cold tongue and the surrounding waters is greater.

These waves grow north of Equator exhibiting their maxima variability around 2°N where the meridional SST gradient is highest and propagate westward from the vicinity of the Galápagos Islands reaching a maximum around 120°W and then decay. Latitudinally, the wave activity is decreased on the Equator and increased again further south, around 2°S. TIWs are important mechanisms in the equatorial Cold Tongue momentum and heat balance and salt transport (Hansen and Paul, 1984, Bryden and Brady, 1989, Swenson and Hansen, 1999, Vialard *et al.*, 2003a). They are also important for the biological life associated with this frontal region (Flament *et al.*, 1996, Strutton *et al.*, 2001, Menkes *et al.*, 2002) where a high concentration of marine life occurs.

The TIWs energetic and generation mechanisms are not fully understood and there is much debate still going on. Using an OGCM resembling the tropical Pacific ocean Masina and Philander (1999) and Masina *et al.* (1999) have suggested that waves are generated by two distinct instability processes that occur in different latitudes. North of the equator the waves have baroclinic instabilities as the energy source while barotropic instability prevails at the equator. Their results suggest that the meridional shear between the northern branch of the SEC and EUC is barotropically unstable and stronger than those between the SEC and NECC. These results are in agreement with those found by Yu *et al.* (1995). Using a linearized 2 $\frac{1}{2}$ layer ocean model they have shown results suggesting that the meridional asymmetries of TIWs are due to asymmetries in the two branches of the South Equatorial Current (SEC) and of the equatorial SST front, and not due to the presence of the NECC.

Baturin and Niiler (1997) have investigated the energetics of the currents associated with the TIW activity using satellite data collected by the Advanced Very High Resolution Radiometer (AVHRR) sensor, drifting buoys and current meter mooring (TOGA-TAO) at 110°W and 140°W. They have analyzed periods of strong and weak instabilities activities. In the location of 140°W the main activity is in October when both SEC and NECC become stronger and the eddy kinetic and potential energy generation are larger. At 110°W the energy production is present during all periods, without significant differences between periods of high and low TIW activity. They have also suggested that TIWs might interact with the atmosphere, with the wind gaining energy from the instability waves.

Flament *et al.* (1996) and Kennan and Flament (2000) have investigated a tropical vortex using data collected from the TIWE. They analyzed a tropical vortex confined in the upper thermocline, between 2° to 6°N and 142° to 136°W, using superimposed data collected by an array of conductivity-temperature-depth (CTD), acoustic doppler current profiler (ADCP) and satellite-tracked buoy. Away from the equator this vortex drifted along the shear layer between SEC and NECC advecting cold, saline, equatorial water northward and warmer, fresher tropical water southward.

The influence of the Galápagos Island on TIWs was studied by Brentnall (1999) using a set of numerical results. He has shown that TIWs are more active when the Galápagos are present in the experiments, compared with experiments when the islands are absent. The main reason for this is the intensification of a pair of barotropically unstable zonal jets in

the northern and southern flanks of the islands.

Ocean-atmosphere interactions

TIWs are oceanic phenomena originating from the equatorial current system shear and water masses differences. They are not caused by the surface wind action. However, there is a signal of TIW activity in the lower atmosphere, within the Atmospheric Boundary Layer (ABL). Recently, Liu *et al.* (2000) have shown, reinforcing Hayes *et al.* (1989) and Wallace *et al.* (1989) previous findings, that over warm water the air mixing is increased because the buoyancy of the air is increased thus reducing the wind shear in the boundary layer and producing stronger winds at the surface. The TIW atmospheric imprints induced by the SST changes penetrates the whole depth of the ABL as shown by Hashizume *et al.* (2002) using atmospheric soundings. The surface wind response to the SST gradients can be seen in Figure 1.3a.

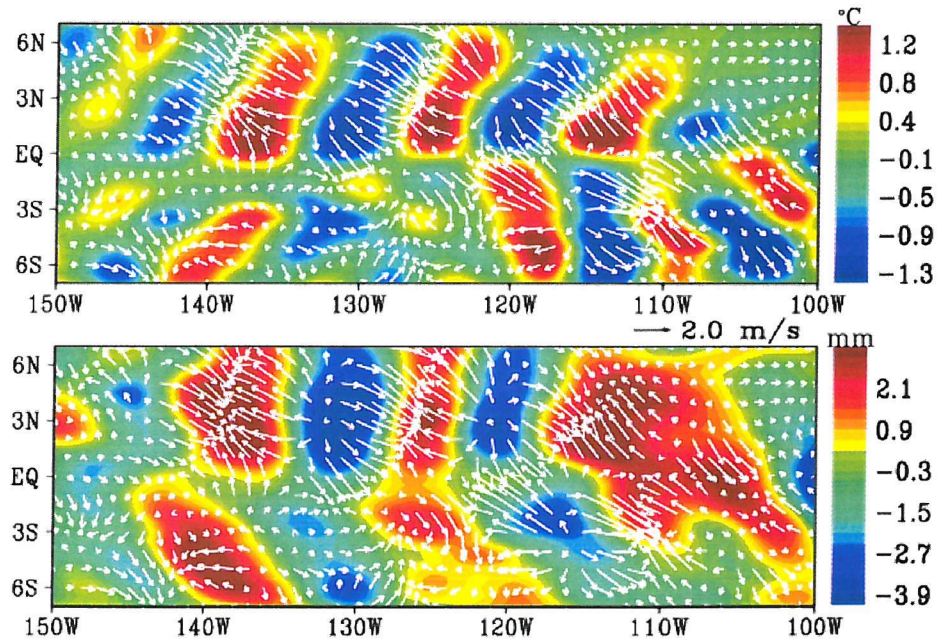

Figure 1.3: Vector wind anomalies (white arrows) are superimposed on the color images of SST anomalies (a), and water vapor anomalies (b), for 11 September 1999, based on filtered data (After Liu *et al.* (2000)).

As the wind moves over these SST anomalies it is accelerated over warm SST anomalies and decelerated over cold anomalies producing centers of convergence and divergence at maximum SST gradient regions. The convergence maximum (minimum) also coincide with

the water vapor maximum (minimum), where convergence (divergence) feeds (withdraws) the water vapor up in the atmosphere increasing (decreasing) the instability in this air column, shown in Figure 1.3b. Based on their findings Liu *et al.* (2000) suggest that the modification of the surface winds are due to the ABL stability changes, re-enforcing Wallace *et al.* (1989) and Hayes *et al.* (1989). A more comprehensive review about this topic is given in Chapters 3 and 4.

1.4 Aims

A number of important issues concerning the equatorial Pacific dynamics relating to lateral mixing and TIWs have been identified and need further study. The main issues are summarized in the following paragraphs.

The models are not perfect in simulating all oceanic phenomena because they have physical and numerical limitations. The small scale processes, such as lateral mixing, have impacts on the large scale dynamics of the equatorial ocean. Lateral mixing of momentum and tracers are not explicitly solved and parameterizations need to be improved considering also the physics evolved in the process. This point is considered further in Chapter 2, where different lateral mixing parameterizations are tested.

TIWs exhibit a clear interannual variability, being more active during La Niña years. Their dependence on other large scale climatic phenomena, such as ENSO, require further study and understanding. Some of the TIWs characteristics as function of the large scale climate characteristics are investigated here. The majority of TIWs observational studies have focused on one single TIW season. Attempts to extend previous studies by analyzing the TIWs seasonality are made in Chapter 3 using high resolution satellite data and numerical modelling experiments in Chapter 2.

Recently the TIW effect in the atmosphere, via mainly ABL stability modulations, has been well studied by means of high resolution satellite data and numerical models. However, there is still a need to understand the TIWs interactions with the ABL vertical structure as well as to explore whether these atmospheric TIW-induced signals can retroact onto the TIW oceanic characteristics. Attempts are made in Chapter 4 to investigate, under an

ocean-atmosphere coupled perspective, the ABL effects in TIWs characteristics.

The main objectives to be addressed in this project are as follows:

- To study the sensitivity of both the mean state and TIW activity of the equatorial Pacific to the strength and form of the lateral mixing parameterization.
- To determine annual and interannual TIWs characteristics and their dependence of the other large scale climatic phenomena such as ENSO, using satellite data.
- To study the coupled oceanic interactions with the Atmospheric Boundary Layer and determine the possible feedbacks in the TIWs characteristics.

The main objectives of this research project are achieved using a variety of different methods, as reflected in the structure of the rest of the thesis. In Chapter 2, the role of the form and strength of lateral mixing in numerical simulations of the oceanic mean state, energetics and TIWs generation is investigated. In Chapter 3, the TIWs interannual variability under the large scale climate perspective, such as ENSO phenomena, using high resolution satellite observations is examined. In Chapter 4, the TIW ocean-atmosphere coupling and associated feedbacks are examined. This thesis finishes by the Chapter 5 where a succinct reminder of what has been achieved is presented followed by suggestions of some future directions.

Chapter 2

Lateral mixing and equatorial dynamics

2.1 Introduction

Ocean models are used in a range of studies of the equatorial Pacific; from studies of the basic dynamics, thermodynamics and circulation of the ocean to seasonal prediction of ENSO events. The models used vary from very simple and idealized models up to those using complex formulations such as Ocean General Circulation Model (OGCM). However, OGCMs have numerical and physical limitations in simulating all ocean processes. The lack of ability of coupled models to reproduce major features of the tropical climatology may be attributed to a sensitivity to sub-grid scale processes as suggested by Neelin (1992). Because of limitations of spatial resolution, physical processes that are not explicitly resolved have to be parameterized, usually by assuming that small scale processes act in a diffusive manner. The magnitude of the associated diffusion coefficients for a given horizontal grid resolution is often chosen, somewhat arbitrarily, solely for reasons of numerical stability (Delecluse, 1994). Previous studies, however, have demonstrated that mixing processes can play a crucial role in the dynamics and thermodynamics of numerical simulations. Ideally a parameterization scheme should be based on sound physical reasoning. This is often not the case because of our lack of understanding of the physical processes involved on mixing different water masses, such as interleaving and internal waves. However, something we can do is to investigate the sensitivity of the system to the form of the imposed parameterization scheme, in order to ascertain the robustness of conclusions drawn from modelling studies.

Lateral mixing plays a important role in determining the sea surface temperature (SST) in the equatorial Pacific as showed by Stockdale *et al.* (1993) in a model inter-comparison. Maes *et al.* (1997) demonstrated the importance of horizontal mixing using the OPA OGCM (Madec *et al.*, 1998) in the tropical Pacific basin by assessing the model sensitivity to a variation of two orders of magnitude in the eddy viscosity and diffusivity coefficients. They state that there is a non-linear interplay between horizontal and vertical mixing of the model solution since a change in the lateral mixing (one parameter) characteristics affects the behavior of the model (multi-parameter) by changing the role of others parameters, e.g. in the Equatorial Under Current (EUC) regime and in vertical mixing. When the eddy dissipation is decreased both the strength of the EUC and the SST in the cold tongue are increased. The sensitivity of the system to the orientation of mixing was investigated in Lengaigne *et al.* (2003). They found that the upper part of EUC is deepened and the strength of the South Equatorial Current (SEC) increased for the equatorial Pacific and Atlantic oceans. However, when mixing of both tracers and momentum along isopycnic surfaces is allowed, they find that the strength of EUC and SEC are simulated more realistically when compared with observations. They argue that the extra equatorial circulation is improved when tracer is mixed along isopycnic surfaces compared with when both tracers and momentum are mixed along horizontal surfaces. Based on their findings Lengaigne *et al.* (2003) suggested that for a better representation of tropical circulation in climate models, isopycnic mixing for tracers and momentum must be considered (see also Megann and New (2001) who use an isopycnic coordinate model).

Some of the above studies have assumed that the viscosity and diffusion coefficients are constant across the whole of the model domain. In a region as variable as the tropical/extra-tropical Pacific it would be surprising if this were to be the case. One process that has the potential of impacting on the larger scale dynamics of the region is the interleaving of water masses across the equator (see Richards and Banks (2002)). The interleaving is confined to a few degrees either side of the equator. Richards (1998) argues that the effective diffusion is of order 1.0×10^3 m^2s^{-1}, large enough to affect the dynamics of the system (c.f. Maes *et al.* (1997)) and indeed shown to do so in idealized studies such as Banks (1997) and Richards and Edwards (2003).

Another feature of the equatorial Pacific is the presence of Tropical Instability Waves

(TIWs) on the eastern side of the Pacific (e.g. Legeckis (1977), Chelton *et al.* (2000)), which contribute to the heat budget of the cold tongue. The energetics of the TIW activity has been analyzed in an OGCM by Masina *et al.* (1999) at a fixed value of viscosity and tracer diffusion coefficients. The waves are affected by the prescribed mixing parameterization, however, the sensitivity of the wave activity to the form of the mixing parameterization needs to be ascertained.

The purpose of this chapter is to investigate the sensitivity of both the mean state and TIW activity of the equatorial Pacific to the strength and form of the mixing parameterization. This investigation should be viewed as an extension of the work of Maes *et al.* (1997) and Lengaigne *et al.* (2003). We choose, however, to study the sensitivity of the system in a rectangular domain with idealized forcing to simplify the interpretation of the results. The rest of the chapter is organized as follow. In Section 2.2 the model configuration, parameterization and experimental setup are described. In Section 2.3 the model sensitivity to the magnitude, orientation, grid resolution and form of the mixing are analyzed. The meridional heat transport is analyzed in Section 2.4, model energetics is investigated in Section 2.5 and the effects on TIW characteristics are considered in Section 2.6. A summary and conclusions are presented in Section 2.8.

2.2 Model configuration and experiments performed

OPA is a numerical ocean general circulation model (OGCM) designed for oceanic studies and its interactions with other components of the climate system i.e. atmosphere, sea-ice and biogeochemical tracers. This model has been used in many fields of oceanographic and climatic research and an extensive reference list of OPA applications can be found in Madec *et al.* (1998).

The variables are distributed on a three dimensional Arakawa C type grid using prescribed horizontal (Z) levels. This OGCM solves the primitive equations following Bryan (1969) as referred in Madec *et al.* (1998) with a large variety of physical options and the prognostic variables are the three dimensional velocity field and thermohaline variables. A leapfrog three-level centered time differencing scheme is used for non-diffusive processes.

The first time step of this three level scheme when starting from an ocean at rest is a forward step. The numerical techniques used to solve the primitive equations are based on the centered second order finite difference approximation. A full description with all model formulations can be found in Madec *et al.* (1998). A brief description of the model and configurations are presented as Appendix A and B.

For this study the model is configured in a rectangular equatorial domain, without bottom topography. The domain covers a region extending from 31°S to 31°N and 120° in longitude (arbitrarily referred to as 1° to 120°, from west to east) resembling the tropical Pacific ocean. All lateral boundaries are closed using no-slip conditions. The model grid is stretched within the equatorial region and over the westernmost region of the domain to better resolve the equatorial current system and the western boundary currents, respectively, when a coarse grid resolution is used. We choose to use two grid resolutions. For the coarser of the two, the grid spacing in the meridional direction is 1/2° between 5°S and 5°N, increasing to 2° by 10°S(10°N). The zonal grid spacing is 1/2° at the western boundary increasing to 1° by longitude 10°, and remaining at this grid spacing over the rest of model domain. The fine grid resolution version has 1/4° in the zonal direction covering all the domain and in the meridional direction it has 1/4° within the equatorial region extending from 5°S to 5°N increasing to 1° towards the northern and southern boundaries. There are 31 levels in the vertical, with the highest resolution of approximately 10 meters in the top 150 meters. Below this depth the resolution decreases down to 500 meters near the ocean bottom at 5000 meters depth, for both coarse and fine grid resolutions. Vertical mixing is computed using a prognostic turbulent kinetic energy (TKE) equation (Blanke and Delecluse, 1993). The majority of the results presented here are from experiments using the fine grid resolution. We compare the results of experiments with the fine and coarse grid resolution to give an indication of the effects of grid resolution.

All experiments are forced by Hellerman and Rosenstein (1983) climatology, zonally averaged monthly mean wind stress over the Pacific ocean basin mapped onto the model domain. Temperature and salinity are initialized from zonally averaged values Levitus and Boyer (1994) and the ocean starts from rest. Sea Surface Temperature (SST) and Sea Surface Salinity (SSS) are restored towards zonally averaged climatological observations (Levitus and Boyer, 1994). The results are analyzed after the 4^{th} year of integration when

the upper ocean solutions have reached a statistically quasi-steady state.

The experiments carried out with the fine resolution model are shown in Table 2.1 and they are split in two groups according to the lateral mixing orientation applied. In the first group, four experiments have tracers and momentum mixed along horizontal (HOR) surfaces and in the second group tracers and momentum are mixed along isopycnic surfaces (ITM). The momentum and tracer diffusivity are set to be the same and are referred for simplicity as A_h. In this study different diffusion regimes are imposed to each experiment with the eddy viscosity and diffusivity coefficients varying from high to low values. In the first three regimes, the A_h used is $4.0 \times 10^3 \mathrm{m^2 s^{-1}}$, $2.0 \times 10^3 \mathrm{m^2 s^{-1}}$ and 4.0×10^2 $\mathrm{m^2 s^{-1}}$, respectively.

SFC	Name	A_h	SST_c	EUC_{max}	MKE_{avg}	EKE_{avg}
HOR	Hor301	4.0×10^3	21.85	63.13	15.49	1.89
	Hor302	2.0×10^3	21.72	88.14	22.30	4.33
	Hor303	4.0×10^2	22.01	133.53	34.80	19.17
	Hor304	$4.0 \times 10^2 + 2.0 \times 10^3$	21.99	81.20	23.10	9.18
ITM	Itm301	4.0×10^3	21.42	83.81	24.84	4.26
	Itm302	2.0×10^3	21.60	97.34	28.38	8.65
	Itm303	4.0×10^2	21.92	130.38	38.89	25.19
	Itm304	$4.0 \times 10^2 + 2.0 \times 10^3$	21.71	86.10	26.63	16.10

Table 2.1: Description of the numerical experiments performed, where the columns represents: Lateral mixing orientation (HOR means horizontal mixing and ITM isopycnal mixing for tracers and momentum), experiment names, mixing coefficients (A_h, units are in $\mathrm{m^2 s^{-1}}$), SST_c averaged over the Cold Tongue region (°C) extending from 6°N to 6°S and 90° to 119° of longitude, EUC maximum value (cm $\mathrm{s^{-1}}$), mean (MKE) and eddy kinetic energy (EKE) averaged zonally over the whole domain, from 8°N to 8°S and over the top 270m (units are $\mathrm{m^2 s^{-2}}$).

In the fourth regime a parameterization based on a representation of interleaving is applied. Our knowledge and understanding of interleaving in the equatorial Pacific is still far from complete, as stated by Richards (1998), and, because of relatively high levels of mixing and limited vertical resolution, interleaving is not represented in OGCMs. In the equatorial Pacific, the fresher water to the north of the equator and the salty water to the south are often observed to interleave. The intrusive features (layers) generated in the frontal region between these two water masses can have a meridional scale of O(100 Km) and a vertical scale of O(10 m) as shown in Richards and Banks (2002).

Richards and Edwards (2003) consider ways of parameterizing the effects of interleaving in OGCMs. As they remark, the most appropriate form for the parameterization depends on the physical mechanism for the formation of the layers and the controls limiting layer growth. Here, as a first step in accessing the importance of interleaving on the large scale dynamics of the equatorial ocean, we will assume that the interleaving acts in a diffusive manner on the large scale. Estimates of an effective lateral diffusion coefficient caused by interleaving are of O(10^3 m^{2}s^{-1}), according with McPhaden (1985) and Richards and Banks (2002). A rationale for increasing the lateral mixing in the vicinity of the equator is assumed. The choice of the functional form for the meridional dependence of the enhanced mixing is somewhat arbitrary. We require a function that reduces to zero away from the equator (a Gaussian has this property) and that the lateral diffusion coefficient can be written as

$$A_h = A_0 + A_{add} e^{\frac{-y^2}{L^2}} \tag{2.1}$$

where A_0 is a constant background diffusion coefficient (here taken to be 4.0×10^2m^{2}s^{-1}) and A_{add} represents the effect of interleaving on the large scale fields of velocity and tracers. The effect of interleaving is chosen to be maximum on the equator decreasing away from the equator on a length scale of L (with $L = 2°$ of latitude). The dependency of A_{add} on the state of the ocean depends very much of the assumptions made for the processes controlling the interleaving (see Richards (1998)). However we can estimate A_{add} to be of order O(1.0×10^3 m^{2}s^{-1}). Here we will set $A_{add} = 2.0 \times 10^3$ m^{2}s^{-1}.

Name	A_h	Std_{max}	c_T
Itm301	4.0×10^3	0.16	29
Itm302	2.0×10^3	0.30	23
Itm303	4.0×10^2	0.43	24
Itm304	$4.0 \times 10^2 + 2.0 \times 10^3$	0.43	23

Table 2.2: Table showing diagnostics statistics. First column are experiment names and second are the lateral mixing coefficients used in the experiments, units are m^{2}s^{-1}. Third column, maximum standard deviations at 4°N along of all model domain (units are in °C). Fourth column is showing the maximum wave propagation speed c_T obtained with Radon Transform (units are in cm s^{-1}).

Table 2.1 lists not only the experimental details but also, for comparison, a number of

model diagnostics: area averaged Sea Surface Temperature (SST_c) within the cold tongue region, extending from 6°N to 6°S and 90° to 119° of longitude, and the mean (MKE) and eddy kinetic energy (EKE) zonally averaged over the whole domain, from 8°N to 8°S and over the top 270m. The results presented in both Tables 2.1 and 2.2 are discussed later.

2.3 Mean State Analysis

2.3.1 The equatorial current system

The zonal component of the annual mean velocity between 10°S and 10°N of latitude in the eastern region of the basin at 97° longitude is shown in Figure 2.1 for varying A_h and mixing orientation. All model experiments are able to reproduce the gross features of the equatorial current system (see Wyrtki and Kilonsky (1984) for a rough comparison); the two (northern and southern) branches of the South Equatorial Current (SEC) in the upper ocean flowing westward, the EUC flowing eastward with its maximum at the equator and the North Equatorial Counter Current (NECC) between 6°N and 8°N (refer to Table 2.1 for the maximum values of the EUC).

The current magnitudes simulated are overestimated when compared with observations shown in Wyrtki and Kilonsky (1984). They have shown a mid Pacific annual mean cross-section for the period April 1979 to March 1980. The EUC maximum speed is around 55 cm s^{-1} and the core 140 meters depth, approximately.

The model equatorial current system is found to be very sensitive to the level and form of lateral mixing. Decreasing the magnitude of the lateral mixing coefficient by one order of magnitude increases the strength of the EUC by 100% (Figure 2.1a-d) with the EUC being narrower with lower values of diffusivity. Likewise, the strength of the SEC and NECC increase with decreasing A_h, with an associated deepening of both currents.

Figure 2.2 shows the SST_c and EUC_{max} plotted for all lateral mixing coefficients used in the experiments. It should be noted that the additional mixing experiments (with A_h given by Equation 2.1) are plotted using an abscissa value of $A_h = 2.4 \times 10^3$ $m^2 s^{-1}$. We note two points from the general behavior of the system. The first is that although the SST_c is

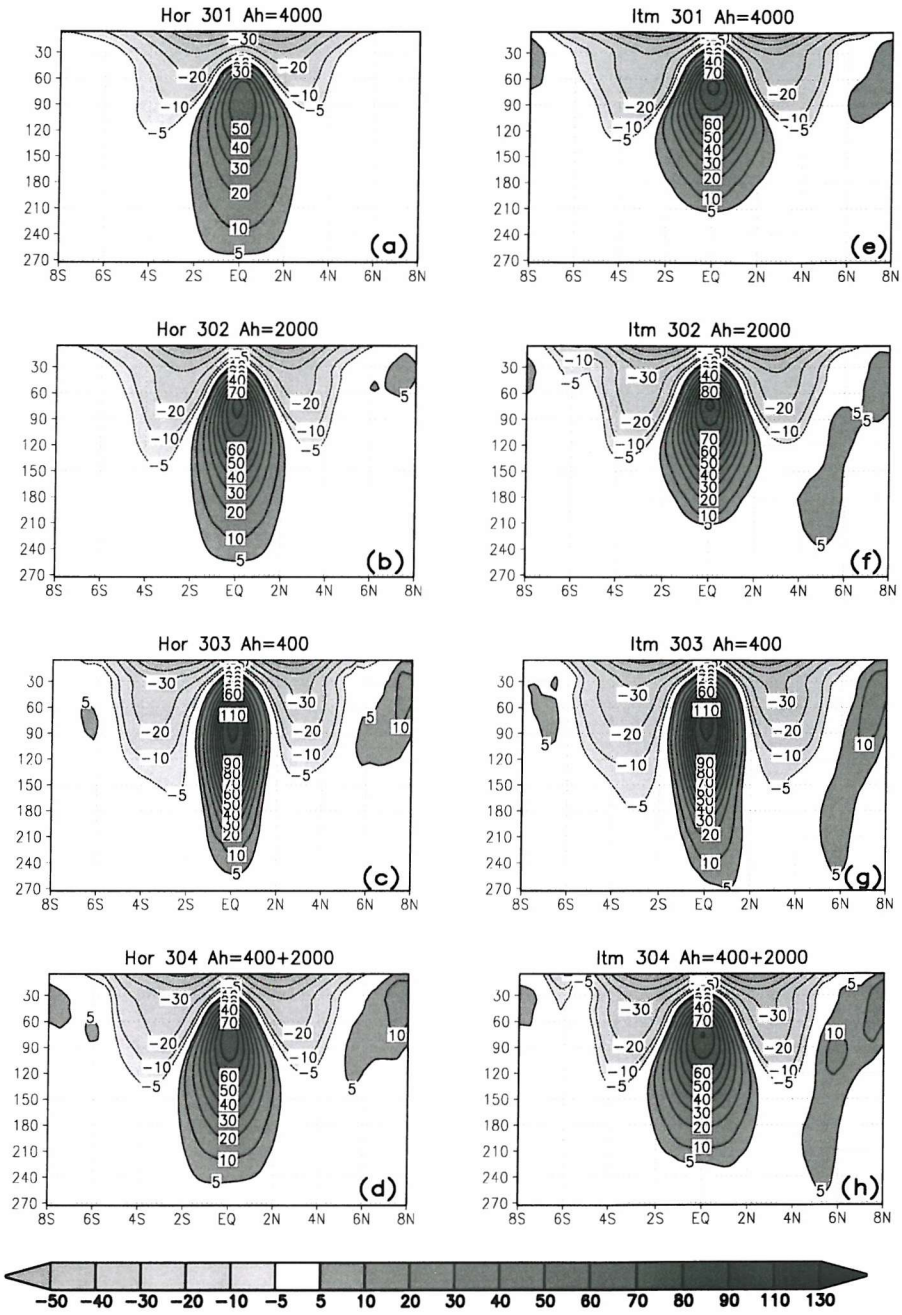

Figure 2.1: Vertical section at 97° of longitude of the zonal velocity component, u, for the fine grid resolution experiments. Left column shows the experiments where tracer and momentum are mixed along horizontal surfaces (HOR), and right column tracer and momentum being mixed along isopycnals (ITM). A_h is the lateral mixing coefficient applied on the experiments. Units are in cm s^{-1}.

greatest for the lowest value of A_h there is not a monotonic increase with decreasing A_h for all series of experiments. The second is that, perhaps reassuring, the points tend to cluster for the lowest value of A_h for SST_c and EUC_{max}. In other words, the characteristics of the model become less dependent on the formulism of lateral mixing and grid spacing at small values of diffusivity.

With regards to the kinetic energy of the system we see, as expected, an increase in the mean kinetic energy (MKE) and eddy kinetic energy (EKE) when A_h is decreased (see Table 2.1). It is worth noting that the vertical transport was not found to vary significantly as the lateral mixing coefficients are varied, by analyzing the annual zonal mean of the meridional overturning circulation between 10°N and 10°S. According to (Maes *et al.*, 1997), this is a convenient way to quantify the impact of the lateral mixing on the meridional circulation and its link to the vertical circulation. However, our results are in contrast to Maes *et al.* (1997) who find that the strength of the meridional cell decreases as the lateral mixing coefficients are decreased, caused by an associated increase in the vertical mixing. In our case the only significant change is a modest increase of around 10% in the vertical transport when the enhanced mixing is applied. The precise reason why we see a smaller variation in the strength of the meridional cell with the value of lateral mixing is unclear, but presumably is related to a smaller variation in vertical mixing.

2.3.2 Mixing orientation

In general, the experiments with the mixing of tracers and momentum (ITM) along isopycnic surfaces produce stronger currents, increasing the EUC velocity and both north and south branches of the SEC and also a better defined NECC compared with experiments when tracers and momentum are mixed horizontally (HOR) (see in Figure 2.1 and Table 2.1). We find, in accord with Lengaigne *et al.* (2003), that rotating mixing to be along isopycnic surfaces reduces the effective diapycnal diffusion. This gives stronger density gradients, producing a tighter pycnocline accelerating the equatorial current system.

However the differences between experiments with different mixing orientation are dependent on both the level of mixing and the numerical grid. For instance the percentage increase of the EUC_{max} gain from horizontal to isopycnic mixing is 31%, 10% and -2%,

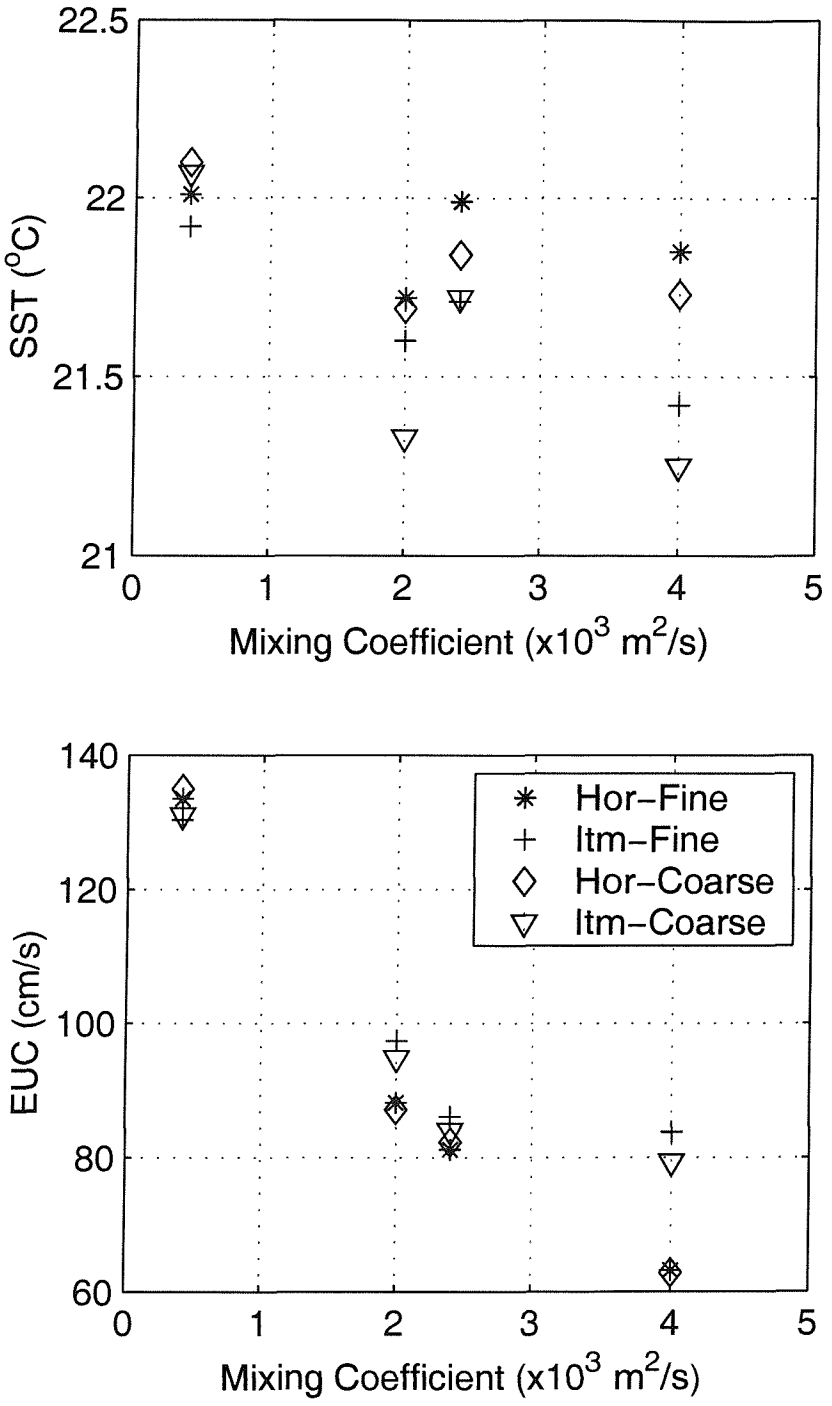

Figure 2.2: Gross properties of the model solutions: [a] SST averaged over the cold tongue region (extending from 6°N to 6°S and 90° to 119° of longitude) plotted against A_h for all experiments; [b] EUC_{max} plotted against A_h for all experiments. Note that symbols plotted at $A_h = 2.4 \times 10^3$ m^{2}s^{-1} correspond to the additional lateral mixing experiments

for $A_h = 4.0 \times 10^3$ m^{2}s^{-1}, $A_h = 2.0 \times 10^3$ m^{2}s^{-1} and $A_h = 4.0 \times 10^2$ m^{2}s^{-1} respectively. Note that the EUC with isopycnic diffusion slows down slightly (compared to horizontal diffusion) for the low diffusion case. We also note that the differences in the SST of the cold tongue, SST_c for horizontal and isopycnic mixing and with $A_h = 2.0 \times 10^3$ m^{2}s^{-1} is 0.4°C for the coarse grid experiments but only 0.1°C for the fine grid experiments.

2.3.3 Enhanced equatorial mixing

The results of the experiments with enhanced mixing restricted to a few degrees either side of the equator show that the system is sensitive to such mixing, where here we are taking the enhanced mixing to be representative of the interleaving of water masses. Solutions with enhanced equatorial mixing (see Figure 2.1d and h) are somewhat intermediary between those with moderate and low (but constant) diffusion. For instance the enhanced equatorial mixing keeps the core speed of the EUC to a modest value, whilst the speed of the flow away the equator (e.q. the NECC) is now similar to that of the low diffusion case (see Table 2.1). The MKE of the enhanced mixing case is similar to that with a constant $A_h = 2 \times 10^3$ m^{2}s^{-1}. This is not so for the EKE which has significantly higher values for the enhanced mixing case. The characteristics of the eddy field will be discussed further in Section 2.5.

The strength of the EUC with enhanced equatorial mixing is consistent with the speed we could expect with a constant diffusivity coefficient (see Figure 2.2b). However the average SST of the cold tongue region, SST_c, is elevated above that for the equivalent constant A_h case, by as much as 0.5°C of the experiment with the coarse grid and isopycnic mixing (Table 2.1). Although the raise in the average SST is smaller for the other experiments, locally there are similar O(0.5°C) increases over an appreciable area in all experiments. This increased value of SST_c is brought about by the enhanced tropical instability wave activity allowed by the reduced levels of diffusion away from the equator (see Section 2.6).

2.4 Meridional Heat Transport

A primary condition for an OGCM be a good tool to couple with an atmospheric model is its capacity to represent the equatorial thermal structure since the surface layers will

have a strong impact on the atmospheric circulation, e.g the ENSO phenomenon. The ocean-atmosphere system is a large heat engine where the sun is the main source of energy. A great part of this incoming heat is redistributed in the ocean by the wind generated currents, transient systems and the thermohaline circulation.

Here we will consider the integrated meridional heat flux across a zonal section (x - longitude vs z - depth) of the basin, given by

$$MHT_{Tot} = \rho_0 C_p \int \int v\theta dxdz \tag{2.2}$$

where, x extends over the whole longitudinal domain, z extends from surface down to 270 m depth, MHT_{Tot} is the total meridional heat transport, v the meridional velocity, θ potential temperature, ρ_0 the mean sea water density (taken to be 1000 kg m^{-3}) and C_p is the specific heat capacity, (4093 Jkg^{-1} $^\circ$ K^{-1}). The diffusive heat flux is not analyzed. The contributions by the time mean and eddy components of the flow can be calculated by decomposing v and T into their time mean and fluctuating components, respectively i.e. $v = \overline{v} + v'$ and $\theta = \overline{\theta} + \theta'$ and substituting in Equation 2.2. Thus mean and eddy components of the meridional heat transport are given by

$$MHT_{Mean} = \rho_0 C_p \int \int \overline{v}\overline{\theta} dxdz \tag{2.3}$$

and

$$MHT_{Eddy} = \rho_0 C_p \int \int v'\theta' dxdz \tag{2.4}$$

respectively.

The mean and eddy meridional heat fluxes using the fine grid resolution are shown in Figure 2.3, respectively. Similar characteristics are displayed by the coarse grid model (not shown). The analysis is done for the largest, smallest diffusivity coefficients and additional mixing experiments, namely $A_h = 4.0 \times 10^3$ m^2s^{-1}, $A_h = 4.0 \times 10^2$ m^2s^{-1} and $A_h = 2.0 \times 10^3$ $m^2s^{-1} + 4.0 \times 10^2$ m^2s^{-1}, respectively. The heat gained by the equatorial ocean at the surface is transported poleward and the mean heat flux is larger in the northern hemisphere compared with that in the south. As shown in previous studies (Hastenrath, 1982, Philander, 1990), the Pacific ocean has a characteristic of poleward heat transport because the meridional equatorial currents are composed of a strong divergence in the surface layers

and subsurface convergence underneath, moving warm surface waters poleward while colder waters return equatorward, mainly within the thermocline region (Philander, 1990).

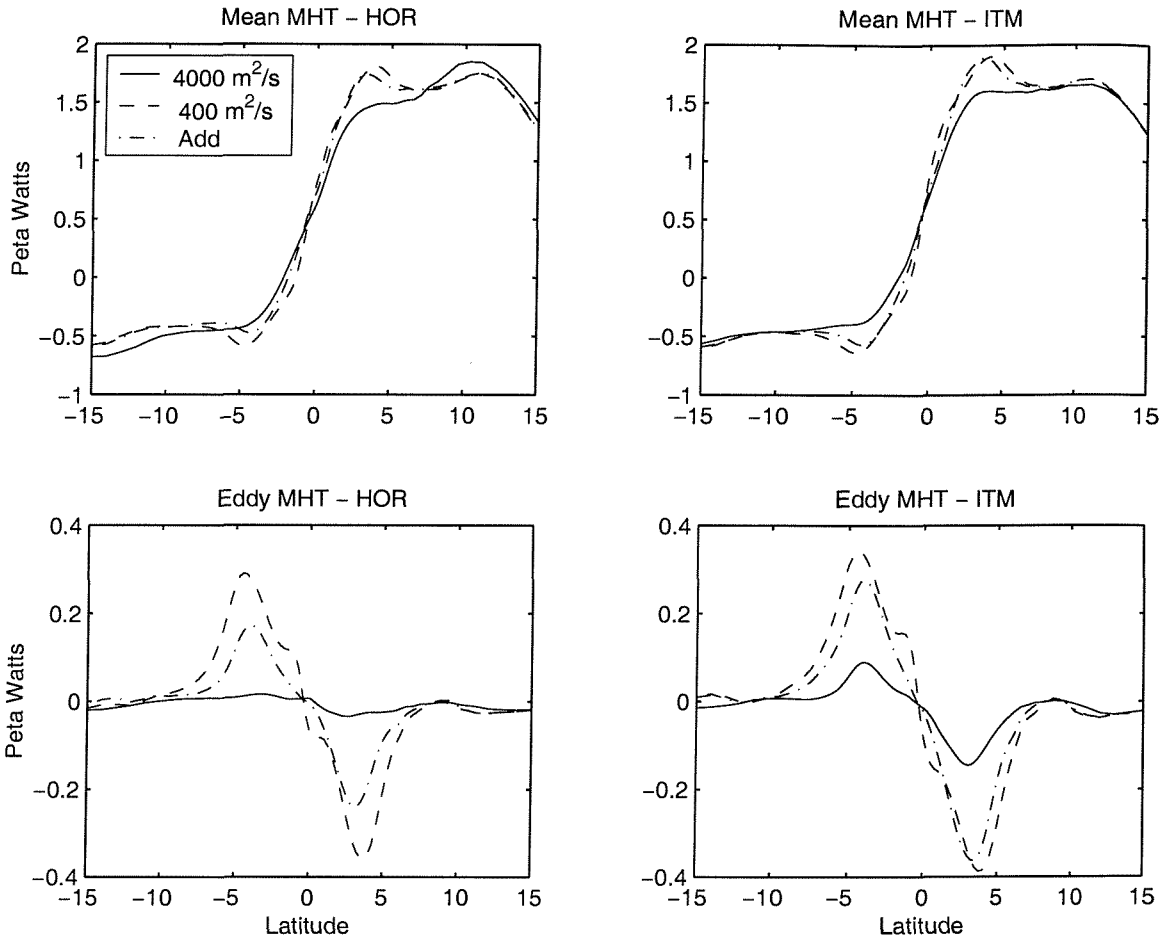

Figure 2.3: Meridional Heat Transport (units are 10^{15} Watts) for the fine grid resolution experiments. HOR, mixing tracer and momentum along horizontal surface and ITM mixing tracer and momentum along isopycnal surface: solid line, $A_h = 4.0 \times 10^3$ m^2s^{-1}; dashed line, $A_h = 4.0 \times 10^2$ m^2s^{-1}; dashed–dot line, Additional mixing experiment. Units are 10^{15} Watts.

The mean meridional heat flux in the experiments performed with the fine grid resolution using different mixing coefficients show small differences between them (Figures 2.3 a and c). There is an asymmetry in the heat flux with the region of no net meridional flux located at 3°S. The largest differences between the experiments are located between 0 and 5°N in the region where the TIWs occur, and for the high diffusion case around 10°N with tracers and momentum being mixed along horizontal surfaces. The high diffusivity horizontal mixing experiment shows a single peak in the mean heat flux occurring around 10°N. As the lateral

mixing coefficient is decreased the mean heat flux is increased within the TIW region giving a second peak.

As the diffusivity is increased the eddy heat transport, which fluxes heat down gradient towards the equator is reduced as the eddies (and TIWs) are damped (Figures 2.4b and d). This effect is strongest with horizontal mixing when $A_h = 4.0 \times 10^3$ m^{2}s^{-1}, with the eddy transport almost completely damped out. The maximum difference in eddy heat flux between the highest and lowest diffusion cases reaches almost 0.4 PW. There is corresponding change in the amplitude of the mean heat flux. Generally the eddy heat fluxes are larger for the isopycnic mixing cases with the difference between horizontal and isopycnic mixing being reduced as the diffusion coefficient is reduced. The magnitude of the eddy flux peaks at around 4°N and 4°S with indications of a secondary peak (or at least shoulder) forming closer to the equator as the diffusivity is reduced.

2.5 Energetics

2.5.1 Kinetic Energy Distribution

In an effort to understand and evaluate the energetics of the mean state and transients generated in the numerical experiments a kinetic energy analysis is performed. Analogous to the heat flux analysis, we divide the total kinetic energy, K_t, into the time mean kinetic energy, $\overline{K}_m$, and eddy kinetic energy, K_e. Thus,

$$K_t = \overline{K}_m + K_e \tag{2.5}$$

where

$$K_t = \frac{1}{2}\rho(u^2 + v^2),$$

$$\overline{K}_m = \frac{1}{2}\rho(\overline{u}^2 + \overline{v}^2),$$

and

$$K_e = \frac{1}{2}\rho(u'^2 + v'^2) \tag{2.6}$$

In this case, the time mean is taken over the last year of the experiments.

Figure 2.4 shows a vertical section of the kinetic energy in the eastern part of the domain at 97° of longitude. Shaded areas represent $\overline{K}_m$, while K_e is represented by solid lines. The K_e indicates the region where the energy of the eddies (here associated with TIW activity) are located while the $\overline{K}_m$ represents the energy structure of the mean flow. The analysis is performed in the first 270 meters of depth since the major eddy activity is confined within this depth. In all cases the most energetic region is between approximately 6°S and 6°N and is where the strongest gradients in the equatorial currents and temperature occur. The most energetic regions of the mean state are where the EUC and SEC north and south branches are located. $\overline{K}_m$ is increased when the diffusivity is reduced, following the same pattern as the EUC and SEC velocity and also showing largest values for the experiments performed with the fine grid resolution as shown in Figure 2.4 when compared with the coarse resolution ones (not shown). The distribution of K_e has a maximum at the surface and from there the energy decreases splitting downwards into two energetic branches. One goes down between the EUC and southern SEC branch in a region of strong shear between these two currents. The northern branch of K_e is slightly more energetic than the southern and is in the region between the EUC and SEC northern branch. For a given diffusion coefficient both the mean and eddy kinetic energy are greatest when tracers and momentum are mixed along isopycnals (Figures 2.4e to h), following the same pattern as the current speed. For instance when $A_h = 2.0 \times 10^3$ m^{2}s^{-1} (Figure 2.4f) K_e is twice as large (having a maximum of 50 m^{2}s^{-2}) when compared with the horizontal mixing on Figure 2.4b (maximum of 25 m^{2}s^{-2}).

There is a marked change in the distribution of eddy kinetic energy as the diffusion coefficient is reduced to $A_h = 4.0 \times 10^2$ (Figures 2.4c and g). At higher values of A_h there are maxima in K_e either side of the equator (the greater being towards the north). For the lowest value of A_h there is now an intense maximum centered on the equator with subsurface maxima to the north and south. With enhanced mixing close to the equator (Figure 2.4d and h) the equatorial maximum in K_e is eradicated, but the northerly and southerly subsurface maxima remain. In this case, the level of eddy activity away from the equator is actually increased and more widely spread when compared to that for a constant $A_h = 2.0 \times 10^3$ m^{2}s^{-1} (Figures 2.4b and f). It might be consequence of the lower mixing used away from the equator.

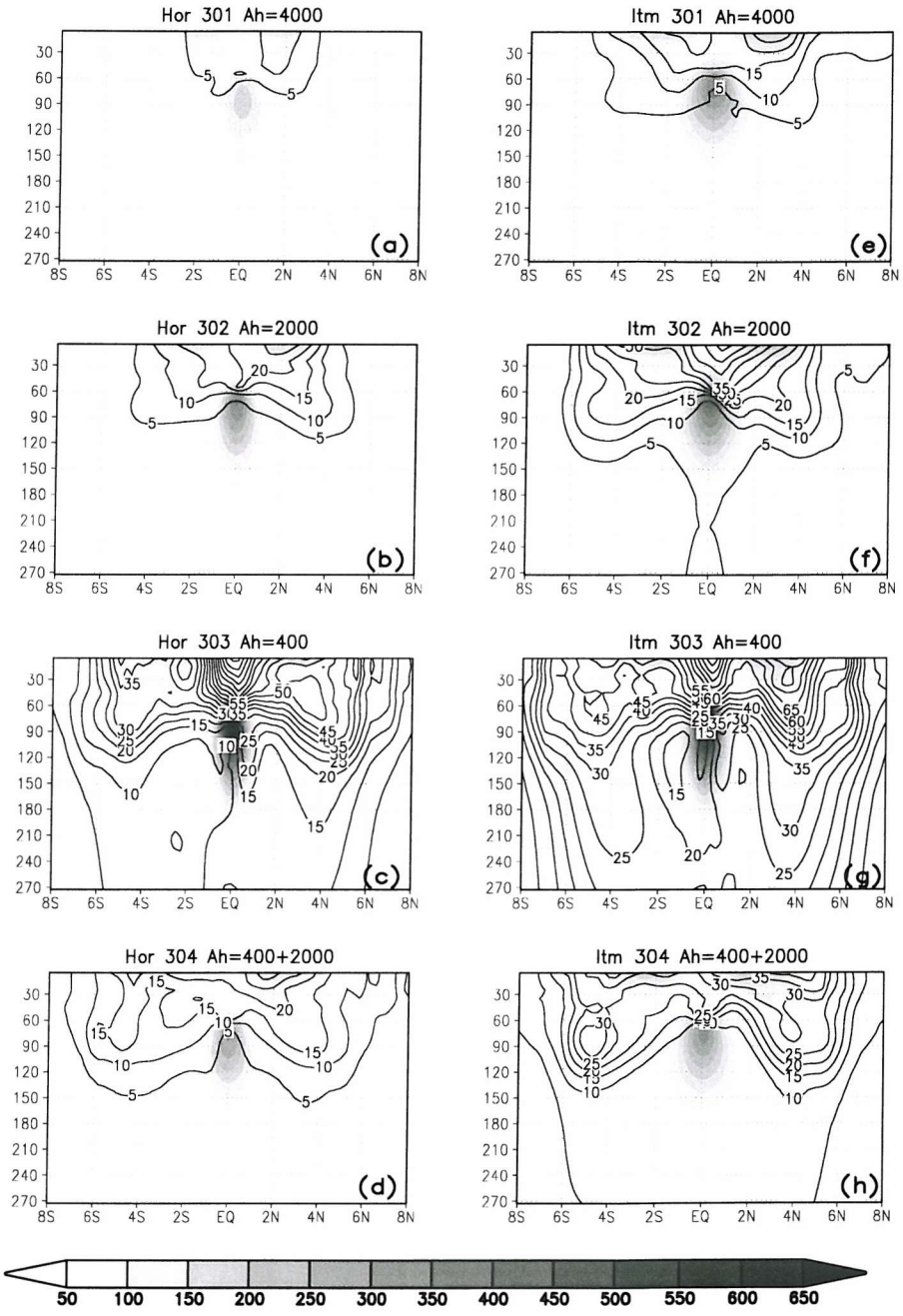

Figure 2.4: Mean Kinetic Energy (MKE) shaded and Eddy Kinetic Energy (EKE) for the fine model grid resolution experiments. Horizontal mixing for tracers and momentum (HOR) are shown in the left column and isopycnal mixing (ITM) in the right column. Units are m^2s^{-2}

2.5.2 Energy transformation analysis

Strong current shear and temperature gradients occur within the tropical Pacific region and as a consequence TIW's are generated in this region. However the generating mechanism for these waves is not completely understood and is still under discussion by the scientific community. Barotropic instability, initiated by the shear between the EUC and SEC, also between the EUC and NECC is attributed as an important mechanism for TIW generation (Luther and Johnson, 1990, Qiao and Weisberg, 1998). However these waves have other processes contributing to their generation, such as baroclinic instability, as argued by Luther and Johnson (1990) and Masina *et al.* (1999), acting as a trigger mechanism further north and south of equator.

In this section we analyze the energetics of the model experiments simulated using different mixing regimes. To analyze the influence and energy source of the equatorial waves the barotropic and baroclinic production terms of the eddy kinetic energy equation are computed, following a similar approach used by Masina *et al.* (1999). For the sake of brevity only the dominant terms in the eddy kinetic energy equation will be discussed here. The full equations can be found in Masina *et al.* (1999).

The eddy kinetic energy equation is

$$\begin{aligned}
&\frac{\partial K_e}{\partial t} + \overline{\mathbf{u}} \cdot \nabla K_e + \overline{w} K_{ez} + \mathbf{u}' \cdot \nabla K_e + w' K_{ez} = \\
&- \quad \mathbf{u}' \cdot \nabla p' + \rho_0 [-\mathbf{u}' \cdot (-\mathbf{u}' \cdot \nabla \overline{\mathbf{u}}) - \mathbf{u}' \cdot (w' \overline{\mathbf{u}_\mathbf{z}}) \\
&+ \quad \mathbf{u}' \cdot (\overline{\mathbf{u}' \cdot \nabla \mathbf{u}'}) + \mathbf{u}' \cdot (\overline{w' \mathbf{u}'}) \\
&+ \quad A_h (\mathbf{u}' \cdot \nabla^2 \mathbf{u}') + \mathbf{u}' \cdot (A_v \mathbf{u}'_z)_z]
\end{aligned} \tag{2.7}$$

where K_e is the eddy kinetic energy, $\mathbf{u} = u\hat{\mathbf{x}} + v\hat{\mathbf{y}}$, the horizontal velocity vector, and ∇ is the horizontal divergence. The terms on the left hand side of (Equation 2.7) represent the local tendency, and horizontal and vertical advection of K_e by the time mean and fluctuating flow, respectively. The first term on the right hand side of (Equation 2.7) represents the pressure work divergence done by the eddies that tend to redistribute the kinetic energy spatially. The second and third terms are the barotropic energy conversion terms between the mean

flow and eddies through deformation work. The fourth and fifth represent the divergence of K_e by the fluctuating velocity field. The two last terms represent the horizontal and vertical eddy dissipation. Calculation of the various terms is made from a time series of instantaneous fields taken every five days with the time mean (given by an overbar) taken as the annual average. The conversion of mean kinetic energy into eddy kinetic energy occurs when the horizontal or vertical deformation work terms in (Equation 2.7) are positive, respectively. The horizontal deformation term of (Equation 2.7) is known as barotropic conversion whilst the vertical term is Kelvin-Helmholtz conversion.

Assuming the hydrostatic approximation, the eddy divergence pressure flux, $\mathbf{u}' \cdot \nabla p'$ in (Equation 2.7) can be written as (c.f. Masina *et al.* (1999))

$$\mathbf{u}' \cdot \nabla p' = -\nabla \cdot (\mathbf{u}' p') - (w' p')_z - g\rho' w' \tag{2.8}$$

The last term on the right hand side represents the conversion of mean available potential energy to eddy kinetic energy, K_e, i.e eddy kinetic energy is gained through the vertical deformation work. This term is known as the baroclinic conversion term and we restrict the baroclinic analysis to this term.

We find the dominant production terms in (Equation 2.7) are $-\rho(\overline{u'v'}\frac{\partial \overline{u}}{\partial y})$ in and $-g\overline{\rho' w'}$ (see Equation 2.8). Hereafter these terms are referred as the barotropic and baroclinic conversion terms, respectively. The other horizontal deformation work terms, e.g. $-\rho(\overline{u'u'}\frac{\partial \overline{u}}{\partial x})$ are smaller than the barotropic term and they are not considered here.

Horizontal sections at 5 meters depth (the upper level of the model) (Figure 2.5) show that there are three primary regions of eddy kinetic energy production. When $A_h = 2.0 \times 10^3$ m^{2}s^{-1} (Figure 2.5a), the barotropic conversion shows a maximum in the equatorial region and is related to the conversion of mean flow kinetic energy into eddy energy due to the meridional current shear. The magnitude and spatial distribution of the barotropic conversion are sensitive to the mixing scheme applied. As the mixing coefficient is decreased the barotropic conversion is increased as a consequence of the increase on the current shear (see for instance Figure 2.1). In the case where low mixing is used (Figure 2.5b), there is a considerable increase (more than a factor of two) in the production of K_e by barotropic conversion in the equatorial region as the EUC strengthens and tightens. For low A_h there is a secondary maximum of energy occurring just north of 4°N. This secondary maximum

is due to the stronger current shear between the SEC and NECC.

For the enhanced equatorial mixing case (Figure 2.5c) the pattern is different from either the high or low diffusion cases. The enhanced mixing suppresses the barotropic conversion on the equator, with an off-equator region of high values of conversion centered on 3°N (i.e. southward of that for low diffusion and somewhat to the west).

On the other hand, the pattern of the time mean baroclinic conversion term is relatively insensitive to the level of lateral mixing. Baroclinic conversion is strongest in the region where TIWs originate, just north (between 2°N and 5°N) and south (2°S and 5°S) of the equator. Note that the maximum value of the baroclinic conversion term is actually highest for $A_h = 2.0 \times 10^3$ m^{2}s^{-1} (Figure 2.5d). There is a strong interplay between the vertical and horizontal shear and the barotropic and baroclinic production of eddy kinetic energy.

The pattern and strength of the barotropic and baroclinic conversion terms with $A_h = 2.0 \times 10^3$ m^{2}s^{-1} are comparable to those found by Masina *et al.* (1999) in their experiments using a more realistic model domain and constant wind forcing. Here we find, however, that the production of eddy kinetic energy (particularly that brought about by barotropic instability) is very sensitive to the level and form of lateral mixing.

The vertical distribution of the time mean barotropic and baroclinic conversion terms in the eastern part of the domain (97° longitude) is presented in Figure 2.6. Overall, the changes in the patterns of barotropic and baroclinic conversion with respect to the level of lateral mixing are similar to those at the surface. But note that the maxima in values are generally subsurface between 40 to 60 m depth. The barotropic conversion is primarily produced by the shear between the EUC and the northern and southern limbs of the SEC. An exception is the surface maximum in barotropic conversion brought about by the shear between the SEC and NECC for low values of lateral mixing. The other noteworthy feature is the much greater depth penetration of the barotropic conversion when the lateral mixing is low close to the equator.

The energy conversion terms are shown as a function of time and depth in Figure 2.7. In each case we have averaged the conversion term over the 90° to 110° longitudinal band and between 8°S and 8°N. The general form of the baroclinic conversion term changes little as the lateral mixing is varied, it reaches a maximum around October with a secondary

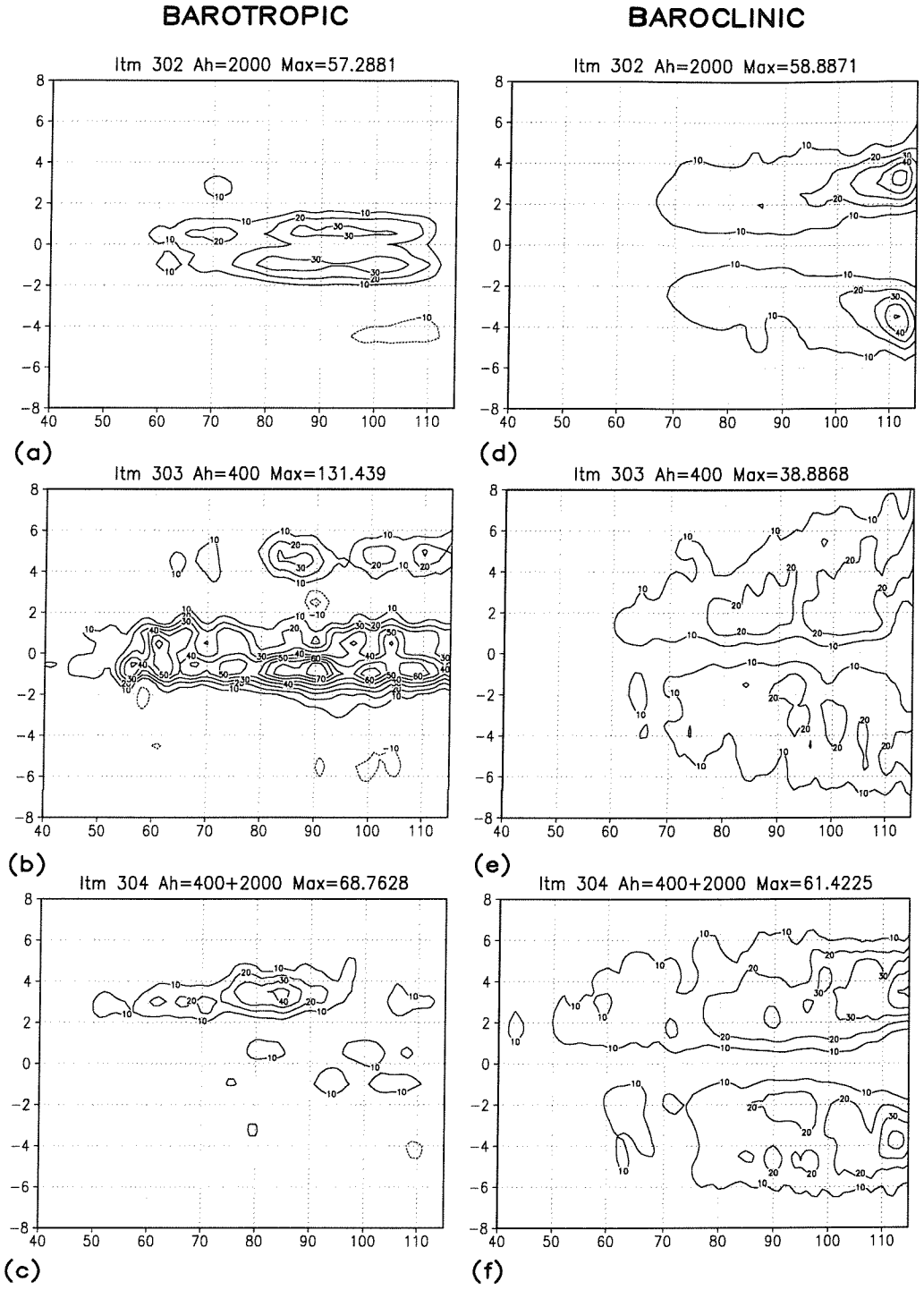

Figure 2.5: Horizontal sections at 5 meters depth of the time mean barotropic conversion term [a-c] and time mean baroclinic conversion term [d-f]. Experiments using $A_h = 2.0 \times 10^3$ m^{2}s^{-1}, $A_h = 4.0 \times 10^2$ m^{2}s^{-1} and additional mixing respectively. The units are in $\mu W m^{-3}$

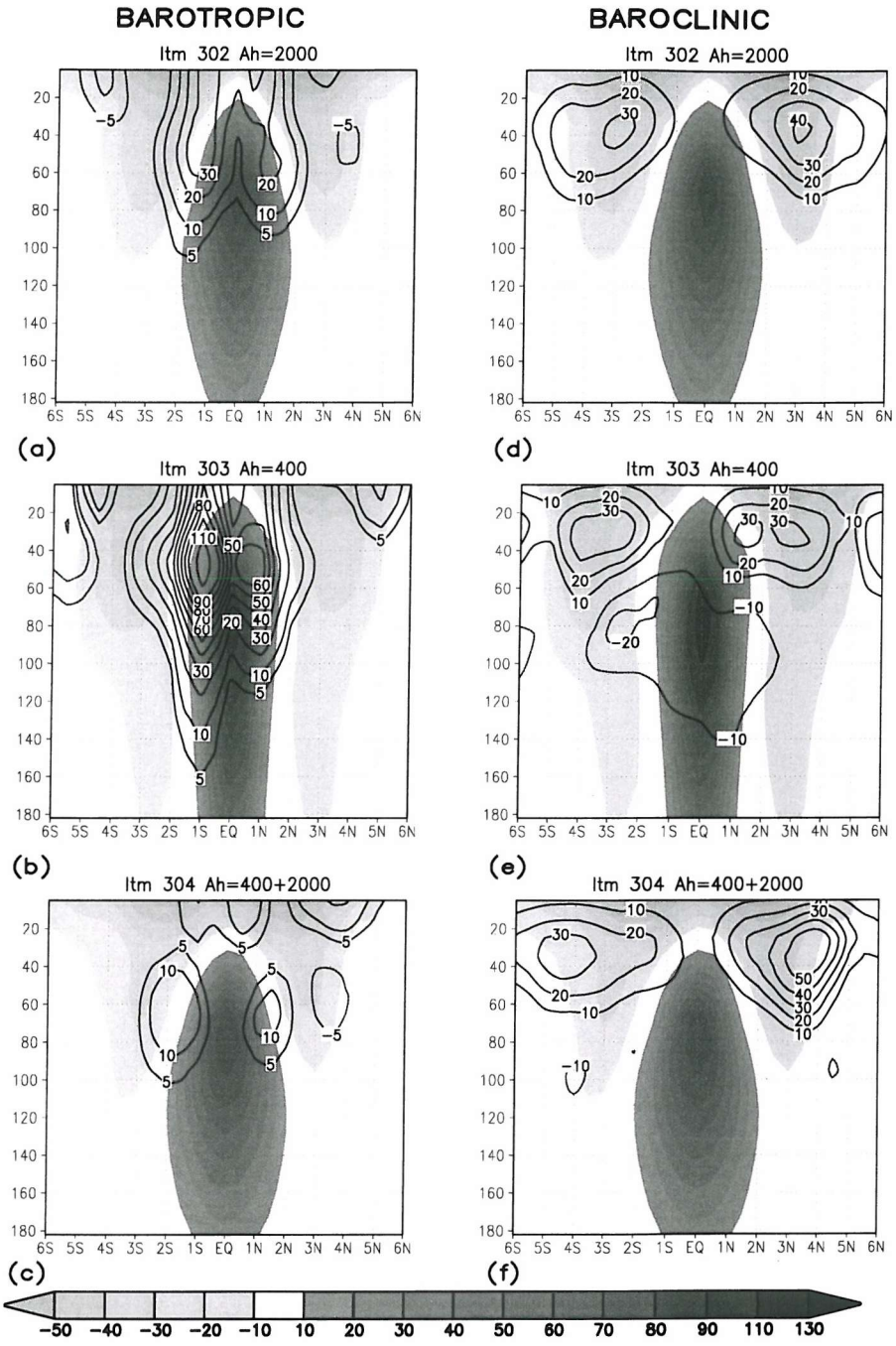

Figure 2.6: Vertical sections at 97° longitude of the time mean barotropic conversion term [a-c] and time mean baroclinic conversion term [d-f]. Experiments using $A_h = 2.0 \times 10^3$ m^{2}s^{-1}, $A_h = 4.0 \times 10^2$ m^{2}s^{-1} and additional mixing respectively. The units are in $\mu W m^{-3}$. Shaded regions show the zonal velocity component, units are in cm/s.

maximum around March. Both maxima are around 40m depth. Decreasing the lateral mixing coefficient has a tendency to shift both maxima by about a month earlier in the year, with an increase in the secondary maximum, and a slight reduction in the depth for which the term is positive. Interestingly, the secondary maximum has its largest value for the enhanced mixing case.

There are major changes to the barotropic conversion term. Again the major activity is around 40m depth. However, with $A_h = 2.0 \times 10^3 \mathrm{m}^2\mathrm{s}^{-1}$ the levels of the barotropic term are generally low except towards the end of the year, with the barotropic term peaking after the baroclinic term. With $A_h = 4.0 \times 10^2 \mathrm{m}^2\mathrm{s}^{-1}$ there is enhanced barotropic activity from the middle of June onwards, with a maximum before that of the baroclinic term, continuing through to April the next year, while for the enhanced mixing case the levels of barotropic activity are much reduced. The times with enhanced levels of baroclinic conversion correspond with times with high TIW activity. A more detailed analysis of the seasonality and spectral characteristics of the TIWs is done in the next section.

2.6 TIWs response to lateral mixing

In this section the characteristics of the model generated TIWs are examined as a function of the lateral mixing imposed in the model experiments. A comprehensive review of TIWs are shown in Chapters 3 and 4. The model is able to capture the basic observed characteristics of TIW activity and their seasonality. The waves in the model experiments are present between 2°N - 4°N and 2°S - 4°S within the eastern part of the domain and exhibit a well defined cusp-shaped wave pattern (not shown), typically extending from 70° to 120° of longitude. The most active model-generated TIWs are located north of the equator, coincident with the region of high levels of eddy kinetic and baroclinic conversion (see Section 2.5).

Here we examine the model TIW activity using time series of SST at 4°N during the last year of integration. To isolate and enhance the signal of the westward propagating features (TIW) a high-pass 2-D digital filter is applied. The digital filter used takes into account wavelength and period (see Cipollini *et al.* (2001) for filter details). In our case, TIWs are considered all oscillations with zonal wavelength ranging from 5° to 25° of longitude and

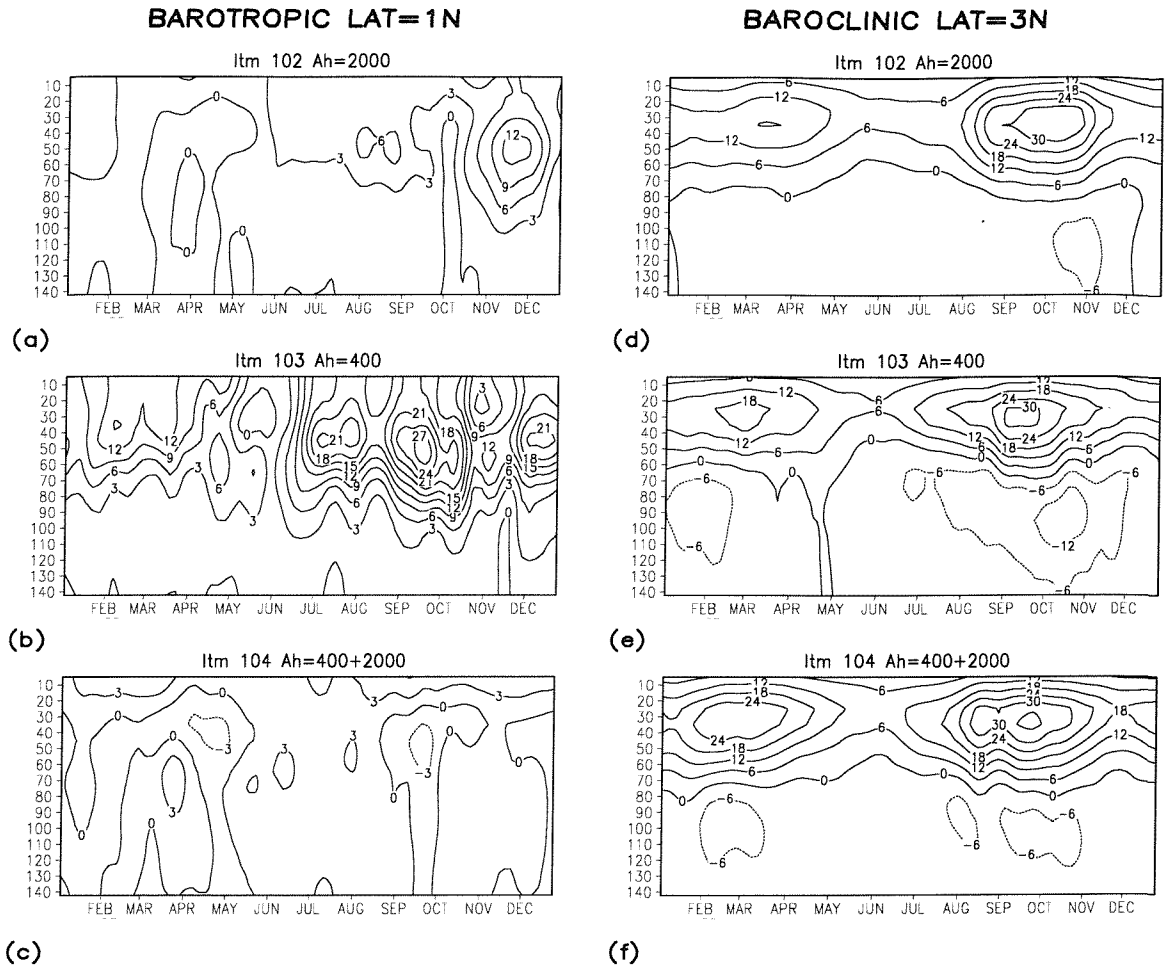

Figure 2.7: Time-depth sections of barotropic [a-c] and baroclinic [d-f] conversion terms, averaged over the 90° to 110° longitudinal band and between 8°S and 8°N. Experiments using $A_h = 2 \times 10^3$ m^{2}s^{-1} (upper panels), $A_h = 4 \times 10^2$ m^{2}s^{-1} (middle panels) and additional mixing (lower panels), respectively. The units are in $\mu W m^{-3}$.

period ranging from 10 to 60 days.

2.6.1 TIW activity

The resultant high-pass SST data are showed in Figure 2.8 as a Hovmöller (time-longitude) diagram for the fine grid resolution experiments when tracers and momentum are mixed along isopycnal surfaces. The TIW can be clearly identified in the time-longitude plots as westward propagating features whose amplitudes are modulated on seasonal time scale: the

most energetic period being the second half of the year and extending to the beginning of the following year. The properties of the TIWs are very sensitive, as is the mean state, to the level and orientation of the lateral mixing (Figure 2.8).

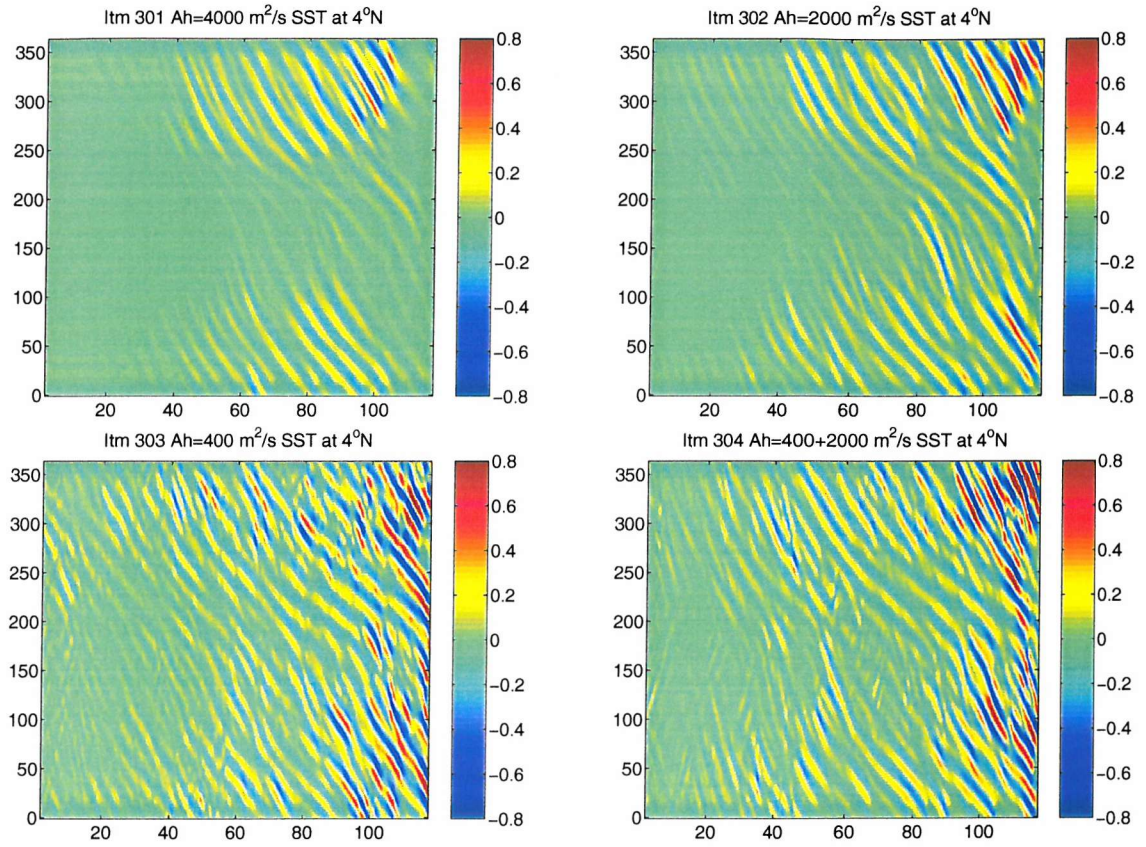

Figure 2.8: Filtered SST, displaying TIWs, at 4°N as a function of time (y-direction) and longitude (x-direction), for the fine model grid resolution experiments mixing tracers and momentum along isopycnal surfaces. Top left $A_h = 4.0 \times 10^3$ m^{2}s^{-1}, top right $A_h = 2.0 \times 10^3$ m^{2}s^{-1} , bottom left $A_h = 4.0 \times 10^2$ m^{2}s^{-1} and bottom right enhanced lateral mixing (Add) experiment, respectively. Units are °C.

Experiments using horizontal mixing for tracers and momentum tend to damp out the TIW activity (not shown) when compared with isopycnal mixing. Additionally, the waves are more intense and confined to the eastern part of the domain when both tracers and momentum are mixed along isopycnal surfaces. A large diffusivity tends to damp the wave activity producing more organized propagation patterns as well as confining the waves to the eastern portion of the domain, as showed in Figure 2.8 upper left panel. The experiment with $A_h = 4.0 \times 10^3$m^{2}s^{-1} produces the waves with smallest intensity (see Figure 4.6), with a maximum value of the standard deviation of 0.16 °C, compared with the other experiments

shown. As the mixing coefficient is decreased the waves become more energetic and their behavior more chaotic. For example consider the experiment with $A_h = 4.0 \times 10^2$ m^{2}s^{-1} (Figure 2.8, lower left panel). The TIW variability is increased over the full width of the domain, compared to experiments with a higher diffusivity, with the standard deviation reaching a maximum of 0.43°C (see Table 2.2) in the eastern part of the domain. However, note that the experiment with enhanced equatorial mixing produces waves which are slightly more energetic, but more confined to the eastern part of the domain, compared with the waves produced with lower mixing.

As mentioned in Section 2.5, there are changes to the seasonality of the TIW as a function of the mixing scheme. With a lower lateral mixing coefficient the TIWs tend to occur during the whole year as shown in the Figure 2.8, lower left panel. However, TIWs in the case with enhanced equatorial mixing have a seasonal cycle similar to the experiment using $A_h = 2.0 \times 10^3$m^{2}s^{-1}, displaying two periods in the year with large activity and one intermediate period in the middle of the year with less activity.

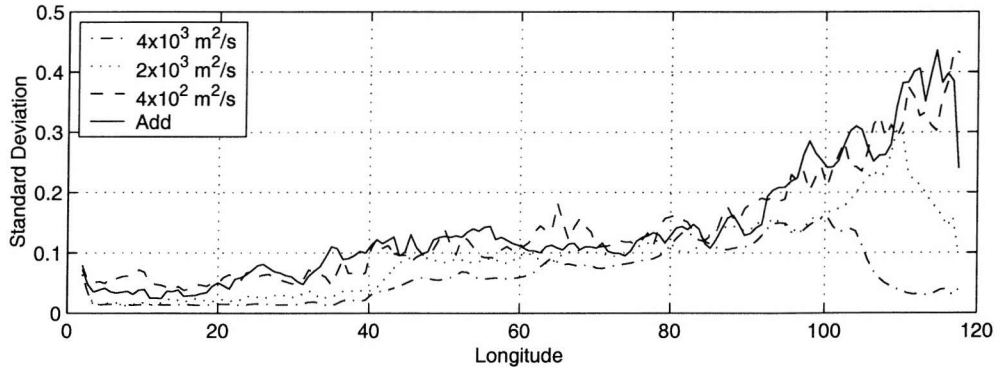

Figure 2.9: Filtered SST variance at 4°N for the fine model grid resolution experiments mixing tracers and momentum along isopycnal surfaces. Dash-dotted line is the experiment using $A_h = 4.0 \times 10^3$ m^{2}s^{-1}, dotted line is $A_h = 2.0 \times 10^3$ m^{2}s^{-1} , dashed line is $A_h = 4.0 \times 10^2$ m^{2}s^{-1} and solid line is the enhanced lateral mixing (Add) experiment, respectively. The units are °C.

In order to provide an objective estimate of the TIW propagation speed we apply a 2-D Radon Transform (RT) to the high-pass data shown in Figure 2.8. See Challenor *et al.* (2001) for a comprehensive description and application of the 2-D Radon Transform to satellite oceanographic data. The RT gives the strength of the signal as a function 'slope' or wave speed. This method is to mathematically define the technique used to measure speed by hand. When the line is perpendicular to the alignment of crests and troughs of

the TIW, the projection will have the maximum variance (i.e. maximum energy). Thus to find their direction of travel in the time-longitude diagram (which is their velocity) the elevation angle of the perpendicular to that region which gives the maximum TIW variance is determined.

The normalised RT power as a function of wave speed is shown in Figure 2.10. The wave speed which has the greatest power is given in Table 2.2 for each experiment. This wave speed is taken as the propagation speed, c_T, of the TIWs. The TIW propagation speed is highest, c_T =29 cm s^{-1}, for the case with the highest value of A_h (4.0×10^3m^{2}s^{-1}). For lower values of A_h, c_T is approximately 24 cm s^{-1} (the differences between these three experiments is probably not significant). However, for the lowest value of A_h (4.0×10^2m^{2}s^{-1}) there is a distinct secondary peak in the wave speed at around 40 cm s^{-1}. The enhanced mixing case also has secondary peak, but less distinct, around the same wave speed and also lower speed values (20 cm/s). These slower moving waves are discernable in the time-longitude plots in the lower panels of Figure 2.8. Similar waves can be seen in the upper panels, but with an amplitude such that they do not show up in the RT analysis.

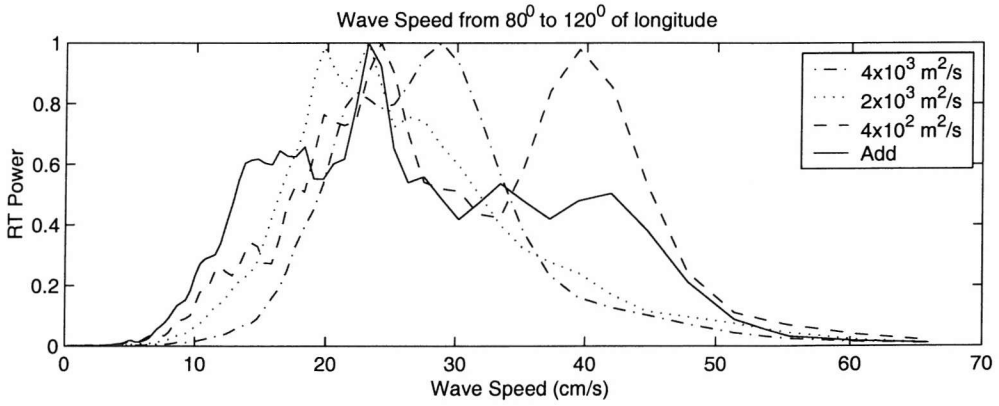

Figure 2.10: Wave speed obtained with Radon Transform calculated from SST at 4°N for the fine model grid resolution experiments mixing tracers and momentum along isopycnal surfaces. Dash-dotted line is the experiment using $A_h = 4.0 \times 10^3$ m^{2}s^{-1}, dotted line is $A_h = 2.0 \times 10^3$ m^{2}s^{-1} , dashed line is $A_h = 4.0 \times 10^2$ m^{2}s^{-1} and solid line is the enhanced lateral mixing (Add) experiment, respectively. The units are cm s^{-1}.

2.7 TIWs response to wind

In previous section we have demonstrated that lateral mixing plays a crucial role on equatorial dynamics simulation. Here we extend our wave variability analysis by means of studying the impacts of wind strength effects on TIW.

The philosophy behind the work presented in this section is to evaluate if the model results extend and support some trends verified on the observations (discussed in the Chapter 3) related to TIW variability as a function of the large scale climatic conditions, including phenomena such as ENSO.

Due to computing time reasons, four experiments are performed using the low spatial resolution model. Three of them only differ on the zonal wind strength forcing. The fourth experiment uses the enhanced equatorial mixing parameterization (shown in Section 2.2). The experiments descriptions are tabulated in Table 2.3.

The control experiment (Itm802) is forced by Hellerman and Rosenstein (1983) zonally averaged monthly mean wind stress (τ_x) over the Pacific ocean basin, seasonally varying. In the second experiment (Itm801) τ_x is decreased by a factor of 0.5 and in the third (Itm803) τ_x is increased by a factor of 1.5. The fourth experiment performed (Itm804) uses the same strengthened wind forcing than Itm803 but with enhanced equatorial mixing parameterization.

The Table 2.3 lists the experimental details and also a number of diagnostics: SST_c averaged over the Cold Tongue region (same region defined in Section 2.2), EUC_{max}, SEC_{max} and $NECC_{max}$ maxima current speed values (cm s^{-1}).

Before investigating the wind forcing effects on TIW characteristic simulations, we briefly analyze the mean state main characteristics of the different experiments when either distinct large scale wind forcing or enhanced lateral mixing parameterization are applied.

The main equatorial current features found in these simulations are similar to those shown in the previous experiments, e.g. Figure 2.1. The simulations reveal a direct relation of the equatorial ocean circulation to the wind forcing strength. However, the EUC exhibits a non-linear behavior as function of the wind stress magnitude applied to the simulations.

Name	A_h	τ_x	SST_c	EUC_{max}	SEC_{max}	$NECC_{max}$
Itm801	2.0×10^3	$\tau_x * 0.5$	25.8	52	-30	3
Itm802	2.0×10^3	$\tau_x * 1.0$	23.4	94	-45	5
Itm803	2.0×10^3	$\tau_x * 1.5$	21.0	103	-50	6
Itm804	$4.0 \times 10^2 + 2.0 \times 10^3$	$\tau_x * 1.5$	21.5	92	-50	13

Table 2.3: Description of the numerical experiments performed using different wind strength and some diagnostics, where the columns represent: Experiment names, mixing coefficients (m^2s^{-1}), Zonal wind forcing strategy, SST averaged over the Cold Tongue region extending from 6°N to 6°S and 90° to 119° of longitude (unit is °C), EUC maximum value, SEC maximum value and NECC maximum value. Speed current units are cm s^{-1}.

The EUC increases its speed from a maximum of 56 cm s^{-1} under reduced winds experiments to over 110 cm s^{-1} when stronger wind forcing is applied in the simulation, see for instance Table 2.3 where the values are displayed. The EUC is deepened also reaching 270 meters depth. The equatorial current system is sensitive to the large scale phenomena such as ENSO, where the EUC has shut down during 1982-83 El Niño episode as shown by Firing *et al.* (1983) and almost completely shut down at 140°W during 1997-98 El Niño episode in Seidel and Giese (1999) simulations. A second feature highlighted from the mean state analysis is that the SEC is made deeper, wider and faster when stronger winds are used. Opposite features of this current are seen in the experiment using weaker wind forcing.

Overall NECC speed is underestimated, this current is weaker and almost completely shut down when the model is forced by reduced wind stresses, as shown in Table 2.3. Although, in the enhanced mixing experiment, NECC is well developed and stronger when compared with previous experiments. This experiment shows similarities of the equatorial current structure with those performed by Brentnall (1999) using a realistic OGCM forcing and configuration. In his equatorial simulations, despite the current magnitudes being smaller than ours, the SEC, EUC and NECC northern branch structure are comparable.

Under normal conditions the strong equatorial easterly winds produce a strong upwelling of cold water in the eastern Pacific that moves westward. Plots of mean SST (not shown here) show that the upwelling on the eastern tropical Pacific and the extent of the cold tongue are largely affected by the mean wind condition, used in each specific experiment. Under the weaker wind conditions the Cold Tongue, taken to be delimited by the 25°C isotherm, does extend to around 75° while when under stronger winds it extends 35°,

further west. These features are also represented on the Table 2.3 where the Cold Tongue area averaged temperature varies by 5°C when comparing the experiments forced by weaker and stronger winds. The Cold Tongue occurs at 2° width either side of the equator, with weaker winds, against 5° approximately when the winds are double the strength at 100° of longitude.

The depth-latitude section at 97° of longitude (not shown) suggests that both $\overline{K}_m$ and K_e maxima tend to increase as the equatorial currents are accelerated by the wind forcing strengthening (see methodology in Section 2.5). The K_e is split in two branches either side of equator coincident with the SEC north and southern branches, near the EUC shear regions.

Overall, there is a significant increase in the eddy kinetic energy of the two bands either side of the equator when the experiment is forced by stronger winds. It is worth noting that the experiment using enhanced equatorial mixing has its K_e energy levels enlarged when compared with itm803, on either sides of equator. The increasing eddy kinetic energy might be related to the current shear increase. These two regions of deep eddy activity are coincident with the TIW activity region as mentioned previously on Section 2.5.

Based on their instability analysis Luther and Johnson (1990) have found a peak of eddy potential energy production in the thermocline below NECC, suggesting these instabilities are confined to a small latitude-depth range to the production region. In our simulation a secondary peak of K_e close to the surface and towards 5°N occurs in Itm804. That is where SEC northern branch and NECC shear region are simulated in this experiment.

2.7.1 TIW activity

In this section the wave variability and some of their spectral characteristics are analyzed. TIW are visible in the raw SST field (Figure 2.11) but as done before the SST time series located at 4°N are filtered and retained only the high variability component. The 2-D FIR digital filter is set with the same parameters as in Section 2.6.

The plots comparison, in Figure 2.11, reveals significant differences in the TIWs characteristics simulated by each experiment. Overall, the waves are more active and faster

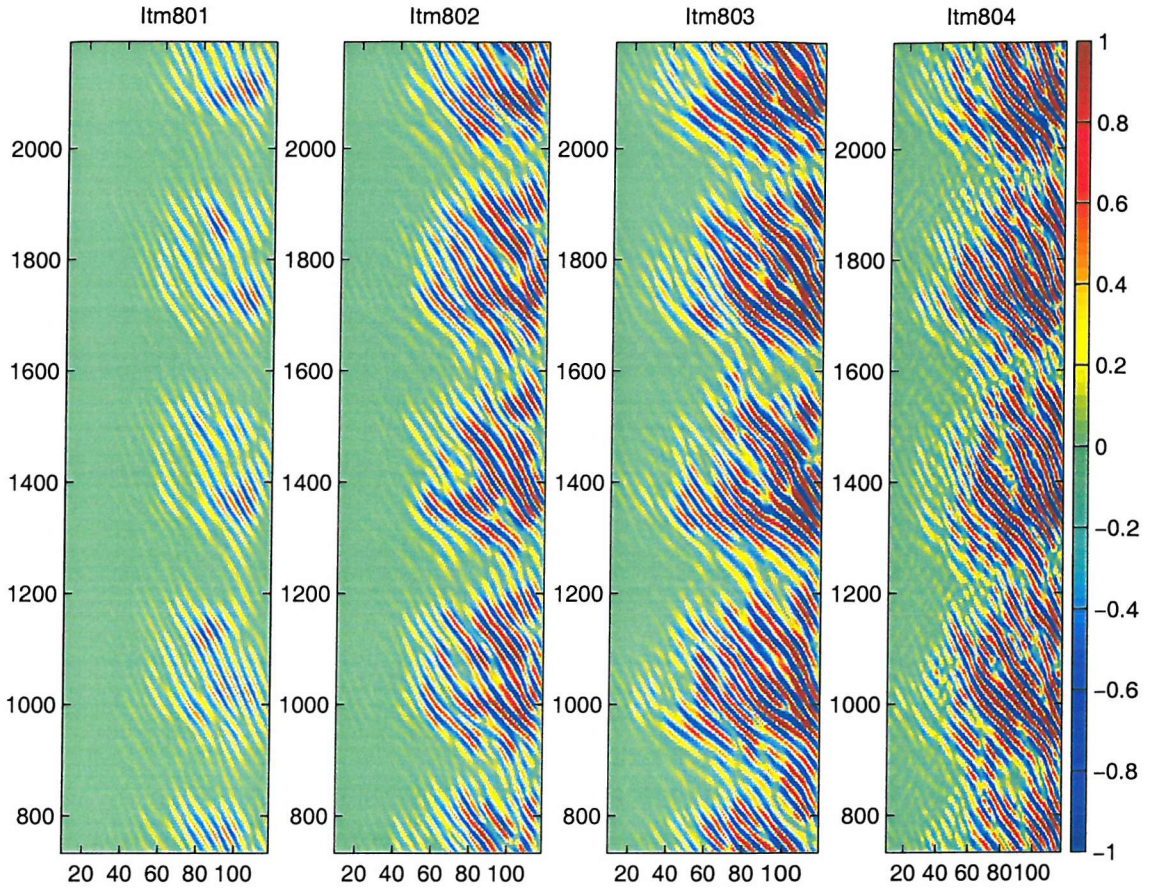

Figure 2.11: Filtered SST, displaying TIWs, at 4°N as a function of time (y-direction) and longitude (x-direction), for the fine model grid resolution experiments using different τ strength. Units are °C.

when the wind forcing is increased. It is worth noting that TIWs are an oceanic phenomena and their generation sources are caused by the equatorial current shear and meridional temperature gradient.

Thus, as the wind used on this experiments are modifying the mean state and consequently the energetics characteristics, the result of it is revealed in the TIWs behavior and characteristics. For instance, the TIWs exhibit low variability when weaker wind is used, as low as 0.05°C, shown in the Figures 2.11 and 2.12. This simulation also exhibit the slower waves propagation speed. The dominant phase speed (c_T) is approximately 37 cm s^{-1}, calculated from the longitude-time plots showed in Figure 2.11.

Both TIW variability and phase speed are increased when the wind forcing is strength-

Name	STD	c_T	λ	Γ
Itm801	0.04	37	7.4	50.3
Itm802	0.4	55	7.4	33.2
Itm803	1.4	59	12.3	34.8
Itm804	1.0	61	12.3	33.2

Table 2.4: Table displaying the dominant TIW spectral characteristics at 4°N. STD is the maximum standard deviation (°C), c_T (in cm s^{-1}) is calculated by applying Radon Transform (RT) on the TMI Hovmöller diagrams (Figure 2.11). λ is in degrees and Γ is in days.

ened, with values reaching 0.4°C and 55 cm s^{-1}, in experiment Itm802, and 1.4°C and 59 cm s^{-1} in experiment Itm803, as shown in Table 2.4 and Figure 2.12. The maximum TIW activity is slightly decreased when equatorial mixing is enhanced (Itm804) compared with the experiment using stronger winds (Itm803). However, this experiment exhibits larger TIW variability in the inner domain, westward of the peak region extending from 85° to 105° of longitude. This larger wave activity in the inner domain produced by the enhanced mixing might be playing a role in limiting the strength of the EUC and raising the Cold Tongue SST.

It will be done an analogy between the results produced here and by analyzing the TIWs interannual variability as function of the large scale climatic conditions and interannual variability such as ENSO phenomena in Chapter 3.

2.8 Summary and Conclusions

The model equatorial current system is found to be very sensitive to the level and form of lateral mixing. Both the mean currents and wave activity become more energetic as the magnitude of the lateral mixing coefficient is decreased. Here we find that decreasing the magnitude of the lateral mixing coefficient by one order of magnitude increases the strength of the EUC by 100% with the EUC being narrower with lower values of diffusivity. There is an associated order of magnitude increase in the level of eddy kinetic energy.

As others have found, if the lateral mixing is orientated along isopycnic surfaces then there is, in general, a speeding up of the current system and a better defined NECC.

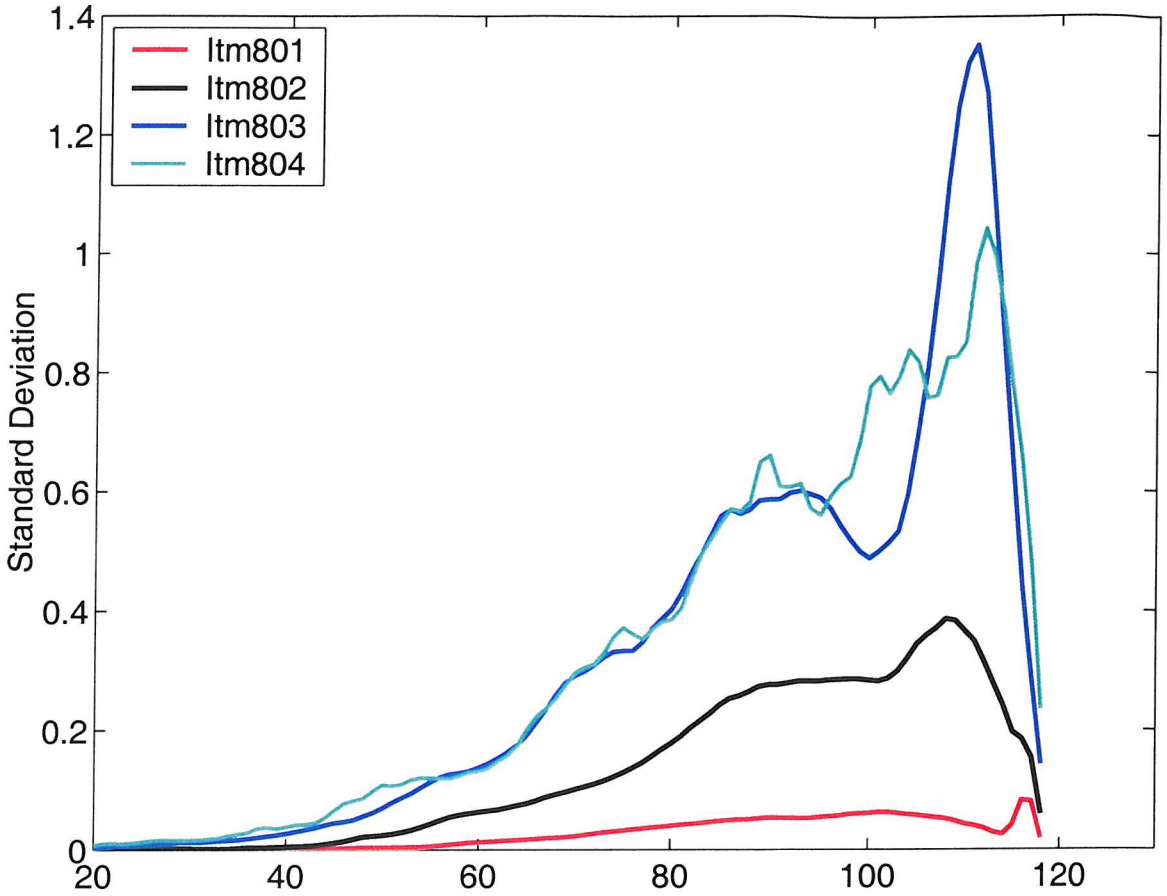

Figure 2.12: SST standard deviation at 4°N for the fine model grid resolution experiments.

However these differences are dependent on the grid and level of mixing. With the lowest value of the lateral mixing coefficient we consider, the results in terms of the strength of the EUC and the SST in the cold tongue region, are less dependent on either the formulism of lateral mixing or the grid spacing (see Table 1 and Figure 2). This points to some sort of numerical convergence and independence of the way sub–grid scale (non–resolved) processes are treated with modest grid resolution. However it should be noted that there is a 30% increase in the EKE going from horizontal to isopycnic mixing (Table 1) with the lowest value of the lateral mixing coefficient we consider.

A major conclusion from the results using a conventional constant value for the lateral mixing coefficient is that, regardless of the level of mixing or its orientation, the model equatorial ocean cannot be made comparable to observations (with the caveat that we are

considering an idealized geometry and forcing). Decreasing the mixing increases the cold tongue SST but produces unrealistically strong currents. Our solution to this dilemma is to invoke enhanced mixing close to the equator, which limits the strength of the EUC whilst little affecting the TIW activity and hence the cold tongue SST (see Figure 2). The physical rationale we put forward for this enhanced mixing is the effect of the observed interleaving of water masses in producing a meridional flux of tracers and momentum (Richards and Banks, 2002, Richards and Edwards, 2003).

We find that both the barotropic and baroclinic energy conversion terms are important for the production of TIWs. The relative role of each and timing of these conversion terms changes as the level of imposed mixing changes. At low levels of lateral mixing, barotropic instability is found to dominate the production of total eddy energy. Including enhanced mixing at the equator reduces this barotropic production, but surprisingly increases the baroclinic production away from the equator.

Experiments using horizontal mixing for tracers and momentum tend to damp out the TIW activity (not shown) when compared with isopycnal mixing. Additionally, the waves are more intense and confined to the eastern part of the domain when both tracers and momentum are mixed along isopycnic surfaces.

As the mixing coefficient is decreased the TIWs become more energetic and their behavior more chaotic, with reduced seasonality. A large diffusivity tends to damp the wave activity producing more organized propagation patterns as well as confining the waves to the eastern portion of the domain (Figure 2.8). The changes to the calculated phase speed of the waves (around 24-29 cm/s) with changes to the lateral mixing are probably not significant. However, it is noteworthy, that as the mixing coefficient is reduced a second set of waves with a faster phase speed (around 40 cm/s) becomes more discernable.

Overall, kinetic energy levels tend to increase as a consequence of the wind forcing strengthening. That is the probable reason why TIW have larger activity during La Niña years as shown in the literature and further discussed in Chapter 3. Wavelength does not shown a linear relationship with the wind strength but it tends to be increased as the wind increases. TIWs activities and wave propagation speed are increased as the wind is strengthened, as shown by our experiments.

The sensitivity of the flow in the equatorial ocean to lateral mixing we have here means that the form and action of that mixing needs a careful examination. It is not the case that simply increasing a model's resolution will lead to better results if the physics of the model itself are deficient. Here we have identified interleaving as having a significant effect on both the mean properties of the ocean and the TIW activity. It is unlikely, in the near future, that OGCM used in climate studies will have the required vertical resolution (order 1m) in order to properly resolve the interleaving. We therefore have to resort to parameterizing its effect. Here we have used a relatively crude parameterization and more investigation relatively responsible mixing process need to be done.

Chapter 3

TIWs and their interannual variability

3.1 Introduction

The central and eastern Pacific, within the tropical region, are dominated by a distinct annual cycle that is driven by the seasonal variation in solar radiation due to the earth-sun distance and the semi-annual cycle in solar declination, when the sun is directly overhead twice per year (Mitchell and Wallace, 1992). There is a warm season around March and April when the Cold Tongue is confined to the upwelling region near the South American coast. This cold tongue is most pronounced from August to October at the peak of cold season when it can extend as far as 130°W. During this period the maximum SST is observed to be meridionally asymmetric and the farthest northward of the Southern Hemisphere easterly trade winds. The mean currents in the equatorial region also exhibit seasonal variations. The SEC (Halpern *et al.*, 1988, Qiao and Weisberg, 1995) is strongest during the northern hemispheric summer and weakened in the spring when the meridional gradients are small and when the southeast trades are relatively weak (Philander *et al.*, 1987).

TIWs occur during the cold season as mesoscale perturbations of currents and temperature in the upper equatorial ocean and play a significant role in the mean balances of momentum, heat and energy as shown previously in Chapter 2. TIWs can be seen as cusp shaped distortions of SST fronts as first showed by Legeckis (1977) and recently by many others studies, such as Flament *et al.* (1996), Chelton *et al.* (2000), Liu *et al.* (2000),

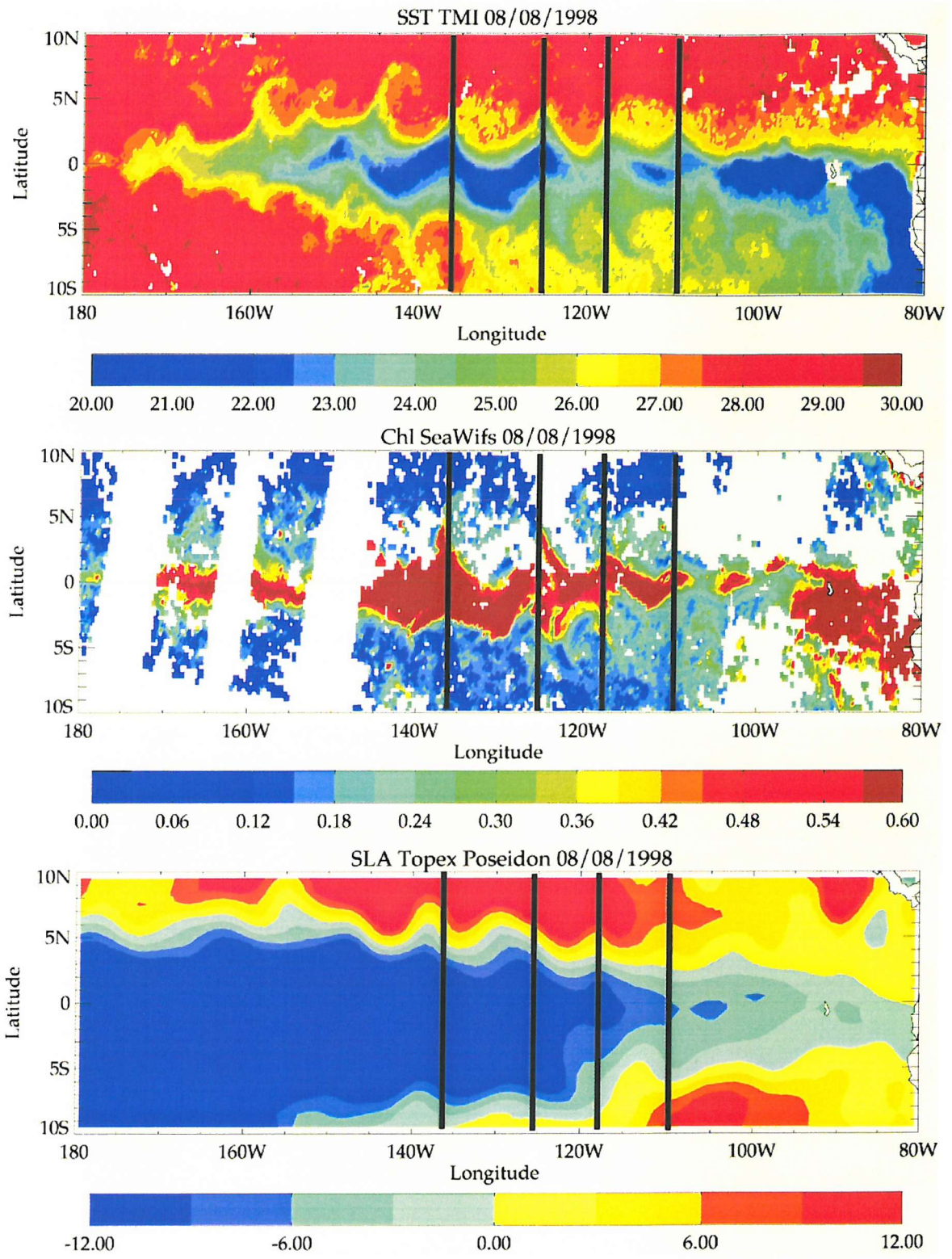

Figure 3.1: Figure displaying TIW imprints in various fields. SST derived from TMI satellite on 8 October 1998, top panel. Middle panel same but for Chlorophyll derived from Seawifs and bottom panel are sea-level anomalies (SLA) derived from TOPEX/POSEIDON. (Courtesy of Dr. Jérôme Vialard)

Menkes *et al.* (2002), Thum *et al.* (2002).

These waves have clear imprints in other variables, as shown in the Figure 3.1, such as Sea Surface High (SSH) (Polito *et al.*, 2000, 2001) and Chlorophyll (Strutton *et al.*, 2001). The instability season typically extends from the boreal summer to the beginning of the winter in the Pacific ocean (Baturin and Niiler, 1997). Figure 3.1 shows that the equatorial cold tongue is separated by crests and troughs from the NECC warmer waters by sharp fronts. The SST gradient in this front can be as abrupt as approximately 2°C/Km as suggested by Kennan and Flament (2000) and Menkes *et al.* (2002). The energy source for the generation of TIWs invoke the shear between EUC-SEC and SEC-NECC as shown in the Chapter 2 and Masina *et al.* (1999).

Some studies have shown TIW north of the equator associated with anticyclonic eddies of three dimensional structures. Hansen and Paul (1984) have mentioned these features and Flament *et al.* (1996) have sampled them using drifters, both studies in the Pacific ocean. Recently, Menkes *et al.* (2002), have shown the effects of an Atlantic ocean tropical vortex in the tracer circulation fields such as temperature, salinity and biological nutrients. Cold equatorial waters, which are nutrient and biologically rich are equatorially upwelled, advected north and downward forming sharp fronts across the frontal boundary. The mixing caused by these waves also redistribute nutrients and dissolved gases, thus affecting the biological productivity in the equatorial regions.

Allen *et al.* (1995), Lawrence *et al.* (1998) and Benestad *et al.* (2001) have shown that systematic TIW phase shifting is linked with events in the wind. For instance, Allen *et al.* (1995) have performed numerical experiments by forcing a model without the intraseasonal component in the windstress. They found that the TIW lost all phase correspondence compared with a control experiment, where the ocean is forced by observed daily windstress. Lawrence *et al.* (1998) have suggested that Rossby waves, remotely wind forced, can influence TIW characteristics such as phase and phase speed. Both Lawrence *et al.* (1998) and Benestad *et al.* (2001) also suggest that TIW may be modified by remote sub-seasonal forcing in the Pacific west through Kelvin waves, excited by Westerly Wind Bursts (WWB).

The TIW exhibit a marked interannual variability. They are more active during La Niña years when the equatorial trades and cold tongue are stronger and the meridional

gradients sharper. On the other hand, these waves are less active during El Niño years when the SST gradient is reduced by the weakened cold tongue. Although this point has been addressed by other authors e.g. Baturin and Niiler (1997) and Contreras (2002), there is still ample scope to further explore TIW variability using both observational and modelling approaches.

In this chapter the TIW interannual variability, their relation and dependence on other large scale climatic phenomenon such as ENSO is presented. A high resolution temporal series of satellite data from 1998 up to 2002 is analyzed. These data have higher spatia-time resolution compared with the data used by Contreras (2002). The aim is to further extend the period of previous studies which have used these satellite data since some of them have focused only on the 1999 TIW season, e.g. Chelton *et al.* (2000), Liu *et al.* (2000), Hashizume *et al.* (2001), Thum *et al.* (2002). In order to complement the TIW variability analysis we compare some observational results with OGCM simulations which have used different wind stress strengthening and lateral mixing parameterizations (see Section 2.7.1).

This chapter is organized as follow. Section 3.2 describes the radiometer, scatterometer and altimeter satellite sensors and data from which SST, wind and sea level heights time series are derived. Section 3.3 briefly describes the Pacific oceanic and atmospheric climatic conditions during the period of our analysis. Section 3.4 analyzes the variability found in the satellite data and TIW spectral characteristics. In Section 3.5 we discuss the results and summarize the main findings.

3.2 Satellite data

3.2.1 TMI SST data

The Tropical Rainfall Measuring Mission (TRMM) satellite has been operational since 28 November 1997 with its orbit ranging between 35° north and 35° south of equator, allowing TRMM to fly over a given position on the Earth's surface at a different local time each day. The TRMM orbit is circular with an altitude of 350 km and an inclination of 35° to the equator. The orbit period is approximately 96 minutes.

The satellite carries the TRMM Microwave Imager (TMI) which is a multi-frequency microwave radiometer. TMI operates in five frequency channels which are: 10.65, 19.35, 21.235, 37.0 and 85 GHz. The horizontal resolution ranges from 5 km (at 85 GHz) to 45 Km (at 10.65 GHz). Microwave radiation is emitted by the Earth's surface and by water droplets within clouds. However, when layers of large ice particles are present in upper cloud regions (characteristics of heavy rainfall systems) microwave radiation tends to be scattered. The five frequencies of the TMI are chosen to discriminate among these process, thus revealing the likelihood of rainfall.

The products derived includes sea surface temperature, surface wind speeds derived using two different radiometer channels, atmospheric water vapor, liquid cloud water and precipitation rates. TRMM is a joint program between the North America Space Agency (NASA) and the National Space Development Agency of Japan (NASDA). The TMI radiometer counts are converted to temperature using a linear relationship, as described in Nirala and Cracknell (2002).

The SST[1] data are provided as daily maps (separated into ascending and descending orbit segments), 3 day mean maps, weekly mean maps and monthly mean maps. The data are available from December 1997 to the present. All images cover a global region extending from 35°S to 35°N at a 'high' pixel resolution of 1/4° (25 km). In this chapter three day average data are analyzed starting on 1 January 1998 and finishing 31 December 2002.

3.2.2 QuikScat wind data

The wind data used in this analysis are derived from the microwave scatterometer QuikScat, which was launched on the QuikBird satellite in June 1999. The primary mission of QuikScat[2] is to measure winds near the sea-surface. QuikScat is the third in a series of NASA scatterometers that operate at Ku-band (i.e., a frequency near 14 GHz). QuikScat is essentially a radar device that transmits electromagnetic pulses down to the Earth's surface and then measures the power that is scattered back to the instrument. This backscattered

[1]Data and information can be downloaded from Remote Sensing Systems (RSS) at http://www.remss.com/tmi

[2]More information can be downloaded from Jet Propulsion Laboratory (JPL/NASA) at http://winds.jpl.nasa.gov/missions/quikscat/quikindex.html

power is a measure of surface roughness.

For water surfaces, the surface roughness is highly correlated with the near-surface wind speed and direction. Hence, wind speed and direction at a height of 10 meters over the ocean surface are retrieved from measurements of the QuikScat backscattered power. The instrument provides wind measurements with 25 km resolution over a single 1600 km swath that is then smoothed and interpolated in order to obtain 3-day averages on a 1/2° grid resolution. The data spans the period from the beginning of July 1999 to the end of November 2002.

3.2.3 Topex/Poseidon SSH data

Radar altimeter on board the satellite permanently transmit signals at high frequency (over 1700 pulses per second) to Earth, and receive the echo from the sea surface. This is analyzed to derive a precise measurement of the round-trip time between the satellite and the sea surface. The time measurement, scaled by the speed of light (at which electromagnetic waves travel), yields a range measurement. By averaging the estimates over a second, this produces a very accurate measurement of the satellite-to-ocean range. However, as electromagnetic waves travel through the atmosphere, they can be decelerated by atmospheric water vapor or by atmosphere ionization. The ultimate aim is to measure sea level relative to a terrestrial reference frame. This requires independent measurements of the satellite orbital trajectory, i.e. exact latitude, longitude and altitude coordinates.

The Topex/Poseidon (T/P) satellite, flies at an altitude of 1330 km, on an orbit inclined at 66° to the Earth's polar axis; this is why it can cover only up to 66° North and South. The satellite passes over the same ground position approximately every ten days, uniformly sampling the Earth's surface. The sea surface height (SSH) is one of the T/P derived data and it is the range at a given instant from the sea surface to a reference ellipsoid. Since the sea depth is not known accurately everywhere, this reference provides accurate, homogeneous measurements. The sea level is simply the difference between the satellite height and the altimetric range.

The along-track T/P data used here are the same used in Cipollini *et al.* (1997), Challenor *et al.* (2001) and recently by Killworth *et al.* (2003), where a detailed description

can be found. The original T/P data were obtained from Geophysical Data Records from AVISO. A set of standard corrections for orbit errors, atmospheric delays, tides and sea state effects has been applied by Cipollini *et al.* (1997). The SSH anomalies are computed relative to the 1993-1995 mean high profile in each location along the tracks and interpolated to a regular 1° latitude x 1° longitude x 1 cycle grid. As shown in Cipollini *et al.* (1997) the re-mapping reduces the instrument and correction errors but preserving the large scale signal in the data.

In this study T/P information is compared with TMI data. In order to have both data sets on the same time and grid resolutions, T/P is spatially re-binned into 1/4° grid and temporally from 1 cycle mean (9.92 days) to 3–days mean. T/P data spans the period from the beginning of January 1998 to the end of May 2002. This corresponds to 193 full 10–day repeat cycles, from cycle 195 to 357, 4 years and 5 months.

3.3 Climate diagnostics

The climate in the tropical Pacific region since from the end of 90's decade to 2002 has been characterized by a sequence of ENSO episodes and they are briefly described by analyzing some diagnostic climatic indexes [3].

The normalized Southern Oscillation Index (SOI) is calculated based on the difference of the normalized Sea Level Pressure (SLP) measured at Tahiti and Darwin, i.e. $SOI = SLP_{Tahiti} - SLP_{Darwin}$. In general, the SOI time series correspond very well with changes in ocean temperatures across the eastern tropical Pacific. The negative phase of the SOI represents below-normal air pressure at Tahiti and above-normal air pressure at Darwin. Prolonged periods of negative SOI values coincide with abnormally warm ocean waters across the eastern tropical Pacific typical of El Niño episodes. Conversely, positive SOI values coincide with abnormally cold ocean waters across the eastern tropical Pacific typical of La Niña episodes. The SST anomaly indexes are averaged over the areas specified in Figure 3.2. The base period used to calculate the monthly Niño region anomalies is 1971-2000.

[3]Both index values and a comprehensive description of them can be found at Climate Prediction Center (CPC/NCEP/NOAA) website, http://www.cpc.ncep.noaa.gov/data/indices/index.html

Table 3.1 shows a zonal wind magnitude index at surface averaged over the west (140°E-180°W), central (175°W-140°W) and east (135°W-120°W) Pacific ocean along the Equator. The index is calculated based on the area averaged data from QuikScat time series. The period spans from 1999 to 2002. During La Niña years, e.g 1999 and 2000, the zonal wind component is stronger in the west and central Pacific. Conversely, during El Niño year (2002) the trade winds are relaxed as shown in Table 3.1.

Year	140°E-180°W	175°W-140°W	135°W-120°W	$ENSO_{phase}$
1999	-3.84	-7.01	-5.31	La Niña
2000	-3.54	-6.38	-5.33	La Niña
2001	-1.70	-6.09	-5.81	Neutral
2002	0.27	-5.30	-5.45	El Niño

Table 3.1: Table displaying the a zonal wind magnitude index at surface, averaged over the west (140°E-180°W), central (175°W-140°W) and east (135°W-120°W) Pacific ocean along the Equator. Units are in ms^{-1}.

The strongest ENSO of the last century was in 1997-1998 when an El Niño episode occurred as shown by the normalized Southern Oscillation Index (SOI) and the SST in Figure 3.2. From the middle of 1998 up to the end of 2001, the situation reversed and in 1999 a well defined La Niña episode was configured in the tropical Pacific. During this period colder waters than normal were over the equatorial eastern and central Pacific. The subsequent years, 2000 and 2001, the trade winds have weakened (Table 3.1) and a situation varying from slight cooling to normal (see SST at Niño3.4 in Figure 3.2) of the equatorial waters was established in the Pacific. During the year 2002 this situation reversed and an El Niño was established again in the equatorial region though somewhat weaker than the 1997-1998 episode.

3.4 TIWs variability from observed data

3.4.1 SST variability

Figure 3.3 shows the longitude-time plot of SST at different latitudes, ranging from the Equator to 4°N. Westward-propagating waves are apparent in the plots even without filtering. Note that the white strip on the equatorial plot is the Galápagos island. This figure

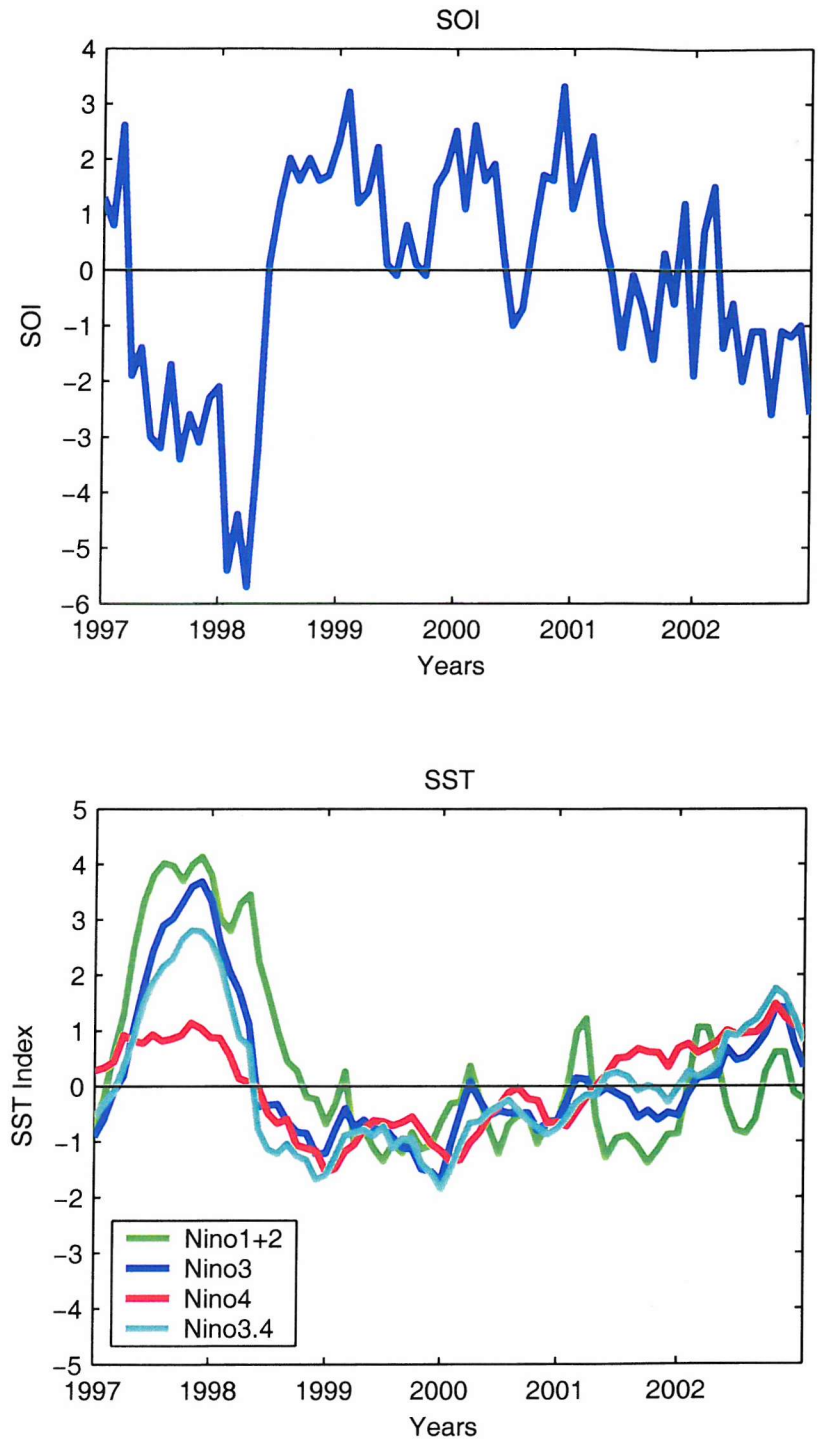

Figure 3.2: Upper panel is the normalized Southern Oscillation Index (SOI) (Tahiti - Darwin) Sea Level Pressure. Lower panel are the SST anomalies averaged over the following areas: Niño 1+2 (0-10°S)(90°W-80°W), Niño 3 (5°N-5°S)(150°W-90°W), Niño 4 (5°N-5°S) (160°E-150°W) and Niño3.4 (5°N-5°S)(170-120°W). Base period used to calculate the monthly Niño region anomalies is 1971-2000. SST index values are °C

clearly shows the seasonal cold tongue cycle most evident in the equatorial plot, with its coldest period being always in the second half of the year. Although weaker at this latitude, TIWs are still visible. Figure 3.3 shows the climatic characteristics previously described and shows TIW activity stronger during the La Niña years, with the season 1998-99 being the strongest TIW season. Also, the SST plots are showing that TIWs are more active at 1°N.

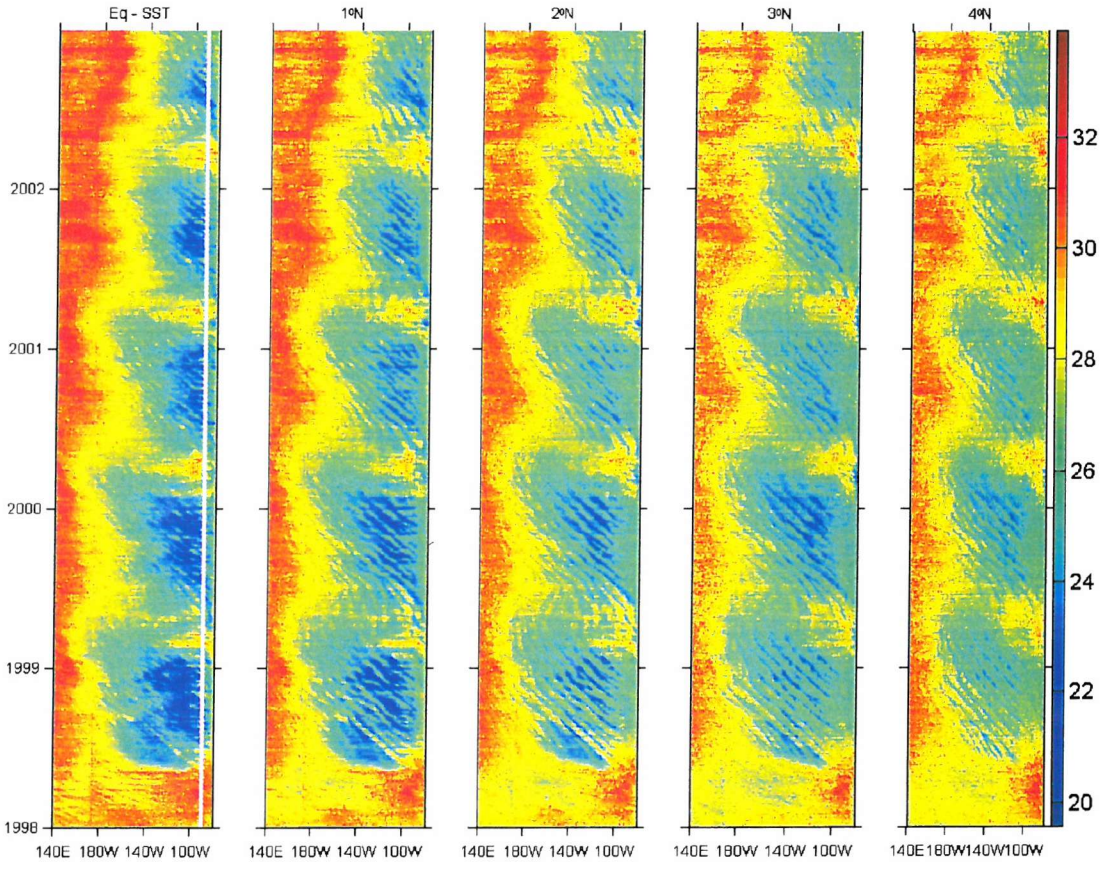

Figure 3.3: Longitude time plot of SST derived from TMI. Row data.

The wave signal can be highlighted to some extent with a different choice of color scale, but it is clear that filtering is more appropriate in order to properly isolate the waves from the variability due to other phenomena such as the seasonal cycle. In order to filter the data, the gaps in the longitude-time series are filled in by using the following approach. A successive, whenever necessary, 3x3 moving window mean is applied to the time-longitude data. It is generated a new longitude-time data without any gap which is used to fill the gaps in the original field. In most of the cases 3 interactions were enough to fill in all the gaps.

The Hovmöller diagrams are then filtered applying a westward-only 2-D finite impulse response (FIR) filter, see Cipollini *et al.* (2001) for more details about this filter. The filter is designed using prior knowledge of the approximate range of the period and wavelength of the waves. This information is set as input and restricts the filter output to a particular region of the frequency-wavelength spectrum. It has a 1/4 length size sample kernel, considering the number of points in time and longitude, passing 5° to 20° in the longitude and 10 to 60 days in time. The filter is the same as that used in the Chapters 2 and 4 only differing here that it is westward-only, i.e. the pass-band is situated only in the westward quadrants in wavelength-frequency space. The filter effectively removes any signal propagating to the east and the seasonal cycle.

Figure 3.4 shows the SST time-longitude filtered fields based on Figure 3.3 data. The results suggest that TIW have their largest variability at 1°N and 2°N, decreasing away from this region. Northward, at 3°N and 4°N, TIWs are still visible from these plots but less intense. At the equator the waves are also visible, however, with larger intensity westward of the Galápagos islands. According to Brentnall (1999), from his numerical simulations performed with and without the Galápagos, the larger intensity westward of the Galápagos islands is caused by the SEC splitting into a pair of barotropically unstable zonal jets originating at the northern and southern border when encountering the island.

In order to quantify and compare the TIWs variability in space and time the statistical standard deviation based on the entire period available and extending from 180°W to 80°W is calculated. The top panel on the left hand side of Figure 3.5, shows the standard deviation performed for each latitude considering the entire period (1998-2002). This plot confirms that the maximum SST variability occurred at 1°N, extending longitudinally from 150°W to 90°W.

The remaining plots in Figure 3.5 display the TIW interannual variability at different latitudes and years [4]. The largest variability of the TIWs occurred during the years when abnormally cold ocean waters were across the eastern tropical Pacific, typical of La Niña episodes such as in 1998 and 1999.

The TIW wave speed characteristics also exhibit a interannual variability as shown in

[4]Note for a given year the wave season extends into the beginning of the next year.

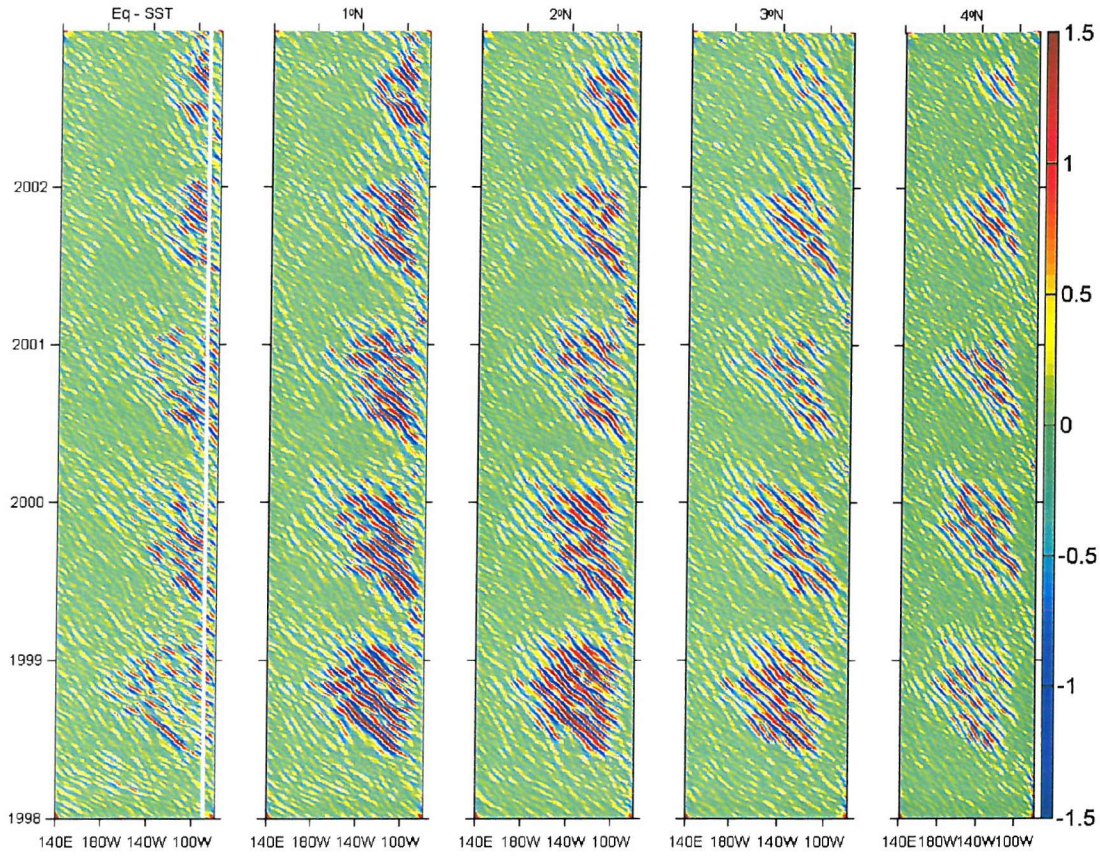

Figure 3.4: Longitude time plot of SST derived from TMI. Filtered data.

Table 3.2. TIW propagation speed (c_T) calculation by applying a Radon Transform (see Section 2.6) for each year as a function of the latitude. Surprisingly the c_T are higher during the 2001 season when the neutral condition were prevailing over the tropical Pacific basin, c_T =61 cm s^{-1}. However comparing the La Niña years, 1998 and 1999 episodes (Figure 3.2), with the beginning of 2002 El Niño episode there is a evidence that besides a strong reduction in TIW activity there is also a reduction in TIW propagation speeds, where they are reduced by 10 cm s^{-1} approximately along of all latitudes between 1°N and 4°N.

Additionally, a spectral analysis is done by means of calculating the dominant wavelength (λ) and period (Γ) of TIWs, based on the filtered SST time-longitude data. These quantities are computed considering the whole period of available TMI SST data and shows that λ is 12° and Γ is 34 days, approximately, at 1°N and 2°N, decreasing at other latitudes.

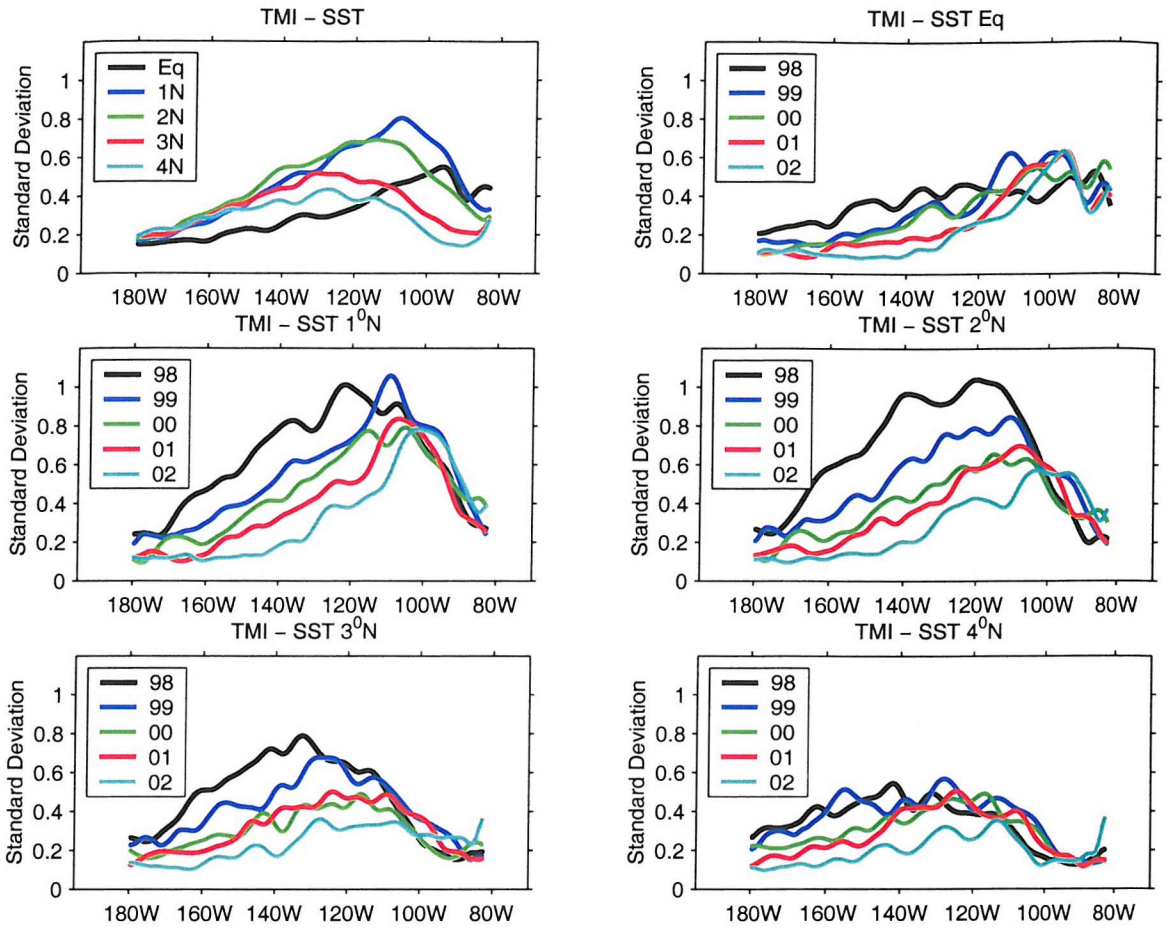

Figure 3.5: Longitude STD plot of SST derived from TMI.

The values found for (λ) and (Γ) are similar to the TIW spectral characteristics reported in the literature e.g Philander (1978), Wilson and Leetma (1988), Baturin and Niiler (1997) and Lawrence *et al.* (1998).

These spectral characteristics exhibit an interannual variability as shown in Table 3.2. During the years of 1998 and 1999 the TIW have the larger values of λ and Γ at 1 and 2°N, which are the latitudes where these waves have their largest amplitudes (Figure 3.5). The average λ for La Niña years is greater than in the El Niño year of 2002 suggesting that in years of stronger upwelling we observe larger wavelengths. This result is analogous with previous findings in 2.7.1 in a sense that longer wavelengths are found when strengthened wind stress is used to force the numerical experiments.

Year	c_T	λ	Γ	$ENSO_{phase}$
1998	55	11.7	33	La Niña
1999	55	11.7	30	La Niña
2000	50	8.2	33	La Niña
2001	61	9.3	21	Neutral
2002	46	10.0	33	El Niño

Table 3.2: Table displaying TIW spectral characteristics at 1°N, where the waves present their maximum variability. c_T (in cm s^{-1}) is calculated by applying Radon Transform (RT) on the TMI Hovmöller diagrams (Figure 3.4). λ is in degrees and Γ is in days.

3.4.2 Wind variability

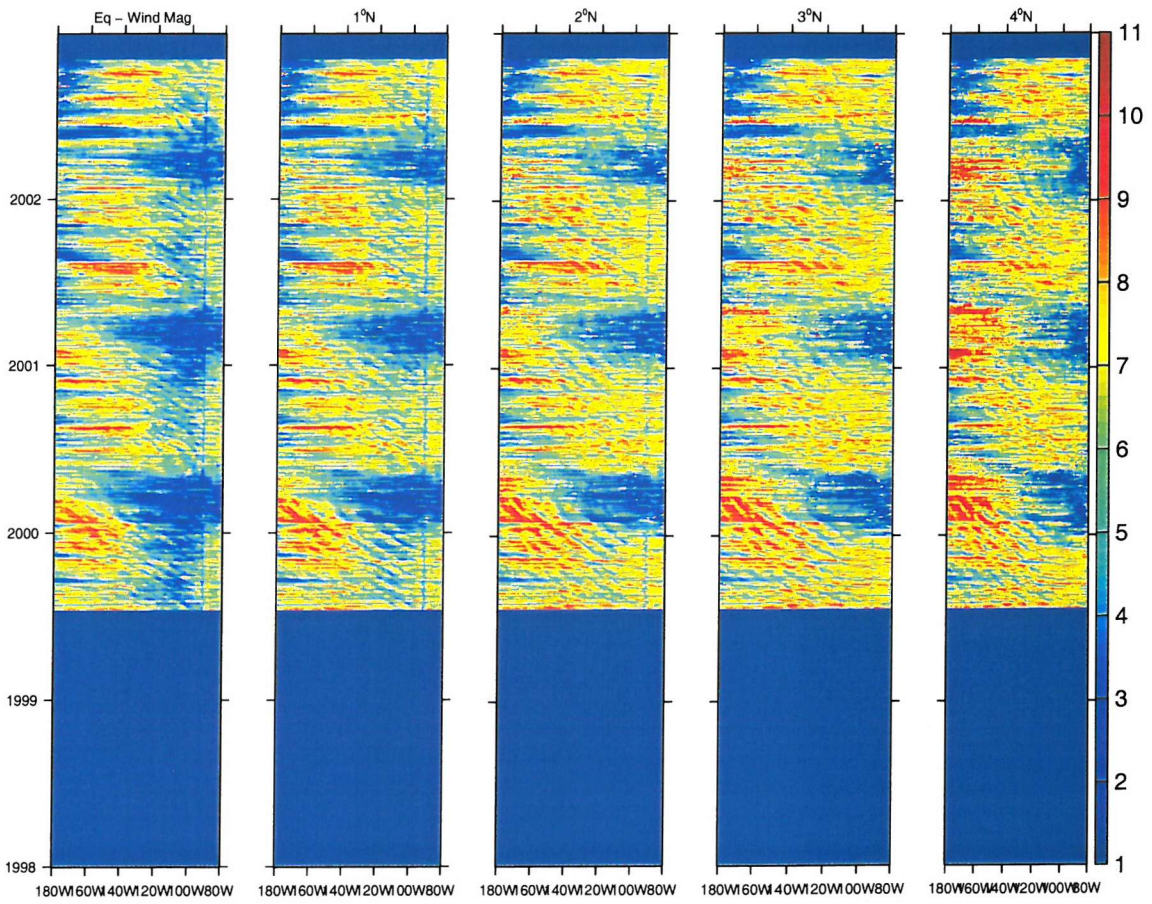

Figure 3.6: Time-longitude plot of Wind magnitude derived from QuikScat.

As previously mentioned the TIW have an atmospheric imprint with the signal propagating into the ABL. Using a conjunction of the surface wind measurements derived from

QuikScat, TMI SST, in situ data and atmospheric radiosonde profile have allowed some observational studies such as Chelton *et al.* (2000), Liu *et al.* (2000), Hashizume *et al.* (2002), Thum *et al.* (2002) explore and investigate the TIW air-sea coupling mechanisms. Liu *et al.* (2000), Hashizume *et al.* (2001) have suggested that SST is in phase with meridional wind component but roughly out of phase (180°) with zonal wind component. Because the scatterometer infers winds from the roughness of the ocean surface, and the roughness is dictated by the difference between the wind and the surface current, scatterometer wind have the surface currents implicit in it (Kelly *et al.*, 2001). Polito *et al.* (2001) has suggested that the oceanic currents have a large impact on surface wind stresses measured by the scatterometer. They suggest that TIWs currents in this low-wind region introduce a significant bias in scatterometer vector wind measurement.

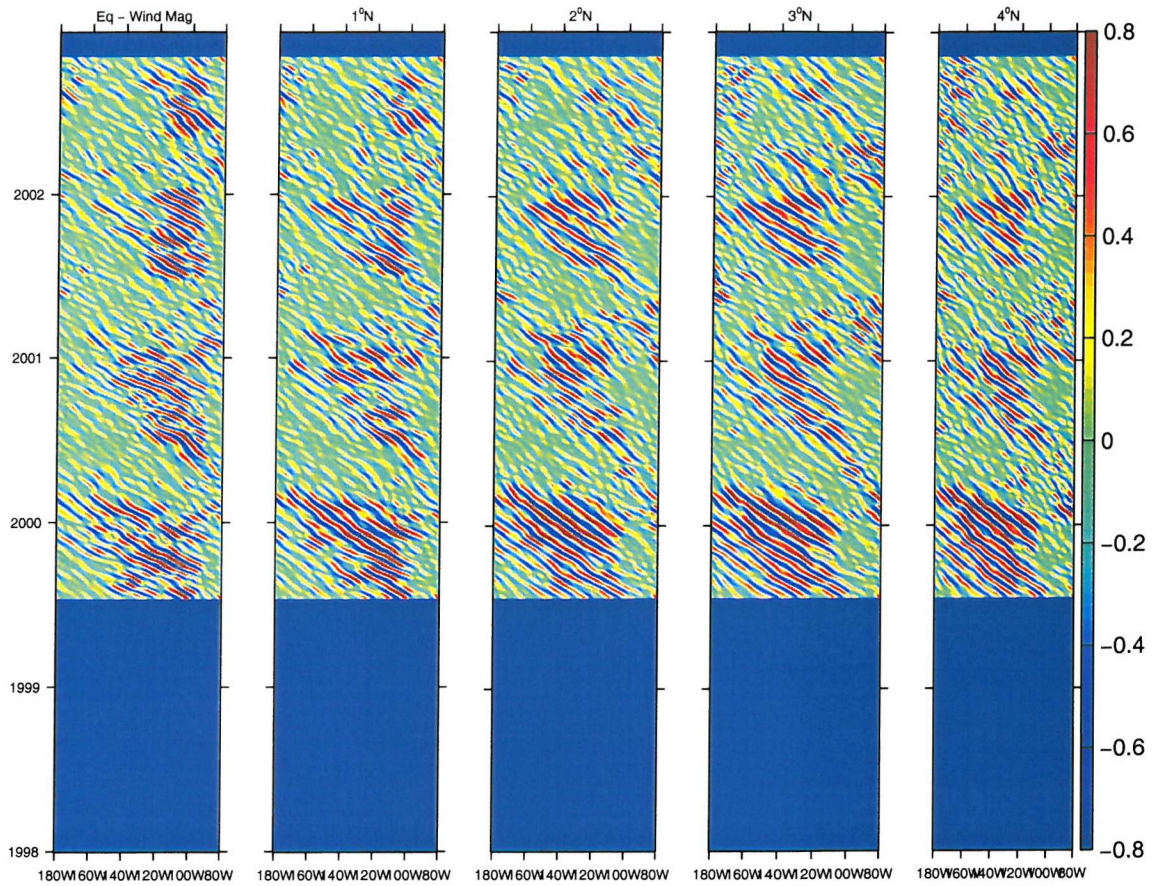

Figure 3.7: Time-longitude plot of Wind magnitude derived from QuikScat.

Regardless of this fact raised by Polito *et al.* (2001), the TIW signals can be clearly seen from the QuikScat wind magnitude analyzed here. The purpose here is further extend

the annual and interannual analysis on the TIW atmospheric response to them and their behavior during the different phases of ENSO.

Figure 3.6 shows the wind magnitude as a function of time-longitude. As shown in SST plots, the TIW also have a westward propagating signal and the wave signals are enhanced by filtering out the lower frequency component of the wind magnitude field as shown in Figure 3.7.

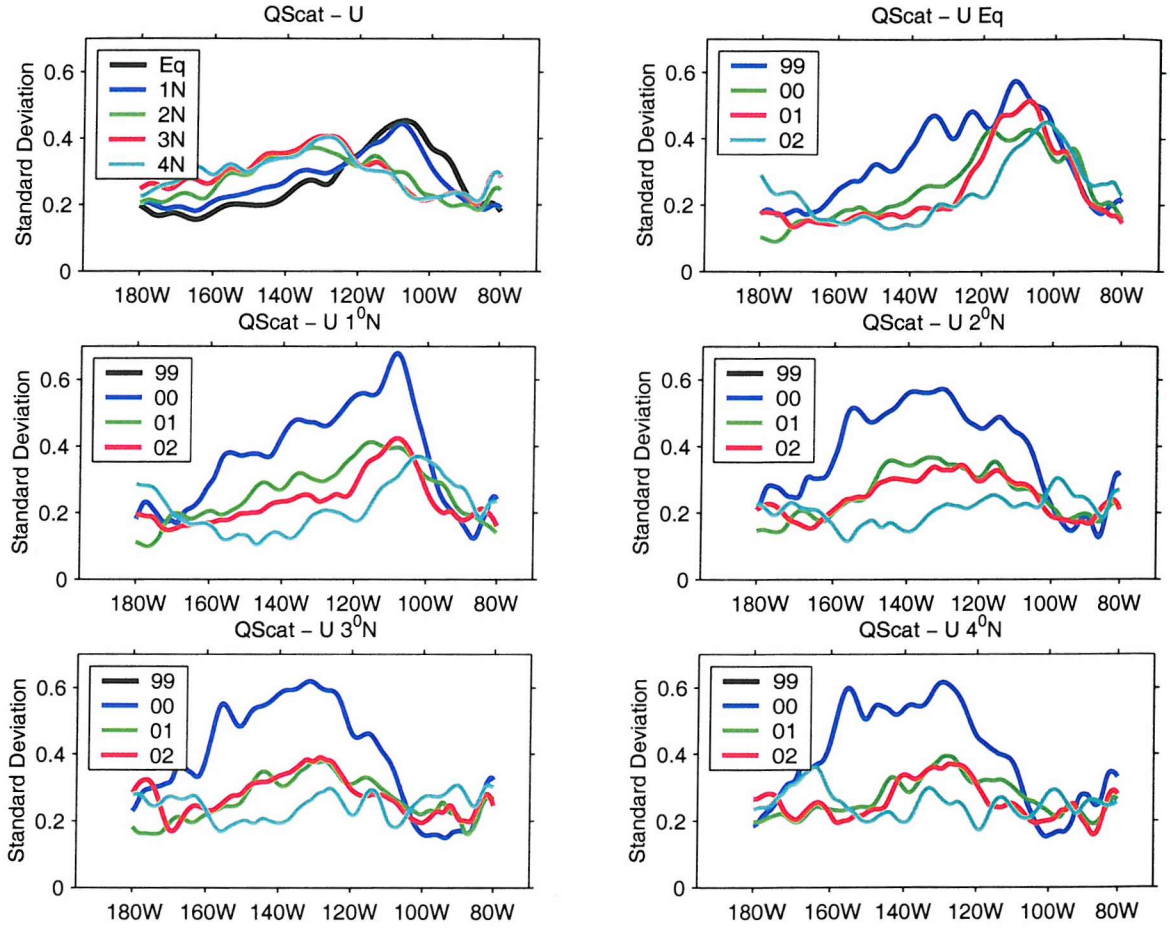

Figure 3.8: Longitude STD plot of wind magnitude derived from QuikScat.

The standard deviation performed for each latitude considering the entire period (1999-2002) is shown in Figure 3.8. This plot suggests that the maximum variability in the magnitude of the wind occurred during the 1999 TIW season, when La Niña was established. Spatially, the maximum tends to occur at the Equator and 1°N extending longitudinally from 90°W to 120°W, approximately. The wind magnitude variability at these latitudes are

due to the larger meridional wind component variability contribution, near the Equator. On the other hand, the zonal wind component tends to display a larger variability towards 2°N to 4°N and westward displaced compared with the meridional wind component, extending longitudinally from 160°W to 120°W, approximately. The meridional and zonal components analyzes are not shown.

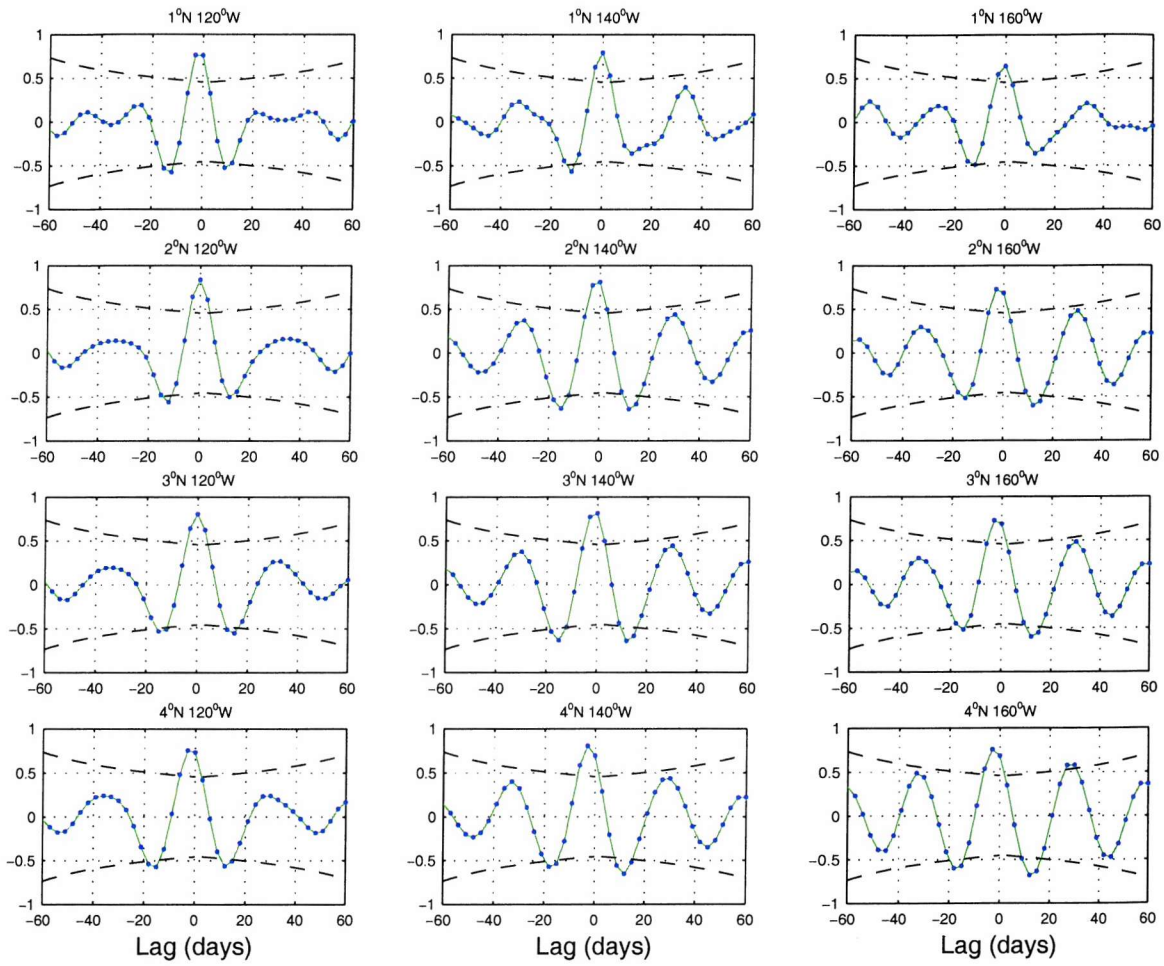

Figure 3.9: Cross correlation between SST and wind magnitude performed at 12 different locations displaying the time lag (x-axis) and correlation coefficients (y-axis). Dashed lines are the statistical significance threshold levels at 95 %. The locations are displayed on the top of each graphic.

The co-variability of westward propagating signals considering both SST and wind magnitude are analyzed by means of calculating the cross-correlations between time series sampled at different locations, as shown in Figure 3.9. SST and surface wind speed are apparently in phase when the lag correlation in days is zero and roughly opposite phase (180°

approximately) around ± 12 days (with deviation of ± 3 days). We have found the most significant correlations, at 95 % level, in the locations from 140°W to 120°W and 1°N to 3°N which represents a region where TIWs are most active.

These results reinforce the Wallace *et al.* (1989) and Hayes *et al.* (1989) suggested mechanism which says that SST is coupled with wind through the stability change in the atmospheric boundary layer, i.e. that buoyancy instability over a warm region of the TIW reduces vertical wind shear in the ABL. Our results also extend Liu *et al.* (2000) where they have tested this hypothesis by analyzing just one TIW season during the second half of 1999, when a La Niña episode was established in the Pacific ocean. Since we are using the whole data period, without distinction of TIW levels of activity, the results are suggesting that this ocean-atmosphere coupling might be valid for any TIW season, independent if the season has or has not high wave activity.

However, around 160°W the wind-SST coupling appears to be slightly shifted. According with Liu *et al.* (2000) in this region and northwards of 3-4°N different mechanisms may become important in governing the wind-SST coupling. Apparently, this is in contrast to Polito *et al.* (2001) who suggest that TIWs currents in the lower ABL region introduce a significant bias in scatterometer vector wind measurement. If it was the case the ABL TIW imprint would be in phase with the oceanic signals since the waves are still active at this longitude. We will further discuss the TIW ocean-atmosphere coupling in the Chapter 4.

3.4.3 Height variability

Both SST and SSH exhibit a similar wave cusp shaped pattern when spatial fields are plotted (see for instance Figure 3.1), but here we restrict our objective analysis to zonal time series at 3.5°N and 4.5°N latitudes, because this is a common region with higher variability for both SST and SSH. The TIW imprints are evident in the sea surface height anomalies as shown by the plots in Figure 3.10. In the SSH anomaly fields the TIW exhibit their strongest westward propagating signal during 1998 and 1999, similar to the SST observations

However, the TIWs imprint exhibit slightly different spectral characteristics comparing both fields. In the SSH anomaly fields TIWs display a longer wavelength and larger period compared with TMI. The values are λ=14.0 ° and Γ=31.5 days for SSH while λ=12.2 ° and

Γ=27.6 days for SST.

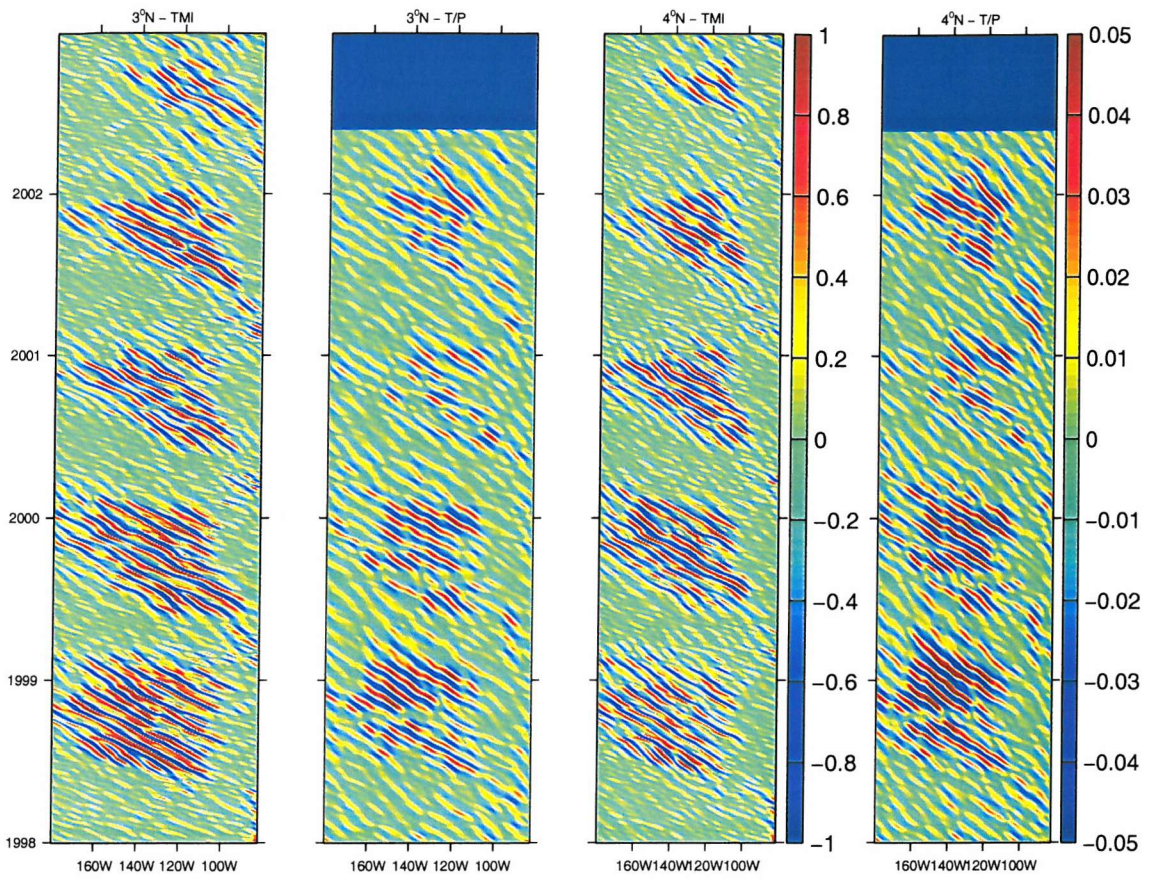

Figure 3.10: Time-longitude plots of SST derived from TMI and SSH anomalies derived from T/P data.

The westward propagating signals co-variability of both SST and SSH have been analyzed by means of calculating the correlations between time series sampled at different locations as shown in Figure 3.11. The most significant correlations are found at 120°W near the region where SST present the largest variability (see Figure 3.5). The statistical analysis reveal clusters of few correlation coefficients at lags of 6, 9 and 12 days. These correlations are significant at 95 % level with maxima at 6 and 9 days. Apparently, they are more significant at 2°N and 3°N latitudes in the easternmost region sampled, at 120°W of longitude. Westernmost of this region there are some marginal correlations.

These correlation plots are also suggesting two relevant aspects. One is that SST and SSH are 90° phase shifted, approximately. The other, is that heat might be meridionally (either north or southward) transported by the geostrophic currents causing the SST anoma-

lies. As suggested by Polito *et al.* (2001), northwards (southwards) current associated with positive (negative) zonal SSH anomalies of TIWs transports cold (warm) waters outward (inward) of Cold Tongue region. This interpretation, they say, is in agreement with Flament *et al.* (1996) where they have mapped a TIW, SST and circulation, using high resolution observations. Our results re-enforce and extend Polito *et al.* (2001) findings since they have analyzed only one TIW season in 1996, when a weak La Niña episode was established in the Pacific ocean. We suggest that SST-SSH phase shift might occur independent of the TIW level of activity.

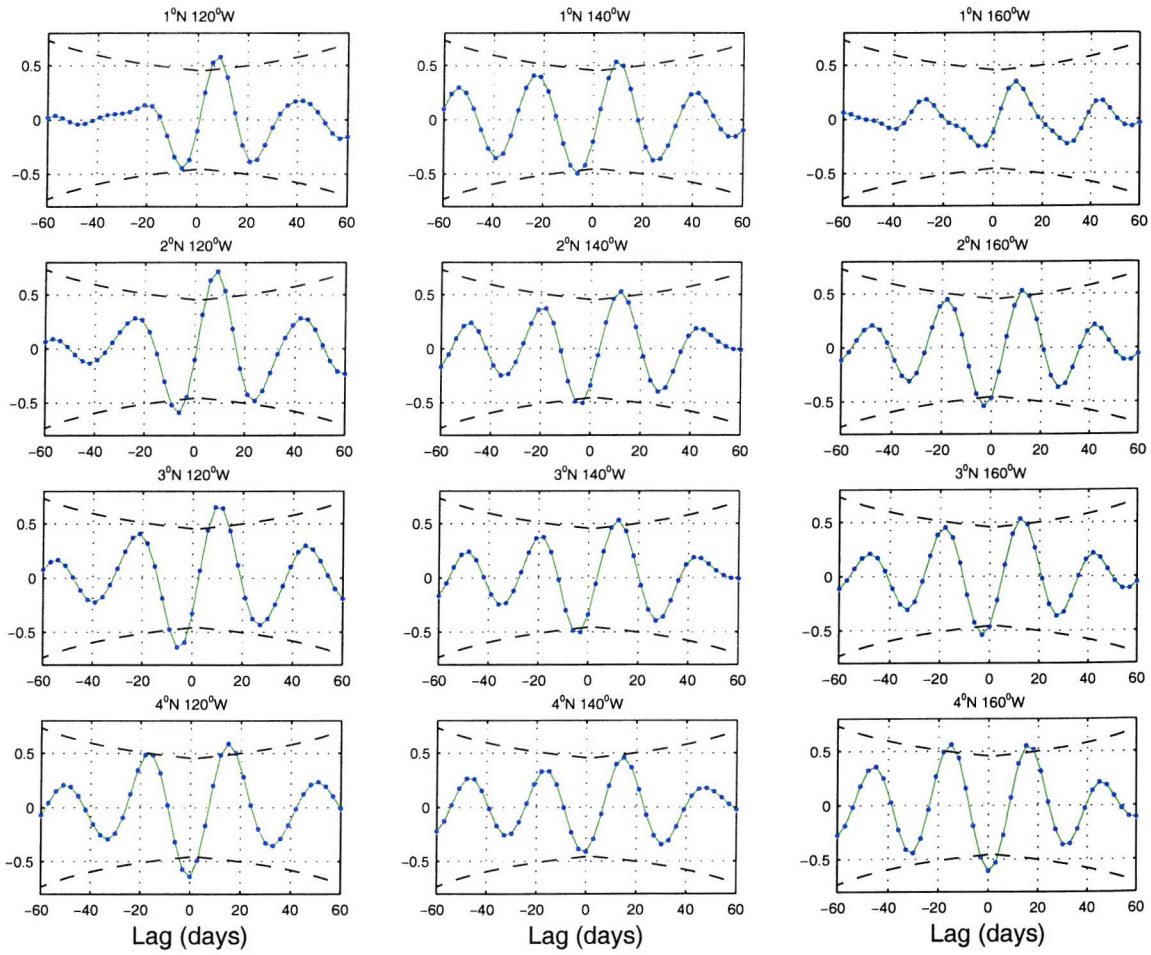

Figure 3.11: Cross correlation between SST and SSH anomalies performed at 12 different locations displaying the time lag (x-axis) and correlation coefficients (y-axis). Dashed lines are the statistical significance threshold levels at 95 %. The locations are displayed on the top of each graphic.

3.5 Summary and Conclusions

Descriptions of TIW variability characteristics in the tropical Pacific ocean as function of the large scale climate conditions and interannual variability, such as ENSO, necessarily rely on the availability of long term time series data.

This chapter has presented the TIW variability using four years of high resolution satellite data. It is not a long time record when the intention is to study TIWs interannual variability and climatology. But this chapter does extend previous studies which have been, restricted to the analysis of TIWs in one season; particularly during La Niña episodes, e.g. Masina *et al.* (1999), Chelton *et al.* (2000), Kennan and Flament (2000), Wentz *et al.* (2000), Liu *et al.* (2000), Hashizume *et al.* (2001) and Polito *et al.* (2001).

This study is based on available high-resolution SST and wind measurements made by two different types of microwave instruments flying on board of two satellites to evaluate the annual and interannual TIW variability. Additional examinations are made by means of comparisons between SST and SSH using the T/P data.

As others have found (Liu *et al.*, 2000, Hashizume *et al.*, 2001), the TIW ocean-atmosphere coupling is caused by ABL instability and mixing. Our results suggest that this mechanism of wind-SST coupled variability may occur not only during La Niña years, when TIWs are more actives.

The SST-SSH co-variability phase shift might occur independent of the TIW season activity. We extend Polito *et al.* (2001) findings since they have analyzed only one TIW season in 1996, when a weak La Niña episode was established in the Pacific ocean.

It is seen from the observational analysis that during La Niña years the wind over central equatorial Pacific is stronger when compared to normal and El Niño years. There is a clear evidence that TIW have their activity increased when they are subjected to strengthened wind stress conditions either in La Niña years or, *by analogy*, when numerical simulations are carried out subjected to stronger wind stress (see for instance Section 2.7.1).

Both observational and model results tend to agree, showing larger TIW wavelengths and shorter periods when the ocean is under action of strengthened wind stress. For the

observational study data this occurs when La Niña conditions prevail on the equatorial Pacific and on simulation results when the model is forced by strengthened winds.

The TIWs interannual variability investigation would greatly benefit by the availability of longer term high resolution satellite images and *in situ* data. An alternative way to study this would be by undertaking numerical simulations using a more realistic domain configuration and forcing fields. Experiments need to be able to simulate NECC since important parts of the equatorial energetic are dependent of this current. A multi-annual integration including several ENSO episodes on this representation would help on the robustness of the statistical calculations and energetics of TIWs since there is still ongoing debate about the waves energy sources, as pointed out in the previous chapter.

Chapter 4

The coupling between TIW and the ABL

4.1 Introduction

TIWs and associated vortices are an oceanic phenomenon originated from the shear instabilities of the equatorial ocean current system. While great attention has been given to the oceanic signal, several studies have shown that there are signals of TIW activity in the lower atmosphere, within the atmospheric planetary boundary layer (ABL). These include surface wind modulation, water vapor and nebulosity. Studies investigating the SST influence on surface winds over the eastern equatorial Pacific were made in the late 80's by Lindzen and Nigam (1987), Hayes *et al.* (1989) and Wallace *et al.* (1989). These studies have proposed mechanisms for the interaction between the TIW oceanic signals and atmospheric signals.

One hypothesis (Lindzen and Nigam, 1987) attributes surface wind modulations to the variations in the Sea Level Pressure (SLP) field, linked to the TIW SST signals. Lower (high) pressures are found over warmer (cooler) water and as a consequence the strongest wind should be found at the highest pressure or SST gradients. The second hypothesis stated by Wallace *et al.* (1989) and Hayes *et al.* (1989) is that TIW SST anomalies induce ABL stability changes which in turn affect the wind variability. In this hypothesis air buoyancy is increased over the warmer waters, reducing the wind shear in the boundary layer thus producing stronger winds at the surface. Strongest winds should be found over warmest waters. Wallace *et al.* (1989) showed the antisymmetry in the climate over the eastern Pacific

with the cold tongue SST being centered at 1°S and a strong frontal region centered at 2°N. The boundary layer air originating over the cold tongue (southern hemisphere) crosses meridionally the equatorial region and joins the Intertropical Convergence Zone (ITCZ) around 8°N. All these systems tend to be stronger during the cold season, which extends from July to November, when the meridional asymmetries are strongest. The oceanic frontal zone becomes hydrodynamically unstable, giving rise to westward propagating waves with periods of a few weeks. The atmospheric boundary layer undergoes a transition from a stable condition to an unstable condition as the air flows from the cold region to the warm (NECC) region across the SST front.

Xie *et al.* (1998) have studied the impact of these waves on the atmospheric boundary layer, analyzing the output from an AGCM averaged over the last 400 days of integration, satellite derived SST and wind data on a weekly time scale. The AGCM was able to reproduce roughly the wind field and divergence when compared with the satellite observations. Their results showed atmospheric waves with shallow vertical structure trapped in the ABL and that the ocean-atmosphere coupling happens on time-scales shorter than one month. TIW affects the horizontal wind direction and intensity in the ABL while ENSO modes affect the large scale atmospheric circulation, modifying the deep convection.

Recently, some key points of the TIWs have been studied using state of art data collected by satellite. The question concerning the ocean atmosphere interactions and influence of the TIWs on the surface wind has been revisited by Liu *et al.* (2000) and Chelton *et al.* (2001) and the TIWs themselves by Chelton *et al.* (2000). Many of these studies have used data from the microwave imager sensor TMI onboard the joint US/Japan Tropical Rainfall Measuring Mission (TRMM) satellite. This satellite sensor has been observing the Earth, mainly in the tropical region, in the spectral band of 10.7-85.0 GHz. The SST data have a daily temporal resolution and high spatial (approximately 46 Km) resolution. The atmosphere is nearly transparent to microwave radiation allowing SST data to be collected in all weather situations, except in rainy conditions. In other words, the atmosphere is seen free of clouds in nonraining situations allowing the acquisition of a nearly uninterrupted time series.

Using satellite-derived data Liu *et al.* (2000) clearly showed the manifestation of TIWs over the northern front of the Pacific cold tongue and using a zonal band pass filter they

were able to isolate the TIW signal in SST, wind components and wind speed to analyze the phase propagation differences. They found in a region between 1.5°N to 3.5°N and 105°W to 145°W SST that was in phase with the wind speed whilst the meridional component of the wind was out of phase (−155°). The wind response to the SST gradients is shown in Figure 1.3 (Liu *et al.*, 2000). As the wind moves over these SST anomalies it is accelerated and decelerated producing centers of convergence and divergence at maxima SST gradient regions. The convergence maxima (minima) also coincide with the water vapor maxima (minima), where convergence (divergence) feeds (withdraws) the water vapor up in the atmosphere increasing (decreasing) the instability in the air column. The water vapor increase in this region might be a consequence of the warm waters and air advection. Based on their findings Liu *et al.* (2000) suggest that the modification of the surface winds is due to the ABL stability changes, agreeing with Wallace *et al.* (1989).

These results have been corroborated by Hashizume *et al.* (2002) using a sequence of atmospheric radiosondings of air temperature, humidity and wind obtained during a cruise sailing through developed TIWs in the Pacific Ocean. From their Figure 9, can be seen that the atmospheric response to TIWs extends through the whole ABL and modulates its vertical extension. Over warm waters the atmospheric boundary layer is unstable increasing the vertical mixing and the ABL height. The turbulence within the vertical column increases also and more momentum is transferred downwards decreasing the vertical shear and accelerating the surface wind over warmest waters in agreements with the previous studies.

Recently, Small *et al.* (2003) have re-opened the discussion about which mechanism is prevailing in the wind surface modulation. Using a high resolution regional climate model with improved physics and forced by TMI SST have examined the atmospheric impacts to Pacific TIWs. Their results suggest that horizontal advection changes the SLP phase relation with SST, the high and low pressure centers are located downwind of the cold and warm SST anomalies centers. Also their momentum budget analysis suggests that pressure gradient term is dominating the balance, besides of the vertical mixing and horizontal advection.

The differences and similarities of the TIWs in the Pacific and Atlantic oceans have been explored by Hashizume *et al.* (2001) also using the TMI sensor during the second half

of 1999, when a well established La Niña was present in the Pacific. The cold tongue in the Atlantic has a faster development and decay than that in the Pacific. Possibly associated to climatic and climatological differences, the wavelength of the Atlantic TIW is smaller (9° of longitude) when compared with the Pacific (12°). It was also observed that in both oceans TIW activity has some indirect impact on the southern edge of the ITCZ.

Thus, while many studies in the past have shown that TIWs originate from oceanic instabilities the discussion above show that there is also an imprint of TIWs in the atmosphere via mainly ABL stability modulations. In this chapter, we explore the ocean-ABL coupled interactions and the main points addressed here are:

- Can we simulate TIW impacts in the atmospheric boundary layer using a simplified coupling scheme?

- Is there an ocean-atmospheric coupling in which the ABL feedback impacts onto oceanic TIW characteristics?

Up to now from our knowledge, the extent of TIW ocean-atmosphere coupling and the associated oceanic feedbacks has not been specifically addressed by other studies. We chose to study the TIW ocean-atmosphere interactions using an OGCM coupled with a simplified statistical ABL scheme.

The remainder of this chapter is organized as follow. In Section 4.2 the ocean model configuration, ABL scheme formulism, coupling coefficients calculation and system setup are presented. In Section 4.3 the model spin-up and sensitivity experiments are described. In Section 4.4 the equatorial current system, TIW simulations and variability are analyzed. The model energetics and wind work are investigated in Section 4.5. A brief summary and conclusions are presented in the last section (Section 4.6).

4.2 Model configurations

4.2.1 Ocean Model

In this study we use the LODYC Ocean General Circulation Model (OGCM) (Madec *et al.*, 1998) in a tropical Pacific configuration which is the same used in Chapter 2. However, it has a slightly different grid configuration and a brief description of the main characteristics follows.

The domain used for this study covers the tropical Pacific from 30°S to 30°N and from 130°E to 70°W, with realistic representation of coastlines. The meridional resolution is 0.5° in the equatorial belt from 5°S to 5°N increasing grid space up to 2° at the southern and northern boundaries. The resolution in zonal direction is 1°, equally grid spaced along the domain.

The model has 31 levels in the vertical, with the highest resolution of approximately 10 meters in the top 150 meters. Below this depth the resolution decreases down to 500 meters near the ocean bottom at 5000 meters (see Appendix B for more detail about the grid resolution).

The lateral mixing for tracers and momentum is applied along isopycnal surfaces following the scheme described in Appendix A and in Lengaigne *et al.* (2003). The mixing coefficient used is 2×10^3 $m^2 s^{-1}$. The results produced by the isopycnal mixing parameterization have suggested a better representation of the eddy effects in the equatorial region and of the tropical circulation, as suggested by Lengaigne *et al.* (2003) and also seen in Chapter 2.

4.2.2 The coupling scheme

In order to investigate whether the ABL-TIW induced patterns do influence the TIWs themselves we assess the differences between experiments forced by specified wind stress and experiments where a ocean-ABL coupling scheme at the TIW scale has been introduced. The experiments are run with the wind stress specified as follows:

$$\tau = \tau_0 + \begin{pmatrix} \alpha SST' \\ \beta SST' \end{pmatrix} \tag{4.1}$$

where τ_0 is the October climatological wind stress used for the control experiment and SST' is the difference between the model SST at a particular instant with the long term averaged $\overline{SST}$ from the control experiment. The α and β values in Equation 4.1 used for these experiments are given in Table 4.1. The zonal and meridional coupling coefficients used in STD experiment are computed from a statistical regression between the 10-50 days filtered Quikscat wind stress and TRMM SST at 140°W, 2°N (the region where the highest correlation of 0.5 between these two data set was found) covering the period 1999-2001.

This is an approach similar to that used in Hashizume *et al.* (2001) and Polito *et al.* (2001) but here it is applied to relate wind stress (rather than wind) to SST. While we are aware that this is a very crude approach, the results obtained with our simplified scheme produces wind stress anomalies consistent with the magnitude and spatial patterns found in observations (see for instance Figure 1.3)

In one way of the ocean-atmosphere coupling, the ABL scheme can be forced by SST produced by the oceanic model and those are included in the wind calculations. On the other way the ABL returns back the wind stress to force the ocean model closing the ocean-atmosphere coupling loop. A simple formulism to calculate the surface wind stresses based on a given background wind plus the information coming from the ocean through SST anomalies is used.

Experiments	α	β
STD	-0.02	0.008
MID	-0.03	0.012
HIG	-0.05	0.020

Table 4.1: Linear regression coefficients calculated from the TMI SST and Quickscat scatterometer. Time series data are coincident in time, covering the period from June 1999 to December 2001, and space. α and β represent the zonal and meridional directions, respectively.

The preliminary results have shown considerable differences on the simulated mean state when different experiments are compared. The question that arose is; are the differences

seen in the mean state caused by the TIWs feedback themselves or caused by the coupling effects in the regions outside of the TIW activity region?

In order to minimize the ABL coupling impacts on the oceanic mean state, the active coupling region is restricted to an equatorial area where the TIWs are generated. The ITCZ is located northward of this area and the coupling mechanisms may differ. Thus, α and β are defined as function of the latitude and longitude limits respectively. The coefficient values are multiplied by one within a region chosen for active coupling region, extending from 9°S to 9°N and from 160°E to 90 °W, and zero elsewhere. In order to avoid an abrupt change in the active coupling a 3° wide transition zone decaying to zero in all four directions (north, south, east and west borders) is applied.

4.3 Experiments performed

4.3.1 Spin-up and control experiments

The ocean model is first spun-up with October climatological wind stress forcing ERS+TAO (Menkes *et al.*, 1998), starting from rest and Levitus and Boyer (1994) temperature and salinity. The net heat flux is parameterized as a relaxation towards October climatological SST observations (Levitus and Boyer, 1994) using a relaxation coefficient of -40 W $m^{-2}K^{-1}$. There is no relaxation to climatological salinity. The results are analyzed after the 60^{th} year of integration when the solution has reached a statistically quasi-steady state.

In order to be coherent with the sensitivity experiments comparison, an additional two years experiment is performed restarting from the spin-up and with α and β set to zero. The only variability in this experiment is linked to tropical instability waves and will be further described in Section 4.4.

4.3.2 Coupled experiments

Three two-years experiments are performed with non-zero values of α and β, i.e. allowing a coupling between the ocean and the atmospheric boundary layer. The α and β values used for these experiments are given in Table 4.1. The zonal and meridional coupling coefficients

used in the STD experiment are the values computed from the statistical regression as defined in the Section 4.2.2. In experiment MID, the coefficients are multiplied by a factor of 1.5 and in the HIG, they are multiplied by a factor of 2. The effects of ABL coupling for each case are compared with the control run experiment (CTL). The 60^{th} spin-up year which used constant October forcing is used as initial conditions. The coupled experiments differ only in the coupling strength applied, all the other parameters and configurations are kept identical.

4.4 Mean state and TIW

4.4.1 The equatorial current system

The Figure 4.1 shows a latitude-depth section at 120°W of 2-years mean zonal currents in the upper panel, zonal surface current in the middle panel and SST in the lower panel. All these results are from the CTL experiment. The equatorial current system is simulated quite well displaying the eastward flowing Equatorial Undercurrent (EUC), the westward flowing South Equatorial Current (SEC) both northern and southern branches and the eastward flowing North Equatorial Counter Current (NECC). Moreover, the SEC southern branch is weaker and shallower compared to the northern branch. Observational studies have demonstrated that SEC is stronger in its northern branch (Qiao and Weisberg, 1995) and in some cases it consists of a single branch to the north (Luther and Johnson, 1990).

The CTL mean currents are reasonably well simulated and in relative agreement with Vialard *et al.* (2003a) and Lengaigne *et al.* (2003) with respect to the equatorial current structure. They have used a similar model configuration forced with ERS+TAO (Menkes *et al.*, 1998). However, in their case the simulations are done using seasonal varying wind, which differs from this study where the forcing is kept constant. This might explain some differences from our mean state patterns compared to theirs, such as the weaker southern branch in our mean state.

The surface current field shows a region of large variability along the equator and extending northward coincidentally with the strong shear region between EUC, SEC northern branch and NECC. The SST in Figure 4.1 exhibits a well defined cold tongue region ex-

tending further west up to 160°W approximately. This field also shows a strong meridional frontal gradient north of the equator, typical of the period when the Cold Tongue is well established.

The SST also shows a region of large variability as seen in the zonal current over the same region where a sharp temperature gradient is located. The large variability region seen in the currents and SST fields are associated with the TIW growth region and it is where the waves are most active. The region with largest variability extends from 100°W to the date line, approximately.

The CTL experiment exhibits TIW activity as shown in Figure 4.5 in the left panel. The figure displays a time-longitude Hovmöller diagram of SST. The TIWs are identified in the time-longitude plots as those features propagating westward with their largest variability over the eastern part of the model domain where the SEC, EUC and NECC shear currents variability and frontal gradients are most intense. This variability decreases westward where TIWs tend to dissipate.

The waves produced in the CTL experiment exhibit organized propagation patterns as well as a larger variability in the eastern portion of the domain. The TIW activity identified in the SST fields are quite sensitive to the atmospheric ABL coupling. The results suggest a reduction in the wave activity when compared with the active coupling experiments. The characteristics of the coupled TIWs will be further discussed in Section 4.4.2.

When the ABL scheme is used on its active mode, i.e. allowing ocean-atmosphere freely interact to force the ocean model, the equatorial ocean simulation is significantly affected by the coupling strength applied as showed in Table. 4.2. There is an increase on the EUC maximum speed for the STD experiment compared with CTL. The same pattern is found for the other experiments, where the ocean-atmosphere coupling is made stronger (e.g, MID and HIG). However, the other currents, e.g. SEC and NECC, do not follow this pattern of a linear increase in their maxima.

By analyzing a series of SST snapshots from CTL and STD experiments, it is seen that TIWs activities are simulated over the latitudes between 2°N to 4°N and 2°S to 4°S over the eastern part of the domain, exhibiting a well defined cusp-shaped wave pattern. For instance one snapshot is shown in Figure 4.4 (upper panel) for the STD experiment. These

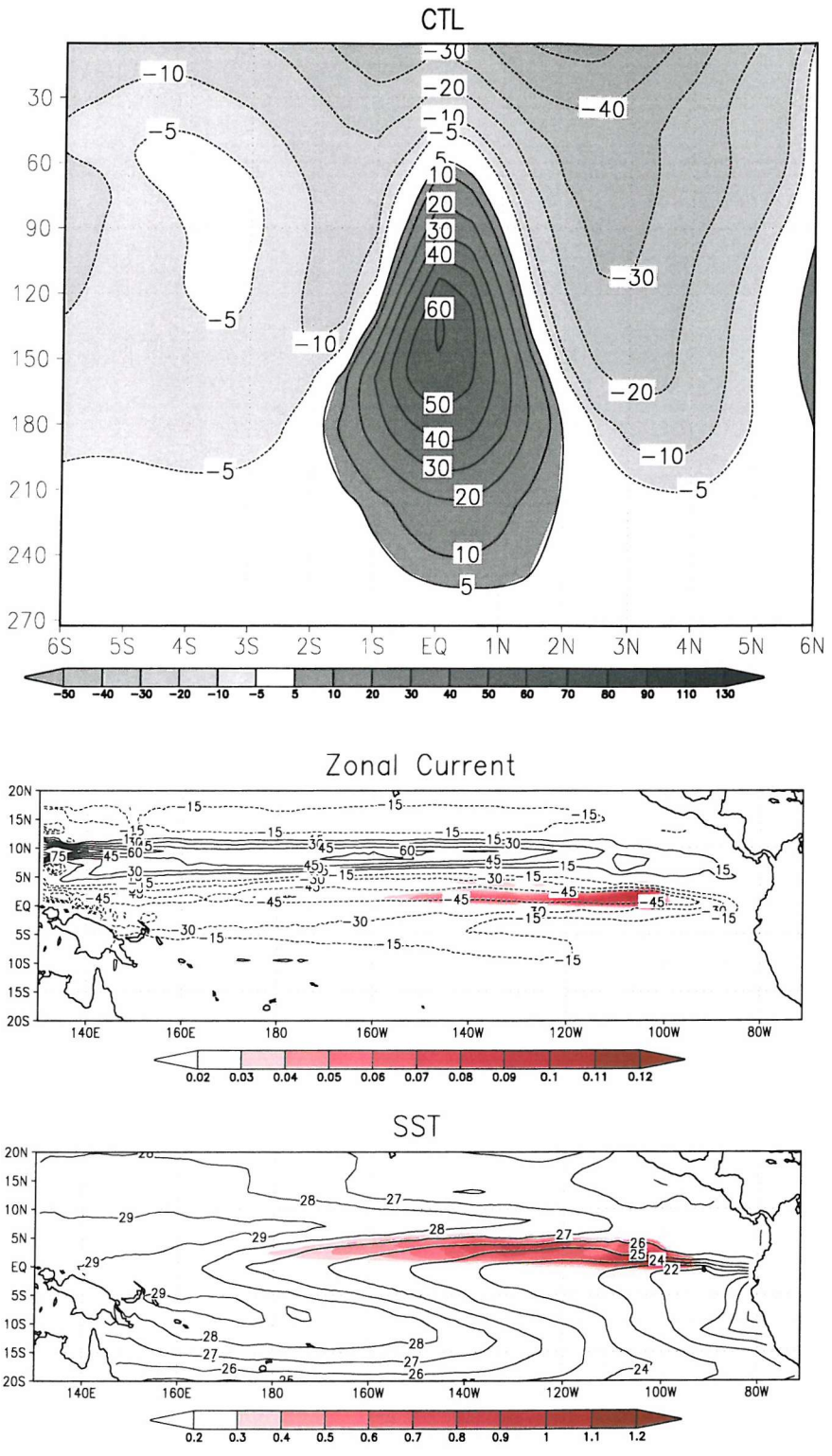

Figure 4.1: EUC vertical section averaged over $130°W - 90°$W band of longitude (upper panel). Middle and lower panel are zonal current and SST, respectively. Shaded areas in these two last plots denote standard deviation. Units are cm s^{-1} for the current and $°C$ for SST.

TIWs features are similar to those previously shown by Legeckis (1977), Chelton *et al.* (2001) and Thum *et al.* (2002). The waves extend approximately from 100°W to 160°W of longitude, coincidentally with the regions of largest variability as shown in the Figure 4.1.

Current	CTL	STD	MID	HIG
EUC	61.06	67.97	69.62	76.71
SEC	-52.07	-52.69	-52.00	-58.80
NECC	60.65	61.09	61.17	58.98

Table 4.2: Maximum values of speed currents for each experiment performed. Units are in cm s^{-1}

To diagnose the differences found in the zonal current system produced by the coupling the terms in the zonal momentum equation are calculated, as done in previous sensitivity studies, e.g. (Maes *et al.*, 1997, Yu and McPhaden, 1999, Lengaigne *et al.*, 2003). Harrison *et al.* (2001) have analyzed the TIW role in the momentum equation tendencies in the boreal springtime surface current reversal that occurs in the equatorial Pacific. In our case we analyzed the total zonal momentum equation trends. The methodology used in this analysis is shown in Appendix C. The results are shown in Figure 4.2 and briefly commented.

In the CTL experiment, the zonal pressure gradient (ZPRG) is the dominant positive term in the balance, accelerating the flow eastward to a lesser extent the vertical advection (VADV), towards the surface. The meridional advection (MADV), vertical diffusion (VDIF) and lateral diffusion (LDIF) are negative and counteracting the zonal pressure gradient(ZPGR) and vertical advection (VADV). In the upper part region of the EUC, around 40-100 meters depth, ZPGR and VADV are the two dominant terms accelerating eastward. The former terms are balanced by VDIF and to a lesser extent by MADV. Similar results to our CTL experiment are found in the literature, e.g. Maes *et al.* (1997), Harrison *et al.* (2001) and Lengaigne *et al.* (2003).

Nevertheless, when the SST-wind co-variability is made active the balance suggests a weakening in the meridional component of the horizontal advection term (MADV). The negative MADV magnitude decreases when the ocean-atmospheric coupling is made stronger. Such weakening extends from the surface deepening down to the EUC upper part. Harrison *et al.* (2001) in their study have found that the weakening of this term associated with

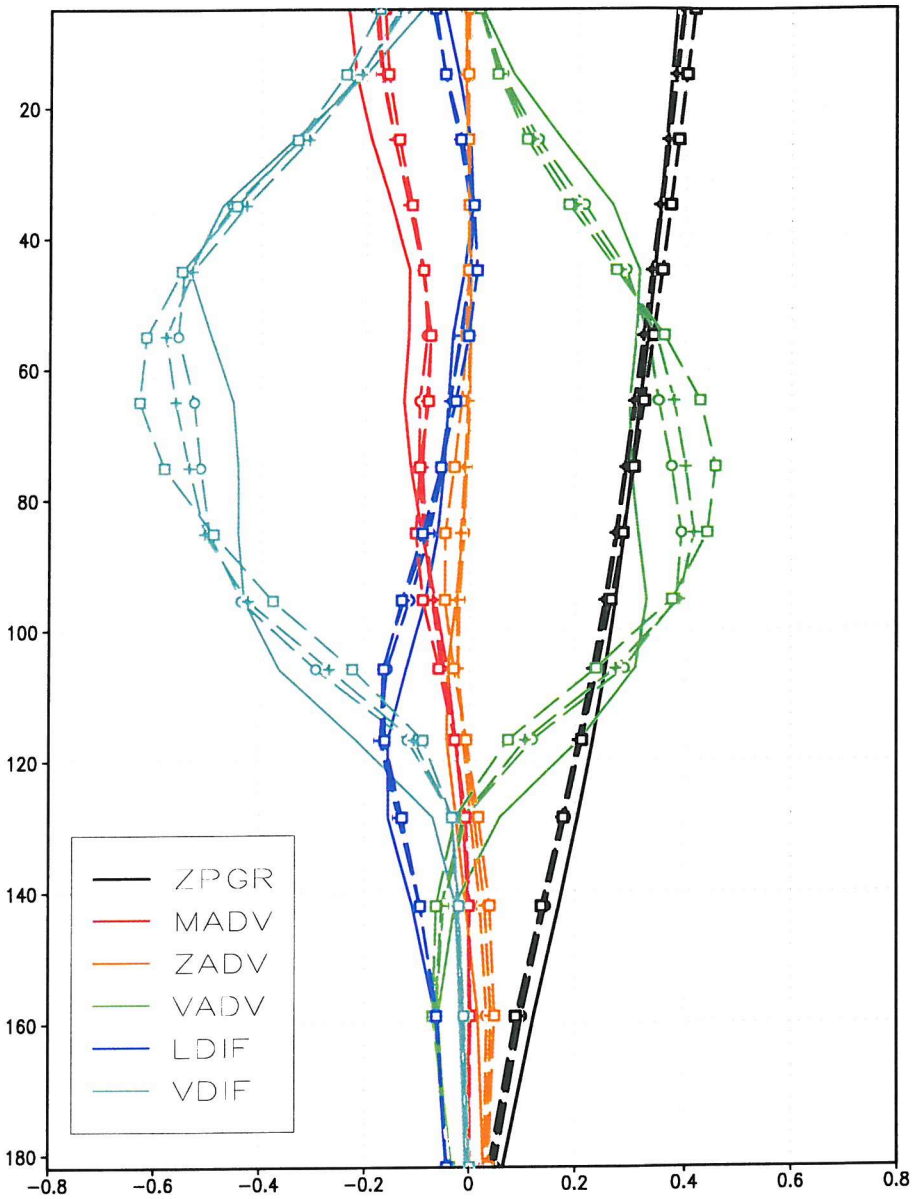

Figure 4.2: Vertical section of the mean zonal momentum equation trends (units are 1×10^{-6} m.s^{-2}). Solid line is CTL experiment. Dashed lines are; STD with open circle, MID with plus sign and HIG with open square. See Appendix C for methodology.

TIW activity is seen to be the primary source of the spring TIW tendency for eastward acceleration.

However, the other balance terms are also sensitive to the coupling and they might play a role in the EUC speed; it is not clear which one of them are responsible for EUC acceleration. In the same TIW time scale analysis we show that the meridional momentum flux is also decreased with TIW activity as discussed later in Section 4.4.4.

4.4.2 The effect of TIW activity on the surface stress

In this section we compare the TIW model generated for each coupled experiment, i.e. when the surface wind stress is simulated taking SST into the calculation. The TIW signal is enhanced by using a Finite Impulse Response (FIR) 2-D digital filter (Cipollini *et al.*, 2001, Liu *et al.*, 2000). The filter band-pass TIW within a selected range of wavelengths and periods from a 3-day average model output. In this chapter, we assume that, TIWs are all oscillations with longitudinal wavelength ranging from 5° to 25° and period from 10 to 80 days. These values are based on what has been reported in the literature on TIW spectral characteristics and also in some preliminary tests carried out before to define the filter parameters.

The STD experiment which uses the ABL scheme interactively with standard values for the coupling coefficients produces TIW imprints in the winds. The TIW imprints on the ABL are identified as those westward propagating features in both zonal and meridional wind stress components as showed in Figure 4.3. Their largest activity is towards the eastern part of the domain, coincident with the TIW maximum activity region in the SST fields as seen in Figure 4.5.

Two snapshots from the STD experiment are shown in Figure 4.4. The upper panel displays the SST field with filtered currents superimposed. The model simulates the cold tongue feature and also exhibits a well defined cusp-shaped wave pattern similar to those TIW patterns described in the literature (Legeckis, 1977, Chelton *et al.*, 2000). In the observed data, TIW appear as oscillations of the northern edge of the cold tongue and with a weaker activity at the southern edge (Chelton *et al.*, 2000). In this study, the model reproduces the observed TIW feature in the Cold Tongue northern edge but the activity

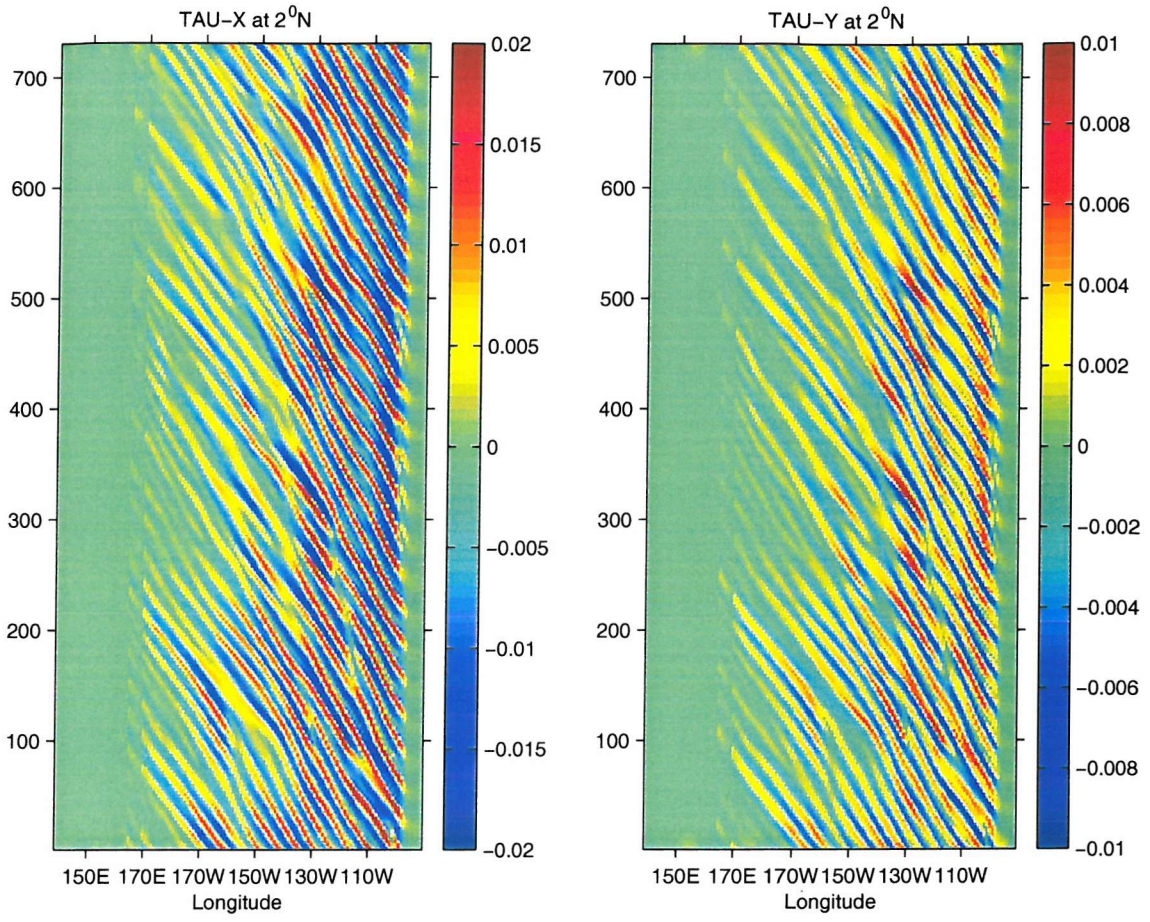

Figure 4.3: Time-longitude series showing the wind stress (zonal and meridional) components produced by the STD experiment. Units are Nm^{-2}.

in the southern is underestimated. As mentioned before this might be related to the weak SEC speed on its southern branch. The currents snapshot, shows clearly that TIWs act to stirring the cold and warm waters in this region. They act to draw out filaments of cold water from the tongue region and to bring warm water filaments into this region.

The lower panel of Figure 4.4 shows the SST with the wind stress, produced by the ABL scheme, superimposed on it. Both fields have been filtered and just the high variability part of them are retained. The positive (negative) blobs of SST anomalies represent the warmer (colder) waters being moved southward (northward) by the currents (as shown in the upper panel). The wind is superimposed on the filtered SST and suggests that as air moves across the isotherms it speeds up and slows down over warm and cold waters respectively, producing convergence and divergence centers over the SST maximum gradients.

This result suggests that the ocean-atmosphere coupling will have a tendency to decrease the TIW activity (as shown in Figure 4.5) by reducing the meridional momentum flux as further discussed in Section 4.4.4. The current and wind vectors have component acting in opposite directions, Figure 4.4. For instance, it is verified that current vectors are directed northwards right over the SST crest, mixing out cold water filaments and the wind is directed towards southeast/south direction. On the other hand, the warmer water filaments are brought into the cold region by the southward currents placed over the SST trough while the wind has a northward component.

Overall, the results obtained with the simplified ABL scheme are in close agreement with those shown by Liu *et al.* (2000) where they have used microwave satellite data to investigate the ABL instability mechanisms proposed by Hayes *et al.* (1989). It is important to note that the ABL scheme used here simulates wind anomalies in the same order of magnitude as those found by Liu *et al.* (2000) as well as displaying a similar spatial pattern.

The high frequency part of SST data is shown in Figure 4.5 which displays a Hovmöller (time-longitude) SST diagram for the CTL and the experiments where different coupling coefficients are applied. The TIWs propagate westward, exhibiting their largest variability over the eastern part of the model domain where the SEC, EUC and NECC shear currents and frontal gradients are most intense. This variability decreases westward where TIWs tend to dissipate.

The TIWs identified in the SST fields are indeed quite sensitive to the atmospheric ABL coupling. The waves produced in the CTL experiment exhibit more organized propagation patterns as well as a larger variability in the eastern portion of the domain, as shown in the left panel of Figure 4.5. The experiment using interactive ABL winds with standard coupling coefficients (STD) tends to damp out the TIW activity when compared with the control experiment (CTL) that uses constant wind forcing. The TIW variability is decreased further as the coupling coefficients are increased such as MID and HIG experiments, as shown in the Figure 4.5. The time-longitude results suggest that increasing the ABL coupling tends to produce waves that are not as regular as the in CTL experiment. Also, the dominant TIW speed is affected. The waves tend to propagate faster and have longer wavelength and period as the ocean-atmosphere coupling increases. The spectral characteristics will be further discussed.

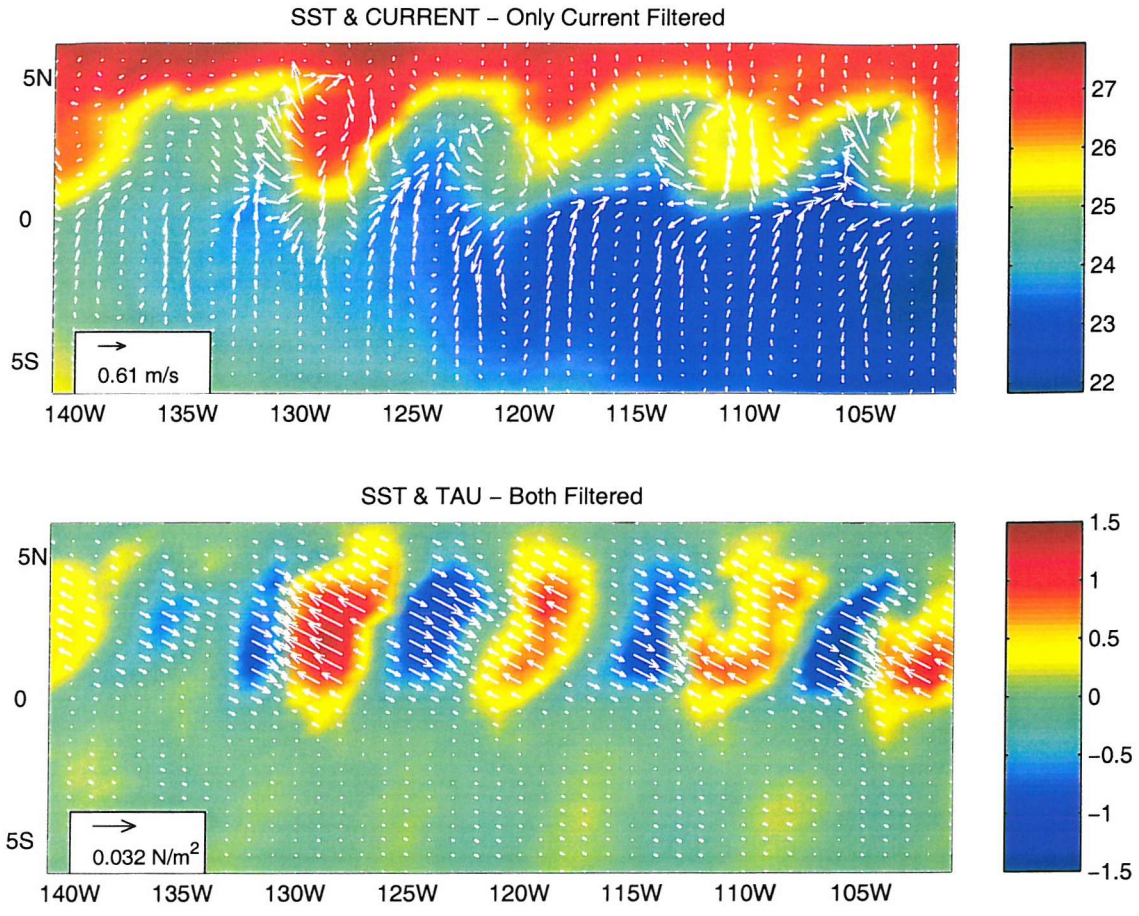

Figure 4.4: SST with filtered currents superimposed (upper panel). SST and wind stress superimposed, both filtered fields (lower panel). STD experiments

4.4.3 TIW variability

In order to quantify the TIW variability as a function of the coupling strength the SST and currents standard deviation is calculated using the total fields.

Horizontal structure

The horizontal or surface standard deviation, averaged over a latitudinal band extending from 5°S to 5°N, for the whole longitudinal extension, is shown in Figure 4.6. This figure also shows the regions where the experiment differences are statistically significant. The statistical F-test at 95% is applied as shown in Zar (1996) in order to find out the significance levels. The top color lines represent the significant difference of a given experiment at a given longitudinal region when compared to the CTL experiment.

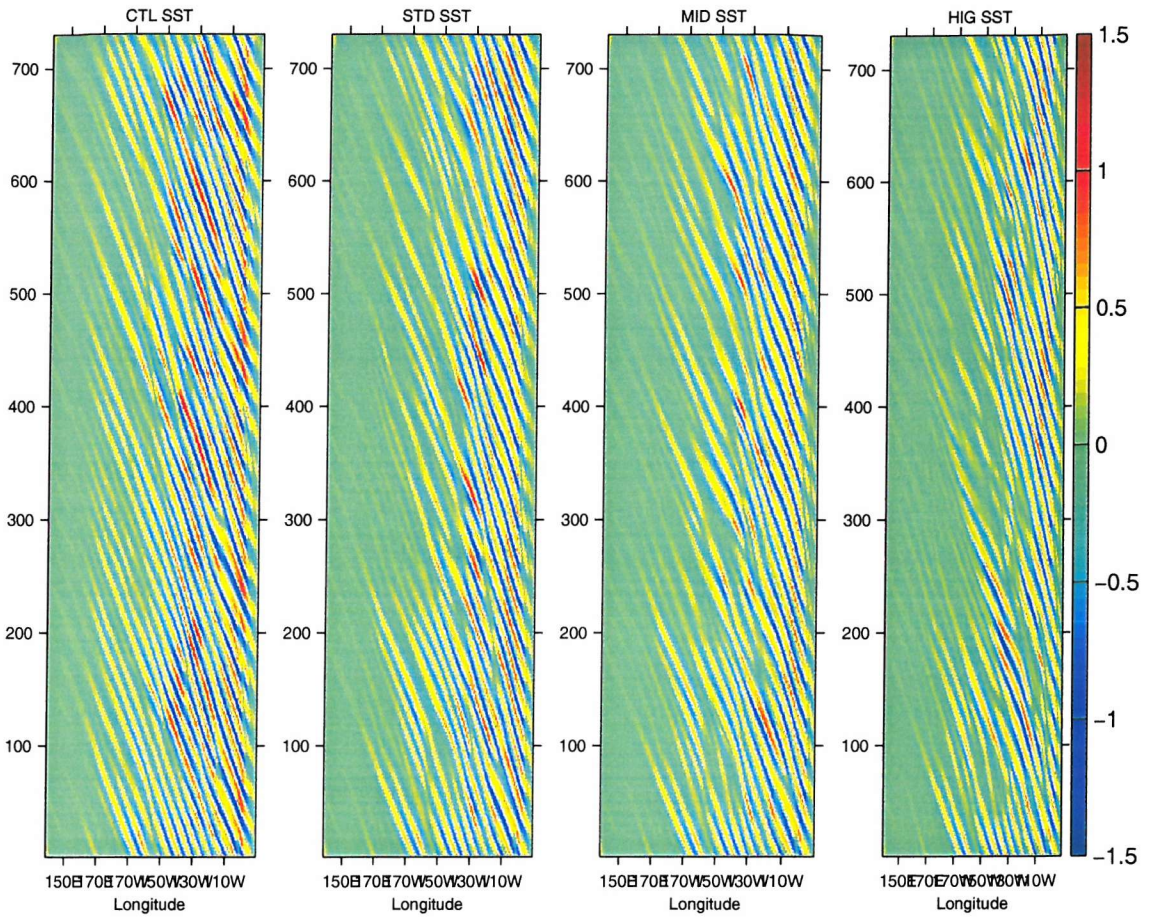

Figure 4.5: Filtered time-longitude SST displaying TIW for the CTL, STD, MID and HIG experiments averaged over the latitudinal band from 1°N to 3°N. Units are °C.

In an effort to map the coupled spatial structure of TIWs we follow the methodology used by Hashizume *et al.* (2001) and Small *et al.* (2003). The method consists of finding the linear relationship between two variables by means of regressing two-dimensional variable field onto the fixed point time series, such as $\mathbf{U}_{(i,j,t)}$ and $SST_{(t)}$; where $\mathbf{U}_{(i,j,t)}$ is either the zonal or meridional filtered current field and $SST_{(t)}$ is the filtered SST at a fixed point. Details of the statistical method are described in Hashizume *et al.* (2001).

The TIWs exhibit their largest surface variability over the eastern part of the domain with the maxima occurring towards 100-110 °W and decreasing towards the west where the waves tend to dissipate. The same characteristic is verified on the currents, zonal and meridional components as shown in Figure 4.6 on the middle and lower panels, respectively. As mentioned before, TIWs have their activity damped out when the ocean-atmospheric

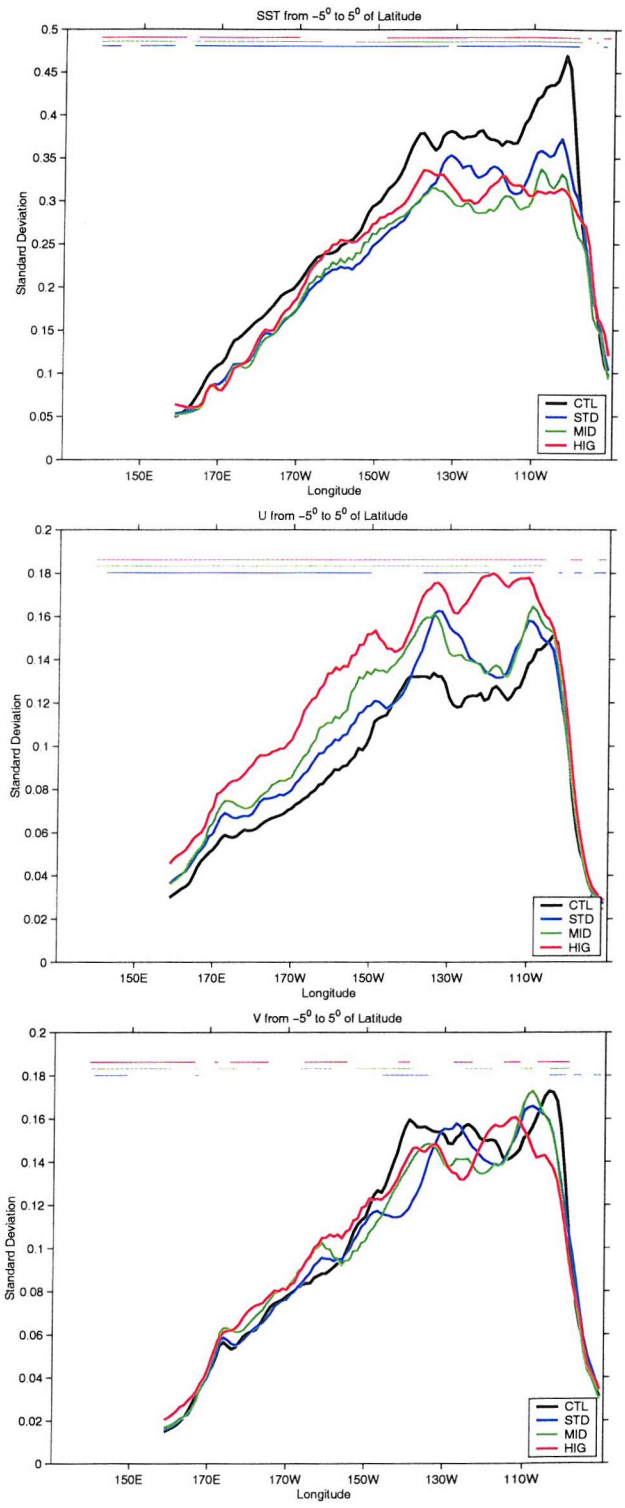

Figure 4.6: Meridionally averaged surface standard deviation, SST (upper panel), u (middle panel) and v (lower panel). The values are latitudinally averaged over the band from 5°S to 5°N.

boundary layer coupling is made stronger. The SST maximum variability is 0.47°C in the CTL experiment, 0.37°C in STD and 0.33°C in HIG, representing an approximate reduction of 21% and 30%, relatively to CTL; suggesting a roughly *inverse*[1] relationship between ocean-atmosphere coupling strength and SST variability. An analysis of a sequence of SST snapshots suggests that the wave shape is also modified. The TIWs are slightly squashed and stretched in the meridional and zonal directions respectively, as the coupling is strengthened.

However, the effects of coupling on TIW activity are less noticeable on the surface currents variability, particularly in the meridional component. The meridional variability is reduced, but not significantly. The maximum value found for the CTL experiment is approximately 0.17 m s^{-1} and it is reduced to 0.16 m s^{-1} in the HIG, representing a 6% reduction of the former. The surface variability in the zonal direction, exhibits an opposite behavior to that seen in SST and meridional current. The zonal variability is increased when the coupling coefficients are larger. The maximum value of variability is approximately 0.15 m s^{-1} in the CTL experiment and 0.17 m s^{-1} in the HIG, representing an increase approximated of 22%.

The large increase in the zonal current variability within the equatorial region is not only caused by the TIW activity. Apparently, two other factors are contributing to enlarge the zonal variability. The analysis of a current snapshot animation has revealed that the zonal background component exhibits a meridional oscillation, being displaced north and southwards as the coupling increases. Another factor contributing to the variability enhancement is the generation of a lower frequency propagation mode as the coupling strengthens and identified in the wavelet analysis.

The Figure 4.7 shows the zonal current time series and the respective wavelet analysis at the Equator and 100°W. This technique has been widely used in various climate data analyzes, e.g. Weng and Lau (1994) for tropical convection, Gu and Philander (1995) ENSO data and recently Cromwell (2001) studying the zonal propagation of energy in the North Atlantic. In the wavelet plots (Figure 4.7, lower panels), the vertical axis shows the wave periods in days and the horizontal axis the model time. The contour lines indicate both the 95% confidence level and the cone of influence (CI), below which edge effects may

[1] *inverse* here means that SST variability is damped out as function of coupling increasing

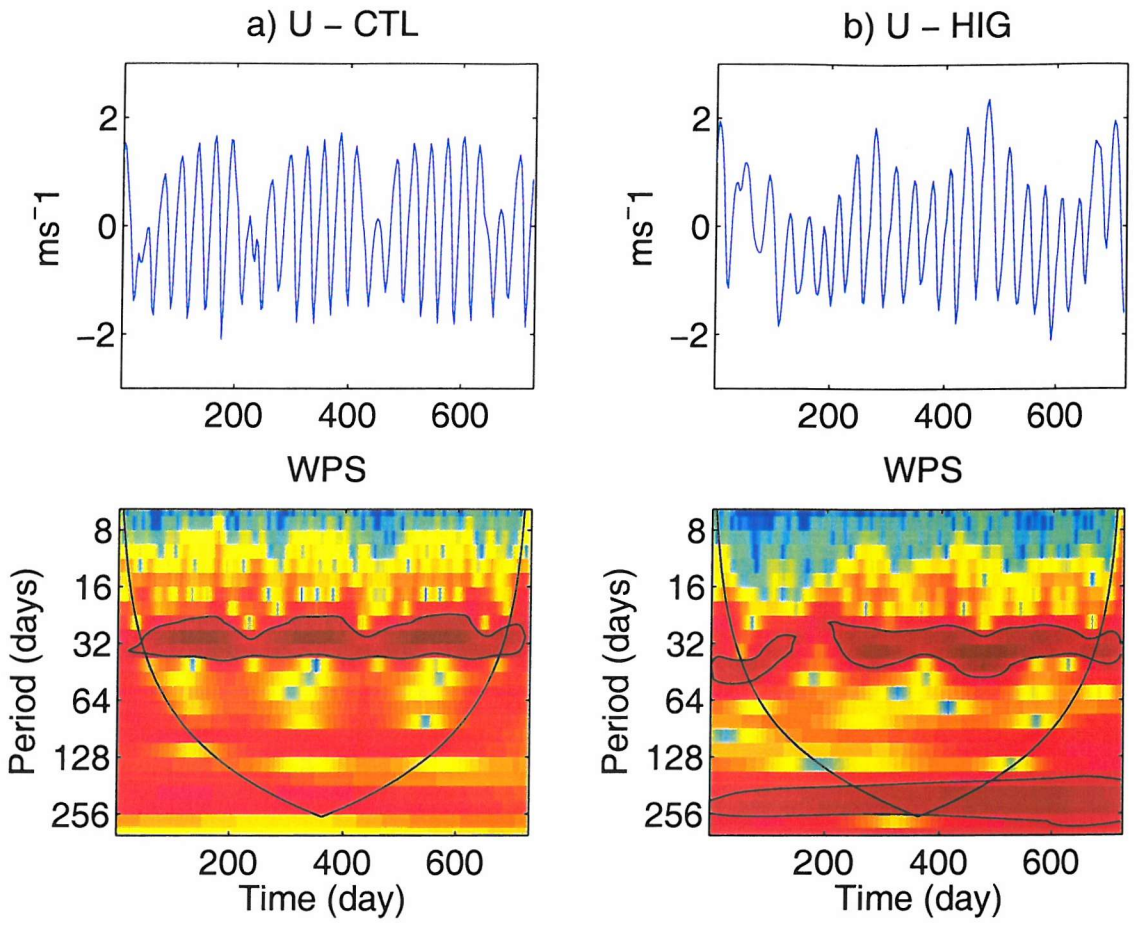

Figure 4.7: Zonal current time series (upper panels) and Wavelet Power Spectrum (WPS, lower panels) at Equator and 100°W for the a)- CTL and b)- HIG experiments. Currents are in m s^{-1}.

become important (Torrence and Compo, 1998). The CTL and HIG experiments clearly exhibits the TIWs characteristics propagating at this location with periods centered at 32 days, approximately. On the other hand, the HIG experiment also shows a lower frequency oscillation with periods around 230 days, approximately. These oscillations are propagating slower than TIWs and are more evident in the HIG zonal current. For instance, SST and meridional current do not show this lower frequency mode.

However, the TIW surface current speed is decreasing in magnitude when the coupling increases as shown in Figure 4.8 (left column) caused by the wind stress increasing (right column). This figure shows maps of zonal and meridional currents regressed onto the

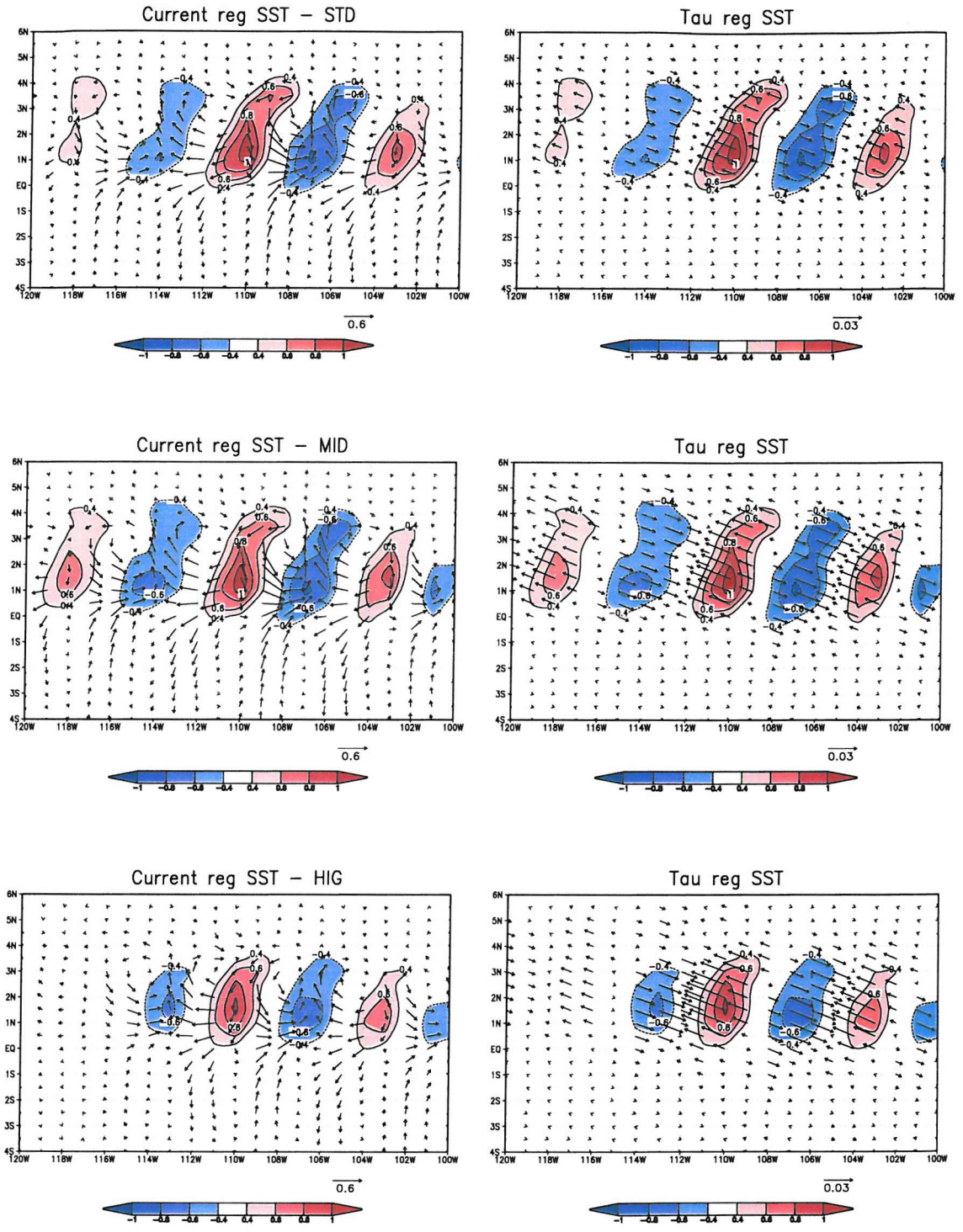

Figure 4.8: Regression map with center point at 110°W and 2°N. The arrows display currents regressed onto SST (m s^{-1} °C^{-1}) in the left column and surface wind stress regressed onto SST (N m^{-2} °C^{-1}) in the right column. SST auto-regression is displayed in shaded regions.

SST field with the center point at 110°W and 2°N (left column) and for wind stress (right column). The SST anomalies display a wave-train pattern largely confined between Equator and 4°N which are reduced in intensity and extension when the coupling is strengthened. The surface wind stress variability produced in the interactive experiments exhibits an increase in the variability. For instance, τ_x maximum variability is markedly increased by 75% (see Table 4.3) when the coupling coefficients are increased, comparing STD and HIG experiments. A similar increase is verified in τ_y wind component. The results suggest that surface wind stress is increased with the coupling strengthen as shown in Figure 4.8 and they are acting in an opposite manner reducing the current speed. This point will be further discussed when the wind stress action in producing kinetic energy is examined in Section 4.5.

Variable	STD	MID	HIG
τ_x	0.007	0.010	0.013
τ_y	0.003	0.004	0.005

Table 4.3: Maximum values of wind stress standard deviation for each coupled experiment along all longitudes and averaged over the latitudinal band extending from 5°S to 5°N.

Vertical structure

The meridional-depth variability is shown in Figure 4.9 and their maxima values are tabulated in Table 4.4. With regards to the vertical profile of temperature, two remarkable features are seen in this figure. One feature is in the upper part of the mixed layer, above 50 meters depth. The variability is clearly reduced when the coupling is increased. This result is consistent with the surface analysis presented in the previous section. The other feature is that, surprisingly, the larger variability values are localized in the lower thermocline region between 2°N and 4°N. For instance the variability in this region is maxima, reaching $0.85°C$ for the HIG experiment.

There are other interesting correspondences between ocean-atmosphere coupling and meridional-depth currents behavior. The zonal current component, mainly on the EUC region, is speeded up when the coupling is made stronger (see Table 4.2). In addition, it is noted a roughly linear increase in the zonal current variability by comparing the HIG experiment with the others performed under weaker ocean-atmosphere coupling coefficient,

Variable	T	u	v
CTL	0.83	0.24	0.22
STD	0.82	0.24	0.20
MID	0.78	0.25	0.19
HIG	0.85	0.27	0.19

Table 4.4: Maximum values of standard deviation zonally averaged over the region ranging from 150°W to 90°W. Maximums extracted from the meridional-depth Figure 4.9. Temperature is in °C and currents are in m s^{-1}

as shown in Figure 4.9 central column. Their maxima values are found at surface and in this case varying from 0.24 m s^{-1} for STD up to 0.27 m s^{-1} for HIG.

Comparing the results on the right column in Figure 4.9, we see that the meridional current exhibits an opposite behavior. The variability tends to decrease within the whole thermocline region when the coupling is increased, suggesting that TIW are less active. Again, in this current component the maxima are at the surface and it is 0.22 m s^{-1} for STD and is reduced to 0.19 m s^{-1} for the HIG experiment.

The dominant westward propagating speed (c_T) are calculated by Radon Transform (RT) technique (Challenor *et al.*, 2001) as used in Chapter 2. TIW imprints in the SST and the currents (both zonal and meridional components) tend to propagate with the same speed in the CTL experiment. The c_T is approximately 50 cm s^{-1} and agrees with other calculations found in the literature (Harvey and Patzert, 1976, Chelton *et al.*, 2001, Vialard *et al.*, 2003a,b).

Results from the interactive experiments suggest that the TIWs tend to speed up when the coupling is made stronger for the ocean TIW imprints, with c_T increasing up to 55 cm s^{-1}, approximately. The c_T calculated from the meridional current (v) is linearly increased as function of the ocean-atmosphere coupling strength. However, an exception is seen in the zonal current where c_T value is decreased with ABL interaction, comparing the CTL and STD experiments.

The 2-D Fourier analysis of the time-longitude data based on SST, current and τ data shows that TIW spectral characteristics are modified by the ocean-atmosphere interactions. Their period (Γ) ranges from 32 days up to 43 days and wavelength (λ) from 9° up to 11°.

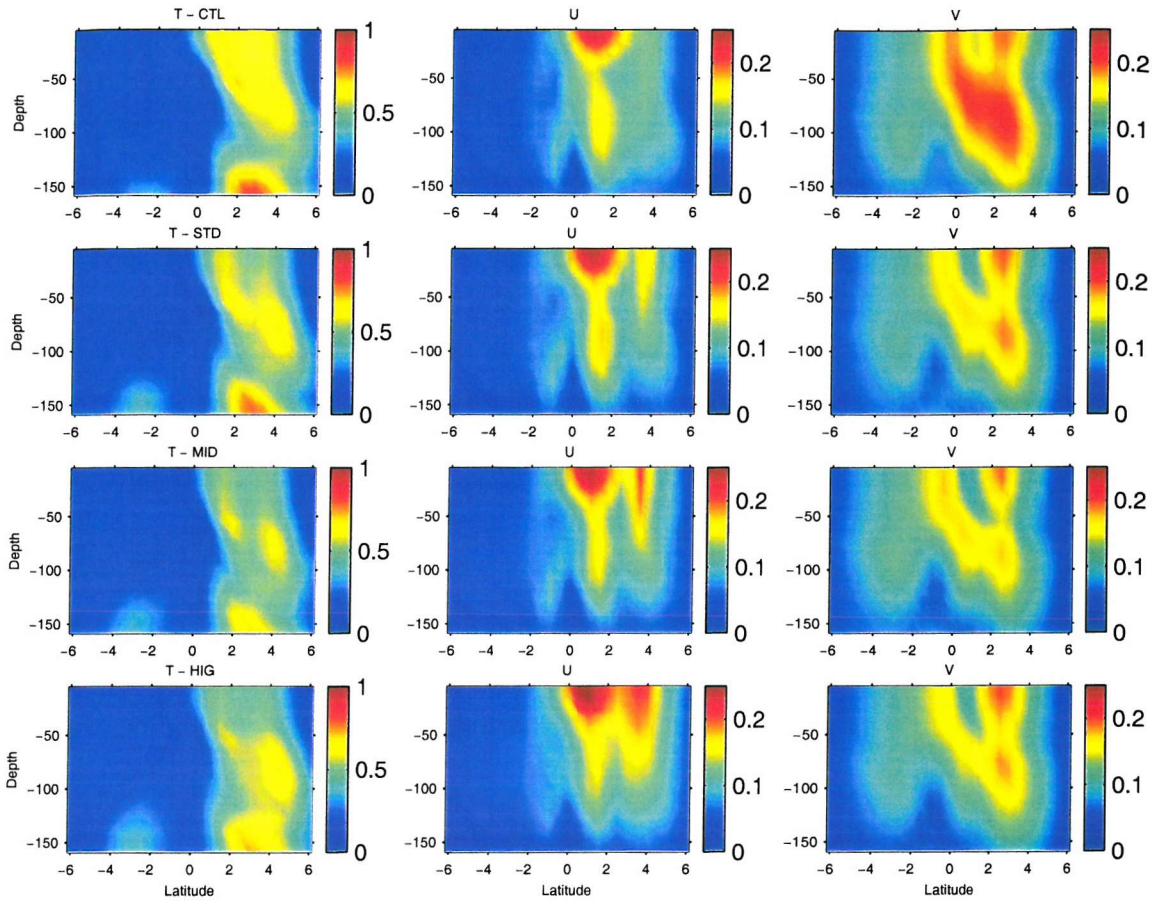

Figure 4.9: Standard deviation zonally averaged over the region ranging from 150°W to 90°W. Temperature on the left column, zonal current component (u) on the central column and meridional current component (v) on the right. Temperature is in °C and currents are in m s^{-1}

λ and Γ area increasing as function of the coupling strength.

4.4.4 Heat and momentum fluxes

The zonal momentum balances analyzed in Section 4.4.1 have shown that ocean-atmosphere coupling strength play an important role in the eastward equatorial flow simulation, which decreases the meridional momentum advection. Now we turn our attention to analyze the coupling strength impacts on the heat and momentum fluxes.

The co-variances $T'v'$, $T'u'$ and $u'v'$ are presented in Figure 4.10. The meridional heat

transport $T'v'$ in the TIW scale is directed towards the equator, since these waves mix warmer waters into the Cold Tongue region. This is evident in Figure 4.10 on the left side column; where a large and deep area with negative values is seen between Equator and 4°N region. The meridional heat flux is 38% decreased, approximately, when the coupling is made stronger and their minimum values are dropped down from -91 $\times 10^{-3}$ °C m^{2}s^{-2} to -57$\times 10^{-3}$ °C m^{2}s^{-2}. This reduction in $T'v'$ is consistent with the reduction in the T and v variability, shown in the previous section.

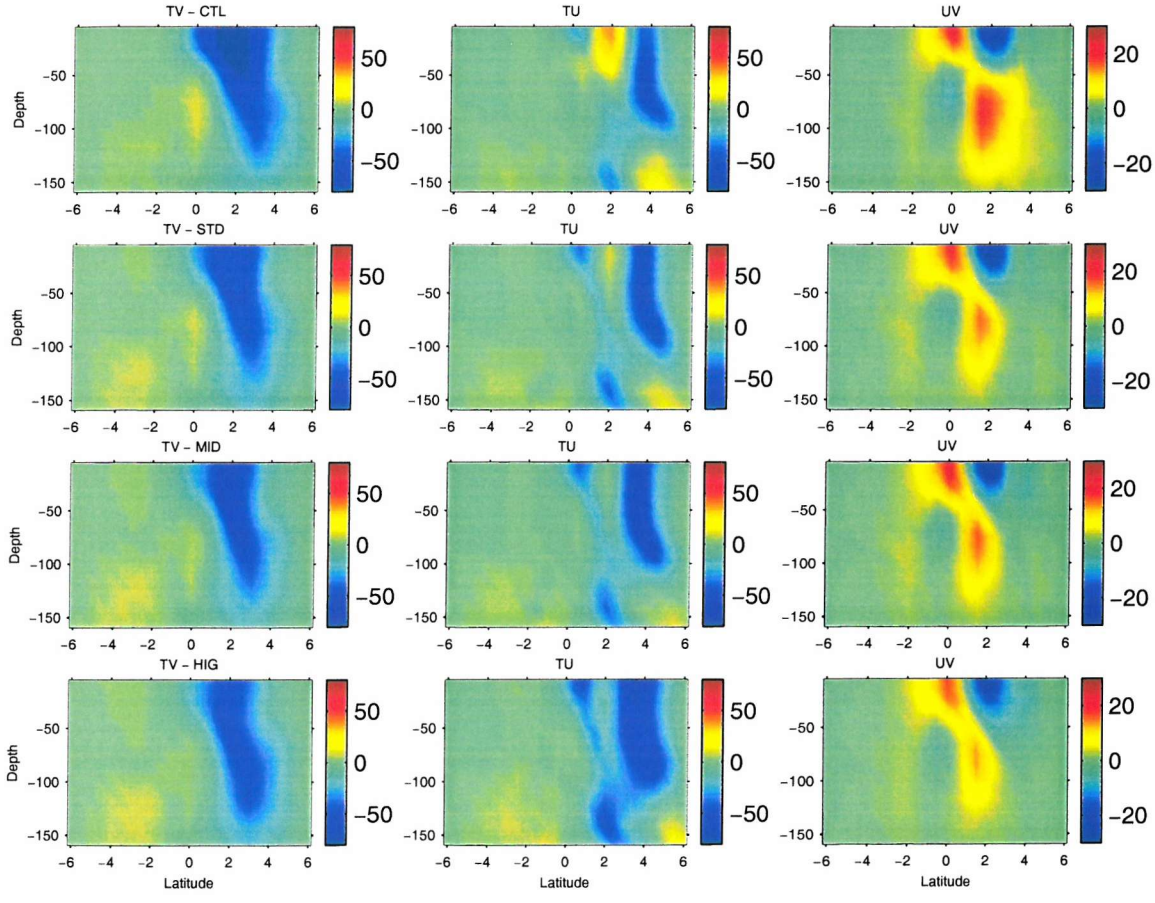

Figure 4.10: Fluxes zonally averaged over the region ranging from 150°W to 90°W. Meridional ($T'v'$) and Zonal eddy heat fluxes ($T'u'$) component. Reynolds stress component ($u'v'$). Units are 1$\times 10^{-3}$ °C m^{2}s^{-2} and 1$\times 10^{-3}$m^{2}s^{-2} respectively.

The momentum flux shown in Figure 4.10, suggests that the decreasing of divergence $u'v'$ at the Equator around 100 meters depth with increasing coupling is consistent with the increase in EUC speed given in Table 4.2 and the decrease in the convergence close to the surface (around 2°N) is consistent with the increase in the westward SEC shown by the

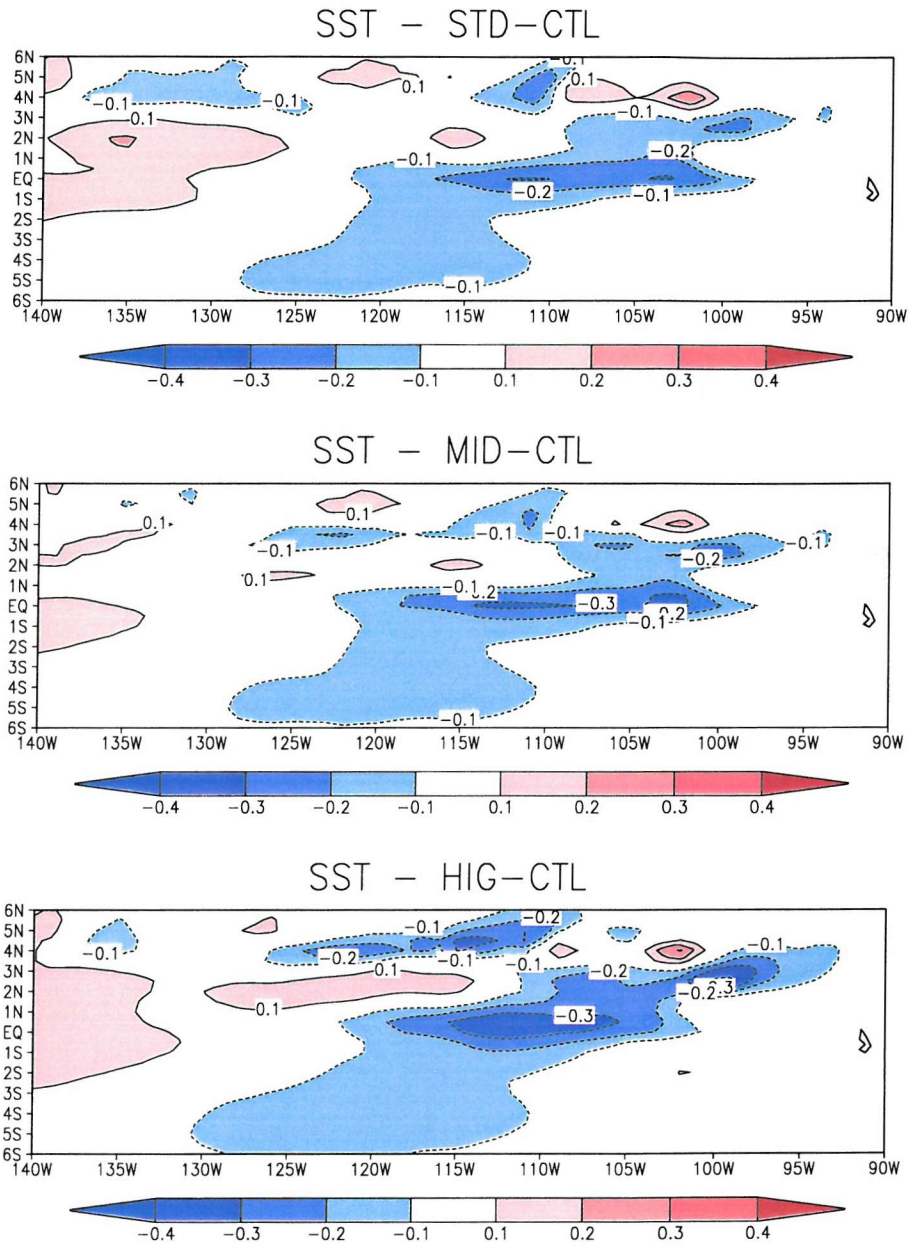

Figure 4.11: Differences of SST averaged over the last two year for the STD, MID and HIG experiments. The upper panel is CTL-STD, middle panel is CTL-MID and lower panel is CTL-HIG.

Variable	$T'v'$	$T'u'$	$u'v'$
CTL	-91	36	21
STD	-72	13	20
MID	-63	11	20
HIG	-57	16	17

Table 4.5: Minima and maxima values of the zonally averaged fluxes over the region ranging from 150°W to 90°W extracted from the meridional-depth Figure 4.10. Units are 1×10^{-3} °C m^2s^{-2} and $1\times10^{-3}m^2s^{-2}$ respectively.

maximum values in Table 4.2.

With regard to the temperature, the reduction in $v'T'$ would imply a cooling south of 3°N and a warming north of 3°N relative to the control run, i.e. the TIW are mixing less heat between the warm north and cooler equator. The SST at the equator indeed decreases as shown in the Figure 4.11 which shows the SST difference relative to the CTL experiment and all the others simulations in the equatorial region. However the upwelling, inferred from the horizontal divergence calculations at surface, is reduced when the coupling is increased. The results (figures not shown) reveal a reduction of 12% in equatorial upwelling comparing the STD experiment with CTL. The upwelling is even more reduced, 30 %, for the HIG experiment. These values are approximate and averaged over the area extending from 2°S to 2°N and from 160°W to 90°W.

The results suggest that TIW activity and upwelling are acting in opposite directions. The TIW activity decreasing tends to cool down the Cold Tongue region and the reduced upwelling to warm up. However, the temperature in this region is decreased suggesting that the TIW effects in transporting less meridional heat into the Cold Tongue region are apparently prevailing.

4.5 Energy rate flux

The ocean-atmosphere coupling strength modify the TIW characteristics as seen in previous sections. The total energy flux transferred into the ocean surface due to the wind action thereby generating kinetic energy is weakened with the coupling strengthening. The role of energy flux rate into the ocean surface associated with the coupling is investigated. We use

a similar approach to that used in Wunsch (1998) based on Stern (1975).

The rate at which energy is supplied to the ocean also commonly called as wind work at ocean surface (Wunsch, 1998) can be calculated as

$$\mathbf{w} = \langle \tau \cdot \mathbf{u} \rangle \tag{4.2}$$

where τ is the wind stress in both meridional and zonal directions (τ_x and τ_y respectively) and $\mathbf{u}$ is the vector representing the currents u and v. As shown in the Section 4.4.2 TIW have imprints in the atmospheric ABL, reinforcing Liu *et al.* (2000) and Hashizume *et al.* (2002) results. Also, TIWs are affected by the ABL feedbacks and here we want to isolate this TIW signal.

In order to analyze the work done by the TIWs we re-write the Equation 4.2 dividing $\mathbf{w}$ into a mean and a fluctuating part as follow

$$\mathbf{w} = \langle \overline{\tau} \cdot \overline{\mathbf{u}} \rangle + \langle \tau' \cdot \mathbf{u}' \rangle \tag{4.3}$$

where $\langle\rangle$ denotes average over two years, primed wind stress and currents are the high pass filtered fields using the same digital filter as used in Section 4.4.2. In Table 4.6 are tabulated the averaged values over the equatorial region ranging from 2°S to 6°N and from 130°W to 90°W for the components and total wind work.

Experiment	$\langle \tau_x u \rangle$	$\langle \tau_y v \rangle$	$\langle \tau'_x u' \rangle$	$\langle \tau'_y v \rangle$	Total
STD	10.3	2.0	0.2	-0.2	12.3
MID	9.7	1.9	0.5	-0.3	11.8
HIG	9.5	1.7	0.7	-0.3	11.6

Table 4.6: Wind flux energy on the ocean surface averaged over the region ranging from 2°S to 6°N and from 130°W to 90°W. All values are two years averaged and units are $\mu W m^{-2}$.

The tropical Pacific region is dominated by the strong westward wind stress in the trades region, approximately between 30°N and 30°S. Overall, the total rate of energy transferred

into the ocean within this region is decreased when the ocean-atmosphere coupling is increased. The mean zonal and meridional stress components are transferring energy into the ocean through the ocean-atmosphere coupling by analyzing the mean wind energy flux shown in Table 4.6. The eastward energy component ($\tau_x u$) represents a substantial part of the total input as can be seen by comparison with the total value and contributes with 82%, approximately, of the total rate of energy transferred into the ocean (Table 4.6) for the STD experiment. The ABL coupling enhancement produces an increase of the wind work maximum values, however, it is not reflected in the spatial average for the MID case as shown in Table 4.6. On the other hand, the mean northward wind work component is contributing with approximately 16% of the total energy rate. All the mean values are decreased when the coupling is increased.

The zonal component of the wind work over this same region but into TIWs spatio-time scales ($\langle \tau_x' u' \rangle$) shows a positive input of energy into the ocean which is increased as function of the coupling. This is a consequence of the τ_x increasing which can be inferred from Figure 4.8. The zonal wind work exhibits two positive areas located in the edges of the TIW activity region. In between these two positive areas there is a negative wind work region as consequence of the weak eastward component of the wind velocity (figure not shown).

The TIW meridional wind work component is acting in an opposite way to the zonal component, removing kinetic energy from the ocean. The $\langle \tau_y' v' \rangle$ values do not exhibit significant differences as the coupling increases, however, the coupling strength tends to decrease the negative values.

4.6 Summary and Conclusions

A series of coupled ocean-atmosphere experiments using different coupling strengths have been analyzed in this chapter. The coupled system uses a simplified ABL scheme, particularly with regards to the explicit physical representation of the boundary layer thermodynamics and dynamics.

The model results have suggested that there are significant effects of the ocean-ABL

coupling in the TIWs variability and characteristics. Despite the simplicity of the ABL scheme the integration using a standard coupling coefficient (STD) suggests that this system is able to accurately simulate the TIW atmospheric imprints. Both TIW magnitude and spatial feature imprints seen in the wind stress are comparable to those observational results shown in Liu *et al.* (2000) which have used high quality satellite data.

A major conclusion of our results is that active coupling strengthening produces a negative feedback on the TIWs. There are two main issues when the ocean-atmosphere coupling is strengthened. Firstly, the TIW activity tend to be reduced in both surface and sub-surface ocean. Secondly, the experiments using active wind interaction simulate a cooler Cold Tongue region with anomalous values reaching -0.3°C in some equatorial regions, when compared with the CTL.

Overall, less energy is being converted into ocean kinetic energy when coupling is increased as shown by both wind work and regression map analyzes. The meridional momentum and heat fluxes are largely decreased contributing to the Cold Tongue SST reduction.

There is an opposing action between the effects of the upwelling and the TIWs as the coupling strength is increased. On one hand, the reduction in the wind flux energy over the equatorial region decreases the cold water pumped up in the Cold Tongue (which would imply a warming). On the other hand, the decrease in the equatorward heat flux by the TIWs would imply a cooling of the water in this region. The effects of the TIWs are dominant in this scenario, mixing less warm water into the equatorial region and resulting a cooler Cold Tongue as a consequence. However, the mechanisms which fully explains the ABL effects in the TIWs characteristics need to be further investigated.

Experiments forced by a simplified ABL scheme would tend to make the results easier to interpret whilst still capturing the essential physics. However, this is not the case since there is no clear way to isolating one particular effect, e.g. only observing the TIWs effects in the system. Pushing the system in one way does not necessarily lead to the expected results. The simulation results suggest that we have a complex system of eddy and mean flow interactions.

Additionally, some important atmospheric processes might be missing or not explicitly being solved in the present model configuration, such as the atmospheric advection. As

suggested in Hayes *et al.* (1989) and recently demonstrated in Small *et al.* (2003), advection is thought to play a role in affecting wind stress and SST caused by the SLP differences.

Finally, the results found in this chapter must be seen as a first step in the investigation of the ABL feedbacks in the TIWs characteristics. It would be naive to believe that all the results obtained from the empirical ABL scheme coupled to an OGCM will reproduce the full ocean-atmosphere coupling processes. The robustness of the results from this simplified coupled scheme remains to be examined in a fully coupled ocean-atmosphere model. Ideally, the atmospheric model should have a grid resolution enough to capture the essential physics of TIWs atmospheric imprints and feedbacks, for example a regional atmospheric model.

Chapter 5

Conclusions

5.1 Final conclusions

The equatorial Pacific dynamics has been investigated in this project and a sizeable number of conclusions have been outlined in the preceding chapters. The strength and form of the lateral mixing parameterization of equatorial Pacific ocean are studied in Chapter 2, TIWs interannual variability in Chapter 3 and ocean-atmosphere TIW coupling feedbacks are investigated in Chapter 4. In this chapter we present a succinct reminder of what (most important) has (and has not) been achieved in this thesis. This will give an opportunity to reflect on some of the remaining problems and discuss how further progress might be made from the present findings.

5.1.1 Lateral mixing

Nowadays one of the major challenges in the simulation of the climate (past and future) lies in the proper representation of the oceanic component of the coupled ocean-atmosphere system. There is a number of limitations on numerical models which makes this a non trivial task. Among them there is the inability of the equations governing the dynamical system used in oceanic climate models to solve explicitly the subgrid-scale physics such as lateral mixing. Those small scale processes require a proper parameterization.

In Chapter 2, the lateral mixing strength and form are investigated. The equatorial

current strength is sensitive to the small-scale mixing, mixing tensor orientation and model grid resolution. SST can be changed by O(0.5°C) and the Equatorial Under Current speed by O(100%). TIWs play an important role in the heat balance of the Cold Tongue region, bringing heat in larger quantities when the eddy regime is more active. Both barotropic and baroclinic energy conversion terms are important in the waves generation. At low levels of mixing TIWs become more energetic and their behavior more irregular, with reduced seasonality.

A major conclusion from the results using a conventional constant value for the lateral mixing coefficient is that decreasing the mixing increases the Cold Tongue SST which in general is good because this reduces the cold bias but produces unrealistically strong currents. As an alternative solution to overcome this problem we propose a parameterization which enhances mixing close to the equator. It limits the strength of the EUC whilst little affecting the TIW activity and hence the cold tongue SST. The physical rationale we put forward for this enhanced mixing is the effect of the observed interleaving of water masses in producing a meridional flux of tracers and momentum (Richards and Banks, 2002, Richards and Edwards, 2003).

Usually the GCMs used for oceanic purposes are tuned to represent the observations and this is generally done just by choosing some lower mixing coefficients and setting up high grid resolutions to try to better solve the small scale physical processes. However the fine grid resolution itself, as showed by previous results in this study, increases the eddy activity, eddy heat transport and at the end it might not be the crucial factor needed to improve results. An alternative way to improve model results is study the physics represented by parameterizations. For example, exploring in more detail the question about the addition of mixing to represent the effect of interleaving as applied in this study and as previously raised by Richards (1998).

5.1.2 TIWs interannual variability

The TIWs interannual variability as a function of the large scale climate conditions are documented in Chapter 3. The total length of the satellite data record analyzed in this project is larger than the majority of TIWs satellite researches published up to this date.

Thus, it has allowed us to register and analyze the TIW characteristics through years when they were very actives and when they were not.

The TIWs clearly exhibit an interannual variability and dependence on the large scale climate conditions, such as ENSO phenomena. During La Niña years TIWs are distinctively more intense and on the average they have longer wavelengths. The numerical experiments using a channel-like geometry forced by stronger winds shown in Chapter 2 reinforce this idea.

The observational analysis is suggesting that ocean-atmosphere coupling mechanism occurs not only in La Niña years. We reinforce Wallace *et al.* (1989) theory which says that SST is coupled with wind through the ABL stability change. Our results also extend work by Liu *et al.* (2000) and Hashizume *et al.* (2001) where they have tested this hypothesis by analyzing just one TIW season during the second half of 1999, when a La Niña episode was established in the Pacific ocean. However, based on the dataset used here, it is not possible determine if the TIW-ABL coupling is the only (or the main) coupling mechanism which affects the low-level winds. Recently, Small *et al.* (2003), reinforcing Lindzen and Nigam (1987) previous findings, have suggested that advection plays a role in affecting SST gradients and wind stress caused by the SLP differences.

5.1.3 TIWs and ABL coupling

The ocean-atmosphere impacts on TIW oceanic characteristics are presented in Chapter 4. The results reveal that our empirical ABL scheme coupled to an OGCM is able to simulate the TIW and its atmospheric imprints, comparable to those shown in Liu *et al.* (2000). One of the most important results from these experiments is that ocean-atmosphere coupling produces a negative feedback on TIWs, reducing their activities and consequently modifying the equatorial characteristics. The model Cold Tongue is simulated cooler because the TIWs are less effective in mixing warmer waters in this region, even with reduced upwelling.

The temperature variations seen in the Cold Tongue region caused by the TIWs activity are significant since the climate over many world regions is sensitive to small SST changes. This fact brings about the discussion relative to the coupled models deficiency to simulate the Cold Tongue region accurately (Stockdale, 1992). Usually, atmospheric models used for

climate studies purposes do not fully represent TIWs imprints given their low grid resolution. Additionally, the ABL physical formulism often used in AGCM might not fully represent TIWs effects (Beljaars, *persn. comm.* 2003). The TIWs misrepresentation might be a contributing factor to the equatorial cold bias usually found in coupled ocean-atmosphere simulations.

5.2 Future directions

While the work undertaken in this project has addressed certain issues, there are many others outstanding. For instance, the sensitivity analysis of mixing parameterization and model grid resolution effects on mean state and TIWs need be taken further by some complementary studies.

Richards and Edwards (2003) suggest that inertial instability is the prime mechanism for the formation of the interleaving. In this case we expect the growth, and associated lateral fluxes of tracers and momentum, to be dependent on the lateral shear, and that the mixing is variable in both space and time. Our next step attempts to test the parameterization of additional lateral mixing and inertial instability as suggested by Richards and Edwards (2003). It is intended to implement both mixing schemes in collaboration with the team at LODYC in an ocean GCM with more realistic geometry and forcing.

By studying the sensitivity of the ABL simulation experiments and focusing their impacts on the TIW characteristics we note that there is still scope to further explore TIW interactions with the atmospheric boundary layer and their feedback mechanisms. This idea about ocean-ABL coupling should be re-visited, however, using a numerical boundary layer scheme which represents the surface fluxes as well as the surface wind shear. Specifically what is being suggested is to couple an OGCM to a 3-D regional atmospheric model. This scheme can provide the surface boundary conditions, such as the surface fluxes of momentum, heat and moisture to force the ocean model.

The fully 3-D coupled scheme would also include atmospheric advection effects in the simulation which would allow the determination of the nature of the interactions between the TIWs and the ABL. This will help to identify the major physical process involved in

affecting the wind stress as investigated in Small *et al.* (2003). Projects studying tropical Pacific climate, such as EPIC, would also benefit from any studies which help describe how the coupled ocean-atmosphere interaction affects the strength and spatial/temporal distribution of TIWs relating to the Cold Tongue maintenance and evolved dynamics. Also, it would be worth investigating the TIW direct/indirect impacts in the atmosphere, such as on the ITCZ as suggested in Xie *et al.* (1998) or in the cloud stratus deck which is formed over the eastern Pacific region and it is believed to be important for the radiative balance of the Cold Tongue.

Appendix A

OPA model

The numerical model used in the present study is the OGCM called OPA[1] which is an acronym for "Océan Parallélise", version 8.1. This model has been developed at "Laboratoire d'Océanographie Dynamique et de Climatologie" (LODYC), CNRS, University of Paris. A full description can be found in Madec *et al.* (1998), however some main characteristics are presented here. OPA was designed to be an easily configured tool for oceanic studies and its interactions with other components of the climate system i.e. atmosphere, sea-ice and biogeochemical tracers. This tool has been used in many fields of oceanographic and climatic researches e.g. Menkes *et al.* (1998), Vialard *et al.* (2003a,b), Lengaigne *et al.* (2003) and an extensive reference list with OPA applications can be found in Madec *et al.* (1998).

A.1 Tool

Modern numerical models are based on a formulation of the dynamical equations, referred as primitive equations, which is essentially based on the pioneering work by Bryan (1969) and after Cox (1984). The vertical coordinate is Z, which represents the vertical distance from a resting ocean surface at $Z = 0$, with positive upwards and $Z = -H(x, y)$ the topography. According with Griffies *et al.* (2000), some advantages of this coordinate is the simplicity of numerical discretization approach. On the other hand, this type of vertical coordinate

[1] OPA has a web site (http://www.lodyc.jussieu.fr/opa) from where can be downloaded the source code, manual, tracers model, visualization tools and publications.

is deficient on representing bottom topography. The primitive equations differ from the complete momentum equations where the vertical momentum equation is replaced by the hydrostatic approximation

A.1.1 Model description

The distribution of the variables is on a three dimensional Arakawa C (Mesinger and Arakawa, 1976) type staggered grid, as shown in Figure A.1 for the horizontal mesh and Figure A.2 for the vertical mesh. All experiments are configured using prescribed 31 Z-levels, which are shown in Table B.1.

This grid arrangement is optimal in reducing phase speed errors in oceanic waves provided that the grid spacing is less than appropriate Rossby radius (Mesinger and Arakawa, 1976). The OPA solves primitive equations following Bryan(1969) as referred in Madec *et al.* (1998) with a large variety of physical options. The prognostic variables are the three dimensional velocity fields and the thermohaline variables.

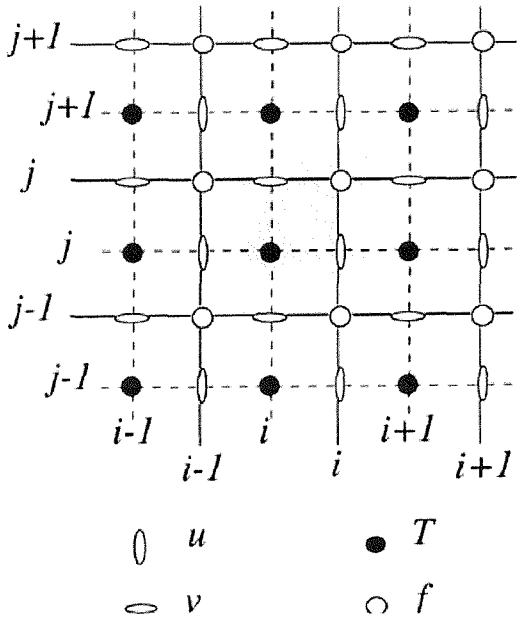

Figure A.1: Horizontal integer indexation used in the model code. The dashed area indicates the cell in which variables contained in arrays have the same i- and/or j-indices. Source Madec *et al.* (1998).

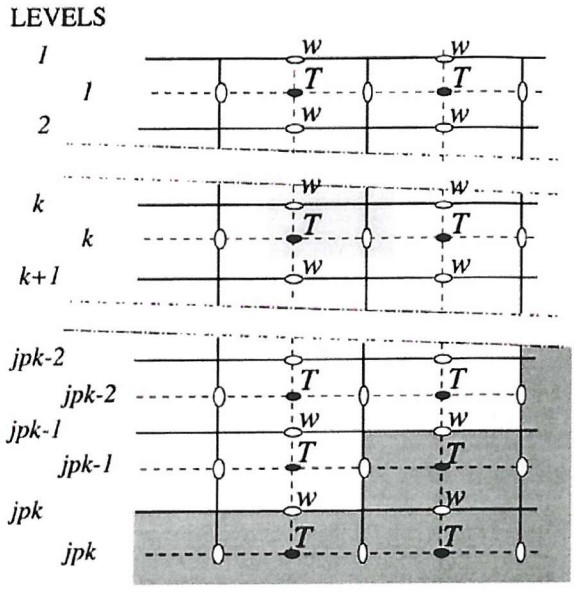

Figure A.2: Vertical integer indexation used in the model code. The dashed area indicates the cell in which variables contained in arrays have the same k-indices. Note that the k-axis is oriented downward. Source Madec *et al.* (1998).

The momentum equation expresses the conservation of horizontal momentum,

$$\frac{\partial \mathbf{U_h}}{\delta t} = [(\nabla \times \mathbf{U}) \times \mathbf{U} + \frac{1}{2}\nabla(\mathbf{U^2})]_h - f\mathbf{k} \times \mathbf{U_h} - \frac{1}{\rho_0}\nabla_h p + \mathbf{D^u} \tag{A.1}$$

where $\mathbf{U}$ is the velocity vector and $\mathbf{U} = \mathbf{U_h} + w\mathbf{k}$ (the h subscript denotes horizontal vector), ρ_0 is a reference density, p the pressure, f is the Coriolis parameter ($f = 2\Omega \cdot \mathbf{k}$, where Ω is the Earth angular velocity), t time and $\mathbf{D^u}$ is the parameterization of small scale physics for momentum.

From the hydrostatic equation is computed the pressure;

$$\frac{\partial p}{\partial z} = -\rho g \tag{A.2}$$

where ρ is in situ density given by the equation of state (Equation A.6) and g is the gravity acceleration.

The assumption of incompressibility allows the computation of the vertical velocity w;

$$\nabla \cdot \mathbf{U} = 0 \tag{A.3}$$

The heat Equation A.4 and salt Equation A.5 conservation are calculated as follows

$$\frac{\partial T}{\partial t} = -\nabla \cdot (T\mathbf{U}) + \mathbf{D^T} \tag{A.4}$$

$$\frac{\partial S}{\partial t} = -\nabla \cdot (S\mathbf{U}) + \mathbf{D^S} \tag{A.5}$$

where T is the potential temperature, S salinity, $\mathbf{D^T}$ and $\mathbf{D^S}$ are the parameterizations of small scale physics for temperature and salinity respectively.

Pressure, temperature and salinity are combined together in the equation of state Equation A.6 in order to compute the density,

$$\rho = \rho(T, S, p) \tag{A.6}$$

The leapfrog, three-level centered, is the time differencing scheme used in OPA for non-diffusive process. The first time step of this three level scheme when starting from an ocean at rest is a forward step. The numerical techniques used to solve the primitive equations are based on the centered second order finite difference approximation and a full description with all model formulations can be found in Madec *et al.* (1998). OPA is portable for different kinds of machines using UNIX as an operational system and can be set up to run either in super-computers or workstations.

The results presented in Chapter 2, OPA has been used in a Silicon Graphics (Origin 2000) workstation, based at Southampton Oceanographic Centre (SOC). The experiments presented in Chapter 4 were performed at LODYC using a NEC-SX5 super-computer facilities at IDRIS (Institute for Development and Resources in Intensive Scientific computing) [2] The model has been written on standard Fortran 77 with some additional routines on Fortran 90.

A.1.2 Parameterizations

Wind forcing

The wind stress τ used to drive the model dynamically is all put into the top layer and the wind forcing strategy has been previously described in Chapters 2 and 4.

[2]IDRIS is a CNRS's national supercomputing center at France. http://www.idris.fr

Heat Flux

Heat flux into the surface layer is prescribed by relaxation towards some climatological value. Specifically, the net heat flux parameterization at the ocean surface is given by the following equation,

$$Q(SST_{mod}) = Q(SST_{obs}) + \frac{\delta(Q)}{\delta(SST)}(SST_{mod} - SST_{obs}) \tag{A.7}$$

where, Q is the net heat flux at the ocean-atmosphere interface, SST_{obs} is the climatological Levitus and Boyer (1994) SST zonally averaged monthly varying (for the experiments carried out in Chapter 2. For the experiments in the Chapter 4 the SST_{obs} is not zonally averaged but is perpetual October. The SST_{mod} is the surface temperature simulated by the model. $Q(SST_{obs})$ is the non penetrative part of the surface heat flux.

According to Barnett *et al.* (1991) the Equation A.7 is surprisingly good representing the interannual varying net heat flux. In our experiments $\frac{\delta(Q)}{\delta(SST)}$ is kept constant -40 $Wm^{-2}K^{-1}$ everywhere. This value is considerable high when compared with Barnett *et al.* (1991). However when lower values were tested the SST simulated is degraded. This result agrees with Vialard *et al.* (2003a) findings. There is no restoring towards observed sea surface salinity (SSS).

Lateral Mixing

The effects of smaller scale motions coming from the advective terms in the Navier-Stokes equations must be represent entirely in terms of large scale patterns to close the equations. Assuming a turbulent closure hypothesis is equivalent to chose a formulation for these fluxes.

OPA vertical eddy viscosity and diffusivity are calculated from a turbulence closure scheme which allows higher values at the surface and minimums of 1×10^{-5} m^2s^{-1} in the thermocline as shown by Blanke and Delecluse (1993). It is worth emphasize that turbulent closure is a weak point in model simulations and at the same time extremely important since such small-scale fluxes have large impacts in the mean fields representations, heat and momentum balances (Banks, 1997, Maes *et al.*, 1997, Lengaigne *et al.*, 2003).

The subgrid-scale $\mathbf{D^u}$, $\mathbf{D^T}$ and $\mathbf{D^S}$ from Equations A.1, A.4 and A.5 are split into a lateral (often called horizontal) component and a vertical component, such as

$$\mathbf{D^u} = \mathbf{D^{lu}} + \mathbf{D^{vu}}$$

where $\mathbf{D^{lu}}$ is the lateral component and $\mathbf{D^{vu}}$ is the vertical.

The lateral eddy mixing formulation in an OGCM depends on whether the mesoscale phenomenon is above or below the gridspacing used in such model. In non-eddy resolving models (commonly used for climate studies) the closure schemes used to solve the lateral mixing usually is similar to the vertical physics. The lateral turbulent fluxes are assumed to depend linearly on the lateral gradients of large scale quantities.

The slope of isopycnal oceanic surfaces is small, as a result a common approximation is to assume that 'lateral' direction is horizontal; i.e. the mixing is performed along geopotential surfaces. This leads to a geopotential second order operator for horizontal subgrid physics. Similar approach is taken when the lateral mixing is assumed to occur along isopycnal surfaces. Lengaigne *et al.* (2003) have suggested that mixing induced by turbulent processes are better represented by numerical models along these surfaces. In such case, the isopycnal second order operator is used. The lateral second order tracer diffusive operator is

$$D^{lT} = \nabla(A^{lT}\kappa\nabla T) \tag{A.8}$$

were T represents temperature in this case, but it can be also either horizontal velocity or salinity. ∇ is the three dimensional gradient operator and κ

$$\kappa = \begin{Bmatrix} 1 & 0 & -r_1 \\ 0 & 1 & -r_2 \\ -r_1 & -r_2 & r_1^2 + r_2^2 \end{Bmatrix}$$

where r_1 and r_2 are the slopes between the surface along which the diffusive operator acts and the surface computation (z- or s-surfaces). More comprehensive description about the formulation and lateral mixing implementations in OPA are given in Madec *et al.* (1998), Maes *et al.* (1997), Lengaigne *et al.* (2003).

Vertical sub-grid scale physics

Turbulent motions are never explicitly solved in OGCM, even partially. They are parameterized because the model resolution is always larger than the scale at which major source of vertical turbulence occurs (shear instability, internal wave breaking, ...). The vertical turbulent fluxes are assumed to depend linearly on the gradients of large scales quantities. For example, the turbulent heat flux is obtained by $\overline{T'w'} = -A_v \partial_z \overline{T}$, where A_v is an vertical eddy coefficient. The resulting vertical momentum and tracer diffusive operators are of second order:

$$\mathbf{D^{vU}} = \frac{\partial}{\partial z}\left(A_{vm}\frac{\partial \mathbf{U_h}}{\partial z}\right), \quad \mathbf{D^{vT}} = \frac{\partial}{\partial z}\left(A_{vT}\frac{\partial T}{\partial z}\right), \quad \mathbf{D^{vS}} = \frac{\partial}{\partial z}\left(A_{vS}\frac{\partial S}{\partial z}\right) \tag{A.9}$$

where A_{vm} and A_{vT} are the vertical eddy viscosity and diffusivity coefficients, respectively. In OPA model, the vertical eddy coefficients can be taken as constant values, or as function of the Richardson number or from an 1.5 turbulent closure model. We choose the former option to use in all experiments performed in this project. Details of the 1.5 turbulent closure model can be seen in Blanke and Delecluse (1993) and Madec *et al.* (1998).

Appendix B

OPA Implementations

The numerical model used in the present study has been adapted from an original version but keeping similar configurations throughout the chapters. However, the variety of experiments performed have used different model grid configuration. In this Appendix are presented the model grid resolution and configuration used in Chapters 2 and 4.

B.1 Horizontal grid

The coarse model grid resolution used in Chapter 2 is shown in Figure B.1. It has fixed zonal resolution except on the westernmost where the resolution is increased to better resolve the equatorial current system and the western boundary currents. The zonal grid spacing is 1/2° at the western boundary increasing to 1° by 10° of longitude, remaining with this grid spacing over the rest of model domain.

The latitudinal grid spacing is reduced near the equator. For the coarser grid resolution experiments in Chapters 2 and 4, the grid spacing in meridional direction is 1/2° between 5°S and 5°N, increasing to 2° by 10°S (10°N).

The fine grid resolution version used in Chapter 2 (Figure B.2) has 1/4° in the zonal direction covering all the domain and in the meridional direction it has 1/4° within the equatorial region extending from 5°S to 5°N increasing to 1° towards the northern and southern boundaries.

In Chapter 4 coastlines resembling the tropical Pacific ocean shape are introduced on the model domain configuration (B.3). Also, the longitudinal resolution is kept constant with 1° grid spacing as shown in Figure B.4.

B.2 Vertical grid

There are 31 levels on the vertical coordinate. The highest resolution, approximately 10 meters, is on the top 150 meters. Below this depth the resolution decreases down to 500 meters near the ocean bottom at 5000 meters depth. This vertical resolution is used in both Chapters 2 and 4.

Levels	T	W
1	5.00	0.00
2	15.00	10.00
3	25.00	20.00
4	35.01	30.00
5	45.01	40.01
6	55.03	50.02
7	65.06	60.04
8	75.13	70.09
9	85.25	80.18
10	95.49	90.35
11	105.97	100.69
12	116.90	111.36
13	128.70	122.65
14	142.20	135.16
15	158.96	150.03
16	181.96	169.42
17	216.65	197.37
18	272.48	241.13
19	364.30	312.74
20	511.53	429.72
21	732.20	611.89
22	1033.22	872.87
23	1405.70	1211.59
24	1830.89	1612.98
25	2289.77	2057.13
26	2768.24	2527.22
27	3257.48	3011.90
28	3752.44	3504.46
29	4250.40	4001.16
30	4749.91	4500.02
31	5250.23	5000.00

Table B.1: Default vertical mesh in z-coordinates, used in all experiments. Units are meters.

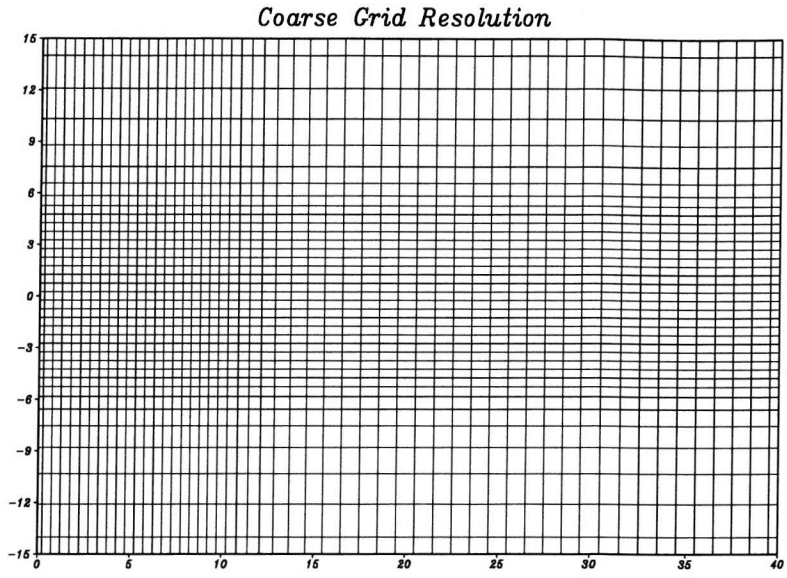

Figure B.1: OPA ocean GCM coarse grid model resolution. The grid resolution is increased on the westernmost region and within equatorial region. Note that it is only showed the western part of the domain.

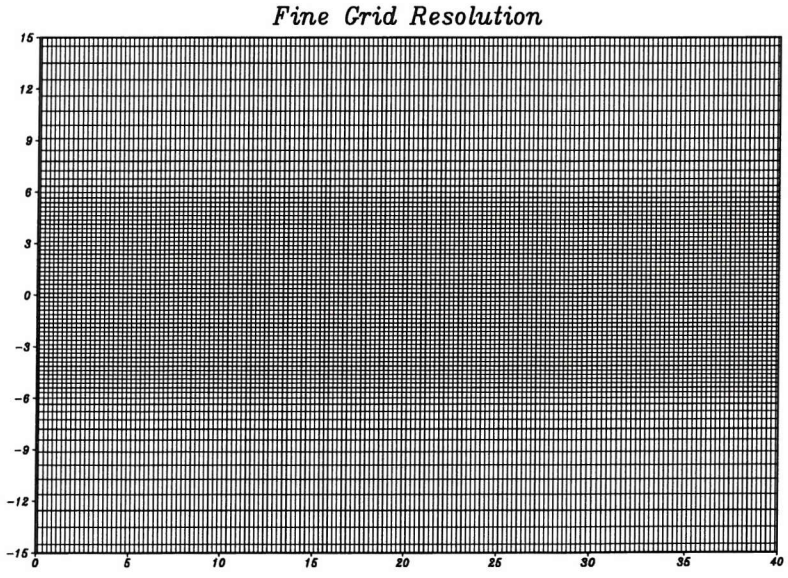

Figure B.2: OPA ocean GCM fine grid model resolution. The grid resolution is 1/4° equally spaced along the longitudes and it increases within equatorial region. Note that it is only showed the western part of the domain.

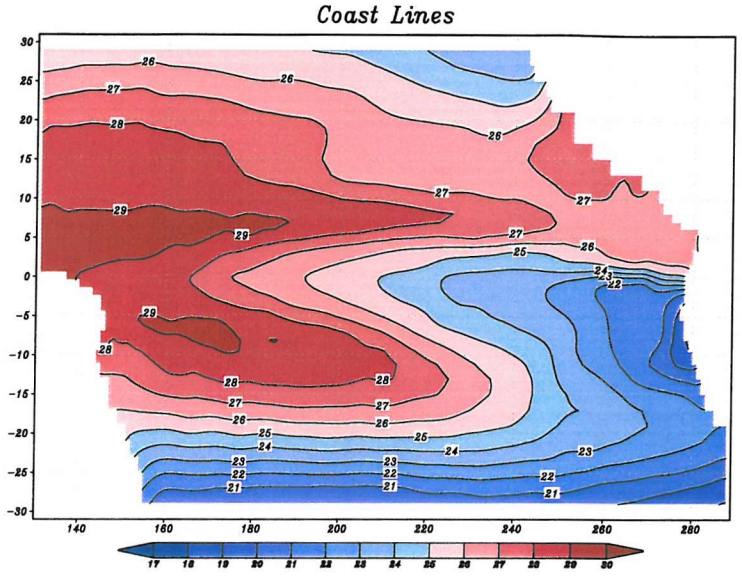

Figure B.3: OPA ocean GCM coastlines used in Chapter 4 coupled experiments. SST of the CTL experiment

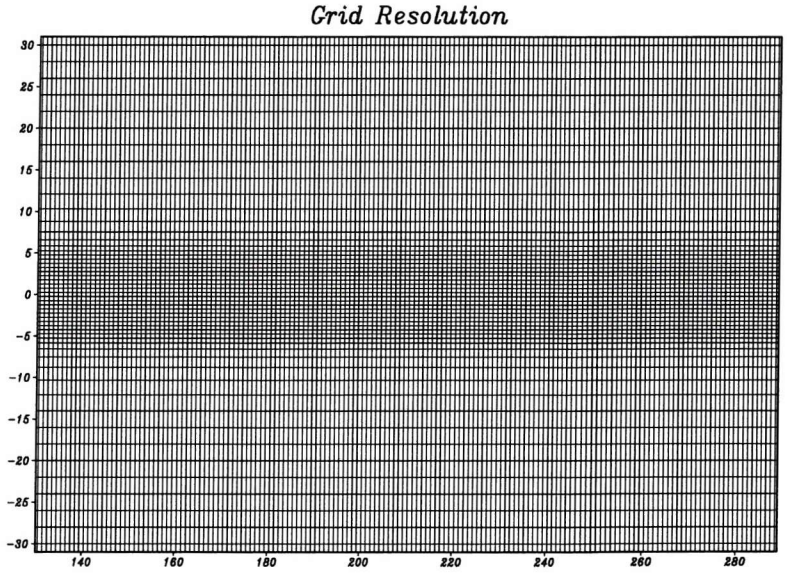

Figure B.4: OPA ocean GCM grid model resolution used in Chapter 4 coupled experiments.

Appendix C

Momentum equation zonal balance

The zonal momentum equation analyzed in Chapter 4 is expressed as

$$\frac{du}{dt} = -\frac{1}{\rho}\frac{dP}{dx} - u\frac{du}{dx} - v\frac{du}{dy} - w\frac{du}{dz} + fv + D_u^l + D_u^v \tag{C.1}$$

where the u, v and w are the velocity components, f is the Coriolis parameter that vanishes at the Equator, ρ the reference density, D_u^l is the lateral diffusive operator and D_u^v is the vertical diffusive operator. On the right hand side of Equation C.1 are considered the tendencies that drive the local acceleration of the zonal current. The first term on the right hand side $-\frac{1}{\rho}\frac{dP}{dx}$ is the zonal pressure gradient (ZPGR), the second term is the contribution by zonal advection (ZADV), third is the meridional advection (MADV) and the fourth term is the vertical advection (VADV). The sixth (D_u^l) and seventh (D_u^v) terms are the physical parameterization of horizontal (LDIF) and vertical (VDIF) momentum transfer. The vertical diffusion is expressed by two terms

$$D_u^v = \frac{d}{dz}(\frac{dK}{dz}\frac{du}{dz}) + \frac{d}{dz}(\frac{\tau_x}{\rho})$$

where $\frac{d}{dz}(\frac{dK}{dz}\frac{du}{dz})$ is the vertical mixing tendency term and $\frac{d}{dz}(\frac{\tau_x}{\rho})$ represents the zonal wind stress τ_x contribution to the vertical mixing tendency at the surface. This last term vanishes in other levels.

Bibliography

Allen, M. R., S. P. Lawrence, M. J. Murray, C. T. Mutlow, T. N. Stockdale, D. T. Llewellyn-Jones, and D. L. T. Anderson, 1995. Control of Tropical Insatbility Waves in the Pacific. *Geophysical Research Letters*, 22(19):2581–2584.

Banks, T. H., 1997. *Intrusions and mixing in the Western Equatorial Pacific.* Ph.D. thesis, University of Southampton.

Barnett, T. P., M. Latif, M. Kirk, and E. Roeckner, 1991. On ENSO physics. *Journal of Climate*, 4:487–514.

Barnston, A. G. and Y. He, 1996. Skill of Canonical Correlation Analysis Forecasts of 3-Month Mean Surface Climate in Hawaii and Alaska. *Journal of Climate*, 9:2579–2605.

Barnston, A. G. and R. Preisendorfer, 1987. Origins and Levels of Monthly and Seasonal Forecast Skill for United States surface air temperatures determined by Canonical Correlation Analysis. *Monthly Weather Review*, 115:1825–1850.

Baturin, N. G. and P. P. Niiler, 1997. Effects of Instability Waves in the Mixed Layer of the Equatorial Pacific. *Journal of Geophysical Research*, 102:27771–27793.

Benestad, R. E., R. T. Sutton, M. R. Allen, and D. L. T. Anderson, 2001. The influence of subseasonal wind varability on Tropical Instability Waves in the Pacific. *Geophysical Research Letters*, 28:2041–2044.

Blanke, B. and P. Delecluse, 1993. Variability of the Tropical Atlantic ocean simulated by a general circulation model with two different mixed layer physics. *Journal of Physical Oceanography*, 23:1363–1388.

Brentnall, S. J., 1999. *The Impact of Galapago Islands on the Dynamics of the Equatorial East Pacific.* Monography, School of Ocean and Earth Sciences - University of Sothampton, Eropean Way - Southampton - UK.

Bryan, K., 1969. A numerical method for the study of the circulation of the world ocean. *Journal of Computacional Physics*, 4:347–376.

Bryden, H. L. and E. C. Brady, 1989. Eddy Momentum and Heat Fluxes and their effects on the circulation of the Eqautorial Pacific Ocean. *Journal of Marine Research*, 47:55–79.

Challenor, P. G., P. Cipollini, and Cromwell, 2001. Use of the 3D Radon Transform to Examine the Properties of Oceanic Rossby Waves. *Journal of Atmospheric and Oceanic Technology*, 18:1558–1566.

Chelton, D. B., S. K. Esbensen, M. G. Schlax, N. Thun, M. Freilich, F. J. Wentz, C. L. Gentmann, M. J. McPhaden, and P. S. Schopf, 2001. Observations of coupling between surface wind stress and sea surface temperature in the eastern tropical pacific. *Journal of Climate*, 14:1479–1498.

Chelton, D. B., F. J. Wentz, C. L. Gentemann, R. A. Szoeke, and M. G. Schlax, 2000. Satellite Microwave SST Observations of Transequatorial Tropical Instability Waves. *Geophysical Research Letters*, 27(9):1239–1242.

Cipollini, P., D. Cromwell, P. G. Challenor, and S. Raffaglio, 2001. Rossby waves detected in global ocean colour data. *Geophysical Research Letters*, 28(2):323–326.

Cipollini, P., D. Cromwell, M. S. Jones, G. D. Quartly, P. G. Challenor, and S. Raffaglio, 1997. Concurrent altimeter and infrared observations of Rossby wave propagation near 34 °N in the northeast Atlantic. *Geophysical Research Letters*, 24:889–892.

Contreras, R. F., 2002. Long-Term observations of Tropical Instability Waves. *Journal of Physical Oceanography*, 32:2715–2722.

Cox, M. D., 1984. A primitive equation, 3-dimensional model of the ocean. *GFDL, Ocean Group Technical Report 1, Available from Geophysical Fluid Dynamics Laboratory, Princeton New Jersey - USA.*

Cromwell, D., 2001. Zonal propagation of Energy at 34°N in the North Atlantic: a wavelet analysis. *Geophysical Research Letters*, 28(19):3705–3708.

Delecluse, P., 1994. *Long-term climatic variations: data and modelling*, chap. Modelling the Ocean Circulation, pages 73–106. Nato Series. ed. J.C. Duplessy and M.T. Spyridakis.

Duing, W., P. Hisard, E. Katz, J. Meincke, K. Miller, K. V. Moroshkin, P. J., A. A. Ribnikov, K. Voigt, and R. Weisberg, 1975. Meanders and long waves in the equatorial Atlantic. *Nature*, 257:280–284.

Firing, E., R. Lukas, J. Sadler, and K. Wyrtki, 1983. Equatorial Undercurrent disappears during 1982-1983 El Niño. *Science*, 222:1121–1123.

Flament, P. J., S. C. Kennan, R. A. Knox, P. P. Niiler, and R. L. Bernstein, 1996. The Three-Dimensional structure of an upper Ocean Vortex in the Tropical Pacific Ocean. *Nature*, 383:610–613.

Folland, C. K., T. N. Palmer, and D. E. Parker, 1986. Sahel rainfall and world-wide sea temperatures 1901-85. *Nature*, 320:602–607.

Garrett, C., 2003. Mixing with Latitude. *Nature*, 422:477–478.

Griffies, S. M., K. Boning, F. O. Bryan, E. P. Chassignet, G. R., H. Hasumi, A. Hirst, A. M. Treguier, and D. Webb, 2000. Developments in ocean climate modelling. *Ocean Modelling*, 2:123–192.

Gu, D. and S. G. H. Philander, 1995. Secular changes of annual and interannual variability in the tropics during the past century. *Journal of Climate*, 8:864–876.

Guilyardi, E., G. Madec, and L. Terray, 2001. The role of the lateral ocean physics in the upper ocean thermal balance of a coupled ocean-atmosphere GCM. *Climate Dynamics*, 13:149–165.

Halpern, D., R. A. Knox, and D. S. Luther, 1988. Observations of 20-day period meridional current oscillations in the upper ocean along the Pacific equator. *Journal of Physical Oceanography*, 18:1514–1534.

Hansen, D. V. and C. A. Paul, 1984. Genesis and effects of long waves of long waves in the equatorial Pacific. *Journal of Geophysical Research*, 89:10431–10440.

Harrison, D. E., R. D. Romea, and G. A. Vecchi, 2001. Central equatorial Pacific zonal currents. I: The Sverdrup balance, nonlinearity and tropical instability waves. *Journal of Marine Research*, 59:895–919.

Harvey, R. R. and W. C. Patzert, 1976. Deep current measurememnts suggest long waves in the eastern equatorial Pacific. *Science*, 193:883–884.

Hashizume, H., S. P. Xie, M. Fujiwara, M. Shiotani, T. Watanabe, Y. Tanimoto, W. T. Liu, and K. Takeuchi, 2002. Direct observations of atmospheric boundary layer response to SST variations associated with Tropical Instability waves over the eastern equatorial Pacific. *Journal of Climate*, 15:3379–3393.

Hashizume, H., S. P. Xie, W. T. Liu, and K. Takeuchi, 2001. Local and Remote Atmospheric Response to Tropical Insatbility waves: A Global View from the Space. *Journal of Geophysical Research*, 106(D10):10173–10185.

Hastenrath, S., 1982. On Meridional Heat Transports in the World Ocean. *Journal of Physical Oceanography*, 12:922–927.

Hayes, S. P., M. J. McPhaden, and J. M. Wallace, 1989. The Influence of Sea Surface Temperature on Surface Wind in the Eastern Equatorial Pacific: Weekly to Monthly Variability. *Journal of Climate*, 2:1500–1506.

Hellerman, S. and M. Rosenstein, 1983. Normal Monthly Wind Stress over the World Ocean with Error Estimates. *Journal of Physical Oceanography*, 13:1093–1104.

Kelly, K. A., M. J. Dickinson, M. J. McPhaden, and G. C. Johnson, 2001. Ocean currents evident is satellite wind data. *Geophysical Research Letters*, 28:2469–2472.

Kennan, S. C. and P. J. Flament, 2000. Observations of a Tropical Insatbility Vortex. *Journal of Physical Oceanography*, 30:2277–2301.

Killworth, P. D., P. Cipollini, B. M. Uz, and J. R. Blundell, 2003. Physical and biological mechanisms for planetary waves observed in sea-suface chlorophyl. *Journal of Geophysical Research*, Submitted.

Large, W. G., G. Danabasoglu, J. C. McWilliams, P. R. Gent, and F. O. Bryan, 2001. Equatorial circulation of a global ocean climate model with anisotropic horizontal viscosity. *Journal of Physical Oceanography*, 31:518–536.

Lawrence, S. P., M. R. Allen, D. L. T. Anderson, and D. T. Llewellyn-Jones, 1998. Effects of subsurface ocean dynamics on instability waves in tropical Pacific. *Journal of Geophysical Research*, 103:18649–18663.

Legeckis, R., 1977. Long Waves in the Eastern Equatorial Pacific Ocean: A View from a Geostationary Sattelite. *Science*, 197:1179–1181.

Lengaigne, M., G. Madec, C. Menkes, A. Jouzeau, and G. Alory, 2003. Impact of Isopycnal Mixing on the Tropical Ocean Circulation. *submitted to Journal of Geophysical Research.*

Levitus, S. and T. Boyer, 1994. World Ocean Atlas 1994. Tech. Report. (Salinity and Temperature) Vol 3-4, US Dep. of Commer., Washington, DC.

Lindzen, R. S. and S. Nigam, 1987. On the role of Sea Surface Temperature gradients in forcing low-level winds and convergence in the tropics. *Journal of the Atmospheric Sciences*, 44(17):2418–2436.

Liu, W., X. Xie, P. S. Polito, S. P. Xie, and H. Hashizume, 2000. Atmospheric Manifestation of Tropical Instability Wave Observed by QuickSCAT and Tropical Rain Measuring Mission. *Geophysical Research Letters*, 27(16):2545–2548.

Luther, D. S. and E. S. Johnson, 1990. Eddy energetics in the upper Equatorial Pacific during Hawaii-to-Tahiti Shuttle Experiment. *Journal of Physical Oceanography*, 20:913–944.

Ma, C. C., C. R. Mechoso, A. W. Robertson, and A. Arakawa, 1996. Peruvian stratocumulus clouds and the tropical Pacific circulation – a coupled ocean atmosphere GCM study. *Journal of Climate*, pages 1635–1645.

Madec, G., P. Delecluse, M. Imbard, and C. Lvy, 1998. OPA8.1 Ocean General Circulation Model - Reference Manual. *Notes du Pôle de Modélisation - Laboratoire d'Océanographie Dynamic et de Climatologie (LOYDC)*, Note 11:93pp.

Maes, C., G. Madec, and P. Delecluse, 1997. Sensitivity of an Equatorial Pacific OGCM to the Lateral Diffusion. *Monthly Weather Review*, 125:958–971.

Masina, S. and S. G. H. Philander, 1999. An Anlysis of Tropical Instability Waves in a Numerical Model of the Pacific Ocean. 1. Spatial Variability of the Waves. *Journal of Geophysical Research*, 104(C12):29613–29635.

Masina, S., S. G. H. Philander, and A. B. G. Bush, 1999. An Anlysis of Tropical Instability Waves in a Numerical Model of the Pacific Ocean. 2. Generation and Energetics of the Waves. *Journal of Geophysical Research*, 104(C12):29637–29661.

McPhaden, M. J., 1985. Fine-structure variability observed in CTD measurements from the central equatorial Pacific. *Journal of Geophysical Research*, 90:11726–11740.

McPhaden, M. J., A. J. Busalachi, R. Cheney, J. R. Donguy, K. S. Gage, D. Halpern, M. Ji, P. Julian, G. Meyers, G. T. Mitchum, P. P. Niiler, J. Picaut, R. W. Reynolds, N. Smith, and K. Takeuchi, 1998. The Tropical Ocean-Global Atmosphere observing system: A decade of progress. *Journal of Geophysical Research*, 103(C7):14169–14240.

Megann, A. and A. New, 2001. The Effects of Resolution and Viscosity in an Isopycnic-Coordinate Model of the Equatorial Pacific. *Journal of Physical Oceanography*, 31:1993–2018.

Menkes, C., J.-P. Boulanger, A. J. Busalacchi, J. Vialard, P. Delecluse, M. J. M. McPhaden, E. Hackert, and N. Grima, 1998. Impact of TAO vs ERS wind stress onto simulations of the tropical Pacific ocean during 1993-1998 period by the OPA OGCM. *Euroclivar Workshop Rep.*, pages 46–48.

Menkes, E. C., S. C. Kennan, P. Flament, Y. Dandonneau, S. Masson, B. Biessy, E. Marchal, G. Eldin, J. Grelet, Y. Montel, A. Morliere, A. Lebourgues-Dhaussy, C. Moulin, G. Champalbert, and A. Herbland, 2002. A whirling ecosysytem in the equatorial Atlantic. *Geophysical Research Letters*, 29(11):14169–14240.

Mesinger, F. and A. Arakawa, 1976. Numerical methods used in atmospheric models. *GARP publication, WMO, Geneva*.

Mitchell, T. P. and J. M. Wallace, 1992. The annual cycle in equatorial convection and sea surface temperature. *Journal of Climate*, 5:1140–1156.

Moura, A. D. and J. Shukla, 1981. On the Dynamics of Droughts in Northeast of Brazil: Observations, Theory and Numerical experiments with General Circulation Model. *Journal of the Atmospheric Sciences*, 38:2653–2675.

Neelin, J. D., 1992. Tropical air-sea interaction in general circulation models. *Climate Dynamics*, 7:73–104.

Nirala, M. L. and A. P. Cracknell, 2002. Microwave measurement of rain and sea surface temperature by the TRMM Microwave Imager (TMI). *International Journal Remote Sensing*, 23(13):2673–2691.

Nobre, P. and J. Shukla, 1996. Variations of Sea Surface Temperature, Wind Stress and Rainfall over the Tropical Atlantic and South America. *Journal of Climate*, 10(4):2464–2479.

Pezzi, L. P. and I. Cavalcanti, 2001. The Relative importance of ENSO and Tropical Atlantic Sea Surface Temperature Anomalies for Seasonal Precipitation over South America: A Numerical Study. *Climate Dynamics*, 17:205–212.

Pezzi, L. P. and K. J. Richards, 2003. The effects of lateral mixing on the mean state and eddy activity of an equatorial ocean. *To appear in Journal of Geophysical Research.*

Pezzi, L. P., V. Ubarana, and C. A. Repelli, 2001. Forecast and Performance of a Statistical Regional Model for seasonal climate prediction in Southern Brazil. *Brazilian Journal of Geophysics.*

Philander, S. G. H., 1978. Instabilities of zonal equatorial currents, 2. *Journal of Geophysical Reserach*, 83:3679–3682.

Philander, S. G. H., 1990. *El Niño, La Niña, and the Southern Oscillation*, vol. 46 of *GC296.8E4P48*. Academic Press, Inc., 24-28 Oval Road, London, NW17DX.

Philander, S. G. H., 1992. Ocean-Atmosphere Interactions in the Tropics: A Review of Recent Theories and Models. *Journal of Applied Meteorology*, 31:938–945.

Philander, S. G. H., D. Gu, D. Halpern, G. Lambert, N. C. Lau, T. Li, and R. C. Pacanowski, 1996. Why the ITCZ is mostly north of the equator. *Journal of Climate*, 9:2958–2972.

Philander, S. G. H., W. J. Hurlin, and A. D. Seigel, 1987. Simulation of the seasonal cycle of the tropical Pacific ocean. *Journal of Physical Oceanography*, 17:1986–2002.

Polito, P., J. P. Ryan, W. T. Liu, and F. P. Chavez, 2001. Oceanic Atmospheric Anomalies of Tropical Instability Waves. *Geophysical Research Letters*, 28(11):2233–2236.

Polito, P., O. T. Sato, and W. T. Liu, 2000. Characterization and Validation of the Heat Storage Variability from TOPEX/Poseidon at four Oceanographic Sites. *Journal of Geophysical Research*, 105(C7):16911–16921.

Qiao, L. and R. H. Weisberg, 1995. Tropical Instability Wave Kinematics: Observations from the Tropical Instability Wave Experiment. *Journal of Geophysical Research*, 100(C5):8677–8693.

Qiao, L. and R. H. Weisberg, 1998. Tropical Instability Wave Energetics: Observations from the Tropical Instability Wave Experiment. *Journal of Physical Oceanography*, 28:345–360.

Rao, V. B. and K. Hada, 1990. Characteristics of Rainfall over Brazil: Annual Variations and Connections with the Southern Oscilation. *Theoretical and Applied Climatology*, 42:82–91.

Reynolds, R. W. and T. M. Smith, 1994. Improved global sea surface temperature analysis using optimum interpolation. *Journal of Climate*, 7:929–948.

Richards, J., K., 1998. Interleaving at the equator. In *Ocean modelling and parameterization. Series C: Mathematical and Physical Sciences-NATO Science Series*, 516:235–252.

Richards, J., K. and H. Banks, 2002. Characteristics of interleaving in the western equatorial Pacific. *Journal of Geophysical Research*, 107(C12):3231.

Richards, K. J. and N. Edwards, 2003. Lateral Mixing in the Equatorial Pacific: the importance of inertial stability. *Submitted to Geophysical Research Letters*.

Ropelewski, C. F. and M. S. Halpert, 1986. North American Precipitation and Temperature Patterns associated with the El *Niño*/Southern Oscillation. *Monthly Weather Review*, 114:2352–2362.

Ropelewski, C. F. and M. S. Halpert, 1987. Global and Regional Scale Precipitation Patterns associated with the El *Niño*/Southern Oscillation. *Monthly Weather Review*, 115:1606–1626.

Ropelewski, C. F. and M. S. Halpert, 1989. Precipitation Patterns associated with high Index phase of the Southern Oscillation. *Journal of Climate*, 2:260–284.

Seidel, H. F. and B. S. Giese, 1999. Equatorial Currents in the Pacific Ocean 1992-1997. *Journal of Geophysical Research*, 104(C4):7849–7863.

Small, R. J., X.-P. Xie, and Y. Wang, 2003. Numerical simulation of Atmospheric response to Pacific Tropical Instability Waves. *Journal of Climate*, Submitted.

Souza, E., M. T. Kayano, J. Tota, L. Pezzi, G. Fisch, and C. Nobre, 2000. On the Influences of the El Niño, La Niña and Atlantic Dipole Pattern on the Amazonian Rainfall During 1960-1998. *ACTA Amazonica*, 30(2):305–318.

Stern, M. E., 1975. Ocean Circulation Physics. *Academic Press*, page 275pp.

Stockdale, T. D., 1992. *Simulation and prediction of tropical SST with a coupled ocean-atmosphere model.* Ph.D. thesis, Wolfson College, Oxford.

Stockdale, T. D., D. Anderson, M. Davey, P. Delecluse, A. Kattemberg, Y. Kitamura, M. Latif, and T. Yamagata, 1993. Intercomparison of tropical Pacific ocean GCM's. *WMO/TD-545*, WCRP79:43pp.

Strutton, P. G., P. J. Ryan, and F. P. Chavez, 2001. Enhanced Chplorophyl associated with tropical instability waves in the equatorial Pacific. *Geophysical Research Letters*, 28(10):2005–2008.

Swenson, M. S. and D. V. Hansen, 1999. Tropical Pacific Ocean Mixed Layer Heat Budget: The Pacific Cold Tongue. *Journal of Physical Oceanography*, 29:69–81.

Thum, N., S. K. Esbensen, and D. B. Chelton, 2002. Air-Sea heat exchange along the Northern Sea Surface Temperature Front in the eastern tropical Pacific . *Journal of Climate*, 15:3361–3378.

Torrence, C. and G. P. Compo, 1998. A pratical guide to Wavelet analysis. *Bulletin of the American Meteorological Society*, 79(1):61–78.

Vialard, J., C. Menkes, and D. L. T. Anderson, 2003a. Phase Locking of Pacific Ocean Tropical Instability Waves. *Journal of Physical Oceanography*, Submitted.

Vialard, J., C. Menkes, D. L. T. Anderson, and M. A. Balmaseda, 2003b. Sensitivity of Pacific ocean Tropical Instability Waves to Initial Conditions. *Journal of Physical Oceanography*, 33:105–121.

Wallace, J. M., T. P. Mitchell, and C. J. Deser, 1989. The Influence of Sea-Surface Temperature on Surface Wind in the Eastern Equatorial Pacific: Weekly to Monthly Variability. *Journal of Climate*, 2:1492–1499.

Weng, H. and K. M. Lau, 1994. Wavelets, period doubling, and time-frequency localization with application to organization of convection over the tropical western Pacific. *Journal of Atmospheric Science*, 51:2523–2541.

Wentz, J. F., C. Gentemann, D. Smith, and D. Chelton, 2000. Satellite measurements os sea surface temperature through clouds. *Science*, 288:847–850.

Wilson, D. and A. Leetma, 1988. Accoustic Doppler current profiling in the equatorial Pacific. *Journal of Geophysical Research*, 93:13947–13966.

Wunsch, C., 1998. The work done by the wind on the Oceanic General Circulation. *Journal of Physical Oceanography*, 28:2332–2340.

Wyrtki, K. and B. Kilonsky, 1984. Mean water and current structure during the Hawaii-to-Tahiti shuttle experiment. *Journal of Physical Oceanography*, 14:242–254.

Xie, S. P., 1996. Westward Propagation of Latitudinal Asymmetry in a Coupled Ocean-Atmosphere Model. *Journal of the Atmospheric Sciences*, 53(22):3236–3250.

Xie, S. P., M. Ishiwatari, H. Hashizume, and T. K., 1998. Coupled Ocean-Atmosphere Waves on the Equatorial Front. *Geophysical Research Letters*, 25(20):3863–3866.

Yu, Z., J. P. McCreary, and J. A. Prohel, 1995. Meridional Asymmetry and Energetics of Tropical Instability Waves. *Journal of Physical Oceanography*, 25:2997–3007.

Yu, Z. and M. J. McPhaden, 1999. Dynamical analysis of seasonal and interannual variability in the equatorial Pacific. *Journal of Physical Oceanography*, 29:2350–2369.

Zar, J. H., 1996. *Biostatistical analysis*. Upper Saddle River : Prentice Hall, New Jersey, 3rd ed.